Development of Graphene-Based Electrically Conductive Polymer Nano-Composites

by

Yun-Seok Jun

A thesis

presented to the University of Waterloo

in fulfillment of the

thesis requirement for the degree of

Doctor of Philosophy

in

Chemical Engineering

Waterloo, Ontario, Canada, 2018

EXAMINING COMMITTEE MEMBERSHIP

The following served on the Examining Committee for this thesis. The decision of the Examining Committee is by majority vote.

External Examiner	Dr. Chul B. Park
	Distinguished Professor
Supervisor(s)	Dr. Aiping Yu
	Associate Professor
Internal Member	Dr. Christine Moresoli
	Professor
Internal Member	Dr. Ali Elkamel
	Professor
Internal-external Member	Dr. Xiaosong Wang
	Associate Professor

AUTHOR'S DECLARATION

This thesis consists of material all of which I authored or co-authored: see Statement of Contributions included in the thesis. This is a genuine copy of the thesis.

I understand that my thesis may be made electronically available to the public.

STATEMENT OF CONTRIBUTIONS

This thesis is based on a combination of published work. Various chapters are adapted from the following list of published work, with specific reference to the published work provided within the chapter.

Y.S. Jun, S Sy, W. Ahn, H. Zarrin, L. Rasen, R. Tjandra, B. M. Amoli, B. Zhao, G. Chiu, A. Yu. "Highly conductive interconnected graphene foam based polymer composite", *Carbon*, 2015;95:653–658.

> S. Sy, and W. Ahn, and I syntheiszed the materials. H. Zarrin, D. Rasen, R. Tjandra, and B.M. Amoli helped analyzed the data. B. Zhao, G. Chiu and A. Yu reviewed the manuscript.

Y.S. Jun, J.G. Um, G. Jiang, G. Lui, A. Yu. "Ultra-large sized graphene nano-platelets (GnPs) incorporated polypropylene(PP)/GnPs composites engineered by melt compounding and its thermal, mechanical, and electrical properties", *Composite Part B: Engineering*, 2018;133:218-225.

> I carried out the experiments. J.G. Um and G. Jiang helped analyzed the data. G. Lui amd A. Yu reviewed the manuscript.

ABSTRACT

Since a vast array of devices, instruments, and equipment in modern society is powered by electrical energy, it has been a very important research topic to develop and fabricate a material that effectively conducts electricity. Typically, metals have been widely used in a variety of electric applications due to their excellent electrical conductivity and mechanical strength. Nevertheless, the development of an electrically conductive polymer composite has been highly desirable because of its numerous advantages, including excellent chemical stability and high corrosion resistance, light weight, great processability and low production cost. The conductive polymer composites can be employed in a number of applications, such as electromagnetic interference (EMI) shielding and electrostatic discharge (ESD) for electronic devices, transducers in chemical sensors, electrostatic painting, and electrodes for energy storage and conversion systems.

Since its discovery in 2004, graphene has been extensively utilized to produce polymer nano-composites due to its exceptional thermal, mechanical, and electrical properties. In this thesis, graphene is incorporated into polymer matrices via two distinct fabrication approaches: (I) infiltration of a three-dimensional filler matrix with elastomer mixture and (II) compounding by twin screw extruder, followed by injection moulding. In the first approach, graphene oxide solution is synthesized by applying Hummer's method, and as-prepared graphene oxide solution is directly used to construct a three-dimensional graphene architecture by means of freeze casting. This filler matrix is then subsequently infiltrated with elastomer mixture. This unique approach significantly improves the state of filler dispersion, achieving a high electrical conductivity with low percolation threshold. This study finds that the use of graphene with large diameter

significantly improves electrical conductivity. In a follow-up study, graphene nano-ribbons (GNRs) with a high aspect ratio are used to prepare the filler matrix, and the variation of electrical conductivity under uniaxial elongation is also investigated. It is revealed that the incorporation of high aspect fillers considerably improves the consistency of conductivity under a uniaxial tensile strain.

In the second approach, conductive thermoplastic composites were produced by means of twin screw extrusion followed by injection moulding. The compounding process by twin screw extrusion is still widely used in industry due to its ease of processing, efficiency, and low cost. Having clearly seen from the first part of a study that a large diameter is beneficial for obtaining elevated electrical conductivity with low filler contents, we have used the graphene nano-platelets (GnPs) with largest diameter size available to incorporate into polypropylene (PP). Due to a large diameter of GnPs employed in this study, a high electrical conductivity is realized at a low content of GnPs fillers. Nevertheless, mechanical properties of PP/GnP composites show inferior improvements. This is owing to the compromised filler morphology and the lack of efficient bonding between polymer melt and the GnPs.

In a follow-up study, we have extended the inclusion of GnPs of various grades with different dimensions. The diameter of GnPs included in this study spans from a few microns to hundreds of microns. This follow-up study finds that thermal stability and tensile property are considerably improved with decreasing GnPs' sheet size. This is largely due to the improved dispersion with less agglomeration of fillers with retained morphology that maximized the filler effects. The improved tensile strength with the use of small-sized GnPs can additionally be attributed to the enhanced load transfer between GnPs and PP matrix with greater surface area and prolonged crack propagation length. The incorporation of GnPs shows a minor induction effect for β-

crystals, and this effect is intensified with increasing GnPs' diameter. The degree of crystallinity is not significantly varied by the addition of GnPs, although GnPs raise the crystallization temperature of PP by serving as seeds for heterogeneous nucleation. As expected from previous studies, the lowest percolation threshold is observed when the largest sized GnPs are employed. This study clearly shows that the physical dimensions of GnPs have a significant influence on a range of different properties of final composites, and suggests that the GnPs dimensions should carefully be tailored to meet the particular requirement of final composites for each application.

ACKNOWLEDGEMENTS

DEDICATION

무한한 사랑과 희생으로 헌신해주신 부모님과 장인 장모님, 그리고 그
누구보다 고생하며 내조하여 준 사랑하는 아내에게 이 논문을 바칩니다.

This thesis is dedicated to my parents, Hyung-Geun Jun and Young-Do Kim,

my brother, Min-Seok Jun

my parents-in-law, Heon-Yang Park and Sang-Man Jeong

my wife, Kyung-Hee Park,

and my child, Ian Jun

TABLE OF CONTENTS

LIST OF FIGURES

LIST OF TABLES

LIST OF ABBREVIATIONS

CNTs	Carbon nanotubes
CVD	Chemical vapour deposition
DOE	Department of Energy
DSC	Differential scanning calorimetry
DTG	Differential thermo-gravimetric
DC	Direct voltage
EG	Expanded graphite
EIA	Electronic Industry Association
EMI	Electromagnetic interference
ESD	Electrostatic discharge
FRC	Fiber reinforced composites
GnPs	Graphene nano-platelets
GNRs	Graphene nano-ribbons
GO	Graphene oxide
LFG	Large flake graphite
MWCNT	Multi-walled carbon nanotubes
PDMS	Poly (dimethylsiloxane)
PEMFC	Polymer electrolyte membrane fuel cell
PP	Polypropylene
RGO	Reduced graphene oxide
RFI	Radio frequency interference

SEM	Scanning electron microscope
SFG	Small flake graphite
SiC	Silicon carbide
TEM	Transmission electron microscope
TGA	Thermo-gravimetric analysis
VARTM	Vacuum assisted resin transfer moulding
XRD	X-ray diffraction

LIST OF SYMBOLS

A	Area
Å	Angstrom
β	Full width at half maximum
b	width
°C	Degree Celsius
γ_{pf}	Interfacial tension
γ_p	Surface energy of polymer
γ_f	Surface energy of filler
D	Diameter of the insulating powder polymer
d	Thickness of flexural strength
E_B	Flexural modulus
I	Current
λ	Wavelength
L	Span length
L_a	Inter-defect distance
ΔH_{cry}	Crystallization enthalpy
ΔH_m	Melting enthalpy
ρ	Electrical resistivity
R	Electrical resistance
P	Load at the yield
σ	Electrical conductivity

σ_o	Filler electrical conductivity
σ_I	In-plane electrical conductivity
σ_T	Through-plane electrical conductivity
σ_m	Composite electrical conductivity
σ_c	Electrical conductivity at the percolation threshold
σ_F	Electrical conductivity at the maximum loading fraction
σ_f	Flexural strength
t	Sample thickness
V	Voltage
vt%	Volume fraction
wt%	Weight fraction
Φ	Volume fraction of filler
Φ_c	Percolation volume fraction of filler
X_c	Degree of crystallinity

1. Introduction

1.1   Background

Electricity is one of the most essential components of everyday life in a modern society as it is used to run manufacturing and processing machinery in industry, transportation, communication devices, medical instruments, military equipment, and so on [1]. Therefore, the development of electrically conductive material has become one of the most important focal points of research in material science and engineering. Among many types of materials, polymers have gained a tremendous attention as an essential raw material and building block for electrical applications. Because of their versatility, they can fulfil specific requirements for each usage. For many years, polymers have been considered as insulators of electricity and widely used as insulating materials, for example, as a protective layer of copper wires in household electrical cables. However, polymers have recently gained considerable attention as basic conductive materials. For instance, macromolecules can be converted to electrically conductive polymers by incorporating conductive fillers. Such composites can potentially replace metals or other conventional conductive materials in many applications including electromagnetic interference (EMI) shielding, electrostatic dissipation (ESD), and bipolar plates for polymer electrolyte membrane fuel cells (PEMFC).

There are several advantages of replacement with plastic conductive materials in the aforementioned applications. First, polymers have a great chemical stability and are highly corrosion resistant. This is very beneficial to applications where materials are employed in chemically harsh conditions with high acidity, for instance as in PEMFC. Second, a significant weight reduction can be achieved when metals are substituted by conductive plastics. Materials

1

being lightweight are a crucial issue for personal communication devices and automotive parts for fuel economy. Third, the use of plastics results in considerable improvements in processability. It is not easy to process metals into desired shapes and it is often expensive. When dealing with plastics, one can use the existing processing methods, such as compression or injection moulding, and this leads to the ease of manufacturing materials into many different shapes in a quick cycle. Moreover, the amount of conductive fillers added to the polymer can be readily adjusted to cope with the particular electrical requirement for each application. Therefore, the electrical properties of the composite can be easily controlled, and the conductive polymer composites can be applied to a wide range of areas.

A number of materials have been added to plastics to produce conductive composites. Metal fibres and particles comprised of aluminium, steel, iron, copper, and nickel coated glass fibres have been used [2]. Further, a number of carbonaceous materials including carbon black, carbon fibre, graphite, and carbon nanotubes (CNTs) have been employed to increase the electrical conductivity. Among these carbon materials, however, graphene exhibits the uppermost performance in a range of properties, such as exceptional carrier mobility at room temperature ($\sim$250,000 cm^{2}V^{-1}s^{-1}), mechanical strength (Young's modulus of $\sim$1 TPa), electrical conductivity ($\sim$6000 Scm^{-1}), thermal conductivity ($\sim$5000 Wm^{-1}K^{-1}), and large surface area ($\sim$2600 m^{2}g^{-1}) [3]. These properties are superior to other carbon allotropes, such as graphite, CNTs, fullerenes, and diamond as shown in Table 1.1.

When the concentration of these fillers exceeds a certain level, the filler particles come into contact with one another, forming a continuous path for electrons to travel. This particular concentration is called a percolation threshold [4]. The percolation threshold is greatly influenced by the shape of the conductive filler. For instance, $\sim$10-20 wt% of loading levels are required for

the traditional roughly spherical-shaped fillers to make the composite electrically conductive. Carbon black with a loading of 8-40 wt% is required for composites to be commercially utilized while ~1-20 wt% of filler loading is required for successful exploitation when CNTs are used as conductive fillers [5].

Table 1-1. The properties of graphene and other carbon allotropes [3], [6], [7]

Carbon allotropes	Graphite	Diamond	Fullerene	CNTs	Graphene
Hybridized form	sp^2	sp^3	Mainly sp^2	Mainly sp^2	sp^2
Dimension	Three	Three	Zero	One	Two
Specific Surface area (m^2g^{-1})	10-20	20-160	80-90	~1300	~2600
Hardness	High	Ultrahigh	High	High	Highest
Thermal Conductivity ($Wm^{-1}K^{-1}$)	1500-2000[a] 5-10[b]	900-2320	0.4	3500	~5000
Electronic properties	Conductor	Insulator, semiconductor	Insulator	Metallic and semiconductor	Semimetal, Zero-gap semiconductor
Electrical properties (Scm^{-1})	Anisotropic, 2-3 x 10^{4}[a], 6[b]	-	10^{-10}	Structure-dependent	6000

[a]a-direction, [b]c-direction

As such, the aspect ratio of the materials (length-to-width ratio) has a significant influence on the percolation threshold of the composite. Using fillers having a higher aspect ratio, composites with lower percolation threshold can be obtained; CNTs with a diameter of few nano-meters and a length of micrometres is capable of forming a conductive network at significantly reduced filler

loading as compared to carbon black. Keeping the percolation threshold as low as possible is important because a high loading of fillers can be detrimental to the processability and mechanical properties of the composite. It can also cause significant wear and damage to the processing equipment [8].

Conventionally, thermoplastic polymer composites have been widely fabricated via melt compounding, which consists of melt extrusion followed by injection or compression moulding or other processing techniques depending on the properties and purpose of materials. Compounding is usually considered as a mixing process that adds a variety of additives to engineering plastics to achieve particular goals, such as facilitating the process itself or improving a particular property of composite stemmed from the additives. In this technique, engineering plastics serve as a polymer matrix and additives are embedded and incorporated into the polymer matrix usually by means of twin-screw extrusion. This method is broadly employed in the industry due to process easiness, efficiency, and low cost.

In recent years, three-dimensional graphene foam consisting of graphene sheets or CNTs has been developed [9]. This three-dimensional structure exhibits high surface area, great accessible pore volume, and high conductivity at extremely low density. Due to its numerous advantages, graphene foam has been recognized to have a great potential in a variety of applications, such as energy storage devices, sensors, absorbers, and composite materials. When employed to fabricate a composite, this graphene foam serves as a three-dimensional filler matrix that forms a conductive network, and polymers are incorporated into this conductive architecture. Owing to the inter-connected network of graphene structure within the foam, a significantly improved electrical conductivity has been measured at a very low loading of graphene fillers [10]. Thus, the structural advantage of graphene foam makes a great potential in the fabrication of graphene

foam-based polymer composites. Polymer nano-composites based on graphene foam cannot be fabricated by conventional methods such as extrusion and injection moulding; instead, resins are infiltrated into the graphene foam. In this way, the unique structure of graphene foam is not compromised by the processing, and the excellent properties of graphene can be realized.

To summarize, there are numerous advantages of using conductive polymer nano-composites, and many different kinds of conductive fillers and fabrication methods can be used for production. The selection of conducting fillers and fabrication method is greatly dependent upon the property of interest to be improved and the particular application of the final composite.

1.2   Study objectives and approach

The goal of this study is to develop electrically conductive polymer nano-composites by integrating polymers with a variety of carbonaceous materials via two distinct fabrication techniques: (I) infiltration of a three-dimensional filler matrix with polymer and (II) polymer compounding with graphene-based conductive fillers. In the infiltration based work, the main goal is to construct an advanced interconnected graphene network for infiltration and achieve a high consistency in conductivity under elongation. In the compounding based work, the main objectives are to obtain a lowest percolation threshold possible and improve both electrical and mechanical properties of composites. The targeted electrical conductivity from both works is 1 S/m or higher. The flowchart below describes the breakdown of work stream (Fig. 1-1).

In the process of (I) infiltration of filler matrix, three-dimensional graphene foam is first produced with two different graphite with different flake diameter. Elastomer mixtures are then infiltrated into as-produced three-dimensional filler matrices from each size of graphite. In this thesis, poly(dimethylsiloxane) (PDMS) is used as elastomer matrix. In a follow-up project, high

5

aspect ratio fillers are employed to produce the three-dimensional graphene foam to further enhance the electrical properties of the composite. Since as-fabricated composites exhibit flexibility due to the nature of elastomer matrix, the variation of electrical conductivity as a function of tensile strain is investigated and compared between fillers with different dimensions and morphologies.

In the process of (II) polymer compounding, electrically conductive thermoplastic composites are fabricated by twin screw extrusion followed by an injection moulding. Firstly, graphene nano-platelets (GnPs) with a very large lateral size are incorporated into polypropylene (PP), and the various properties of PP/GnPs composites are explored. To obtain PP composites with both improved electrical and mechanical properties, a series of GnPs with different physical dimensions are incorporated, and their influences on a number of important properties of PP/GnPs composites are explored in a follow-up study.
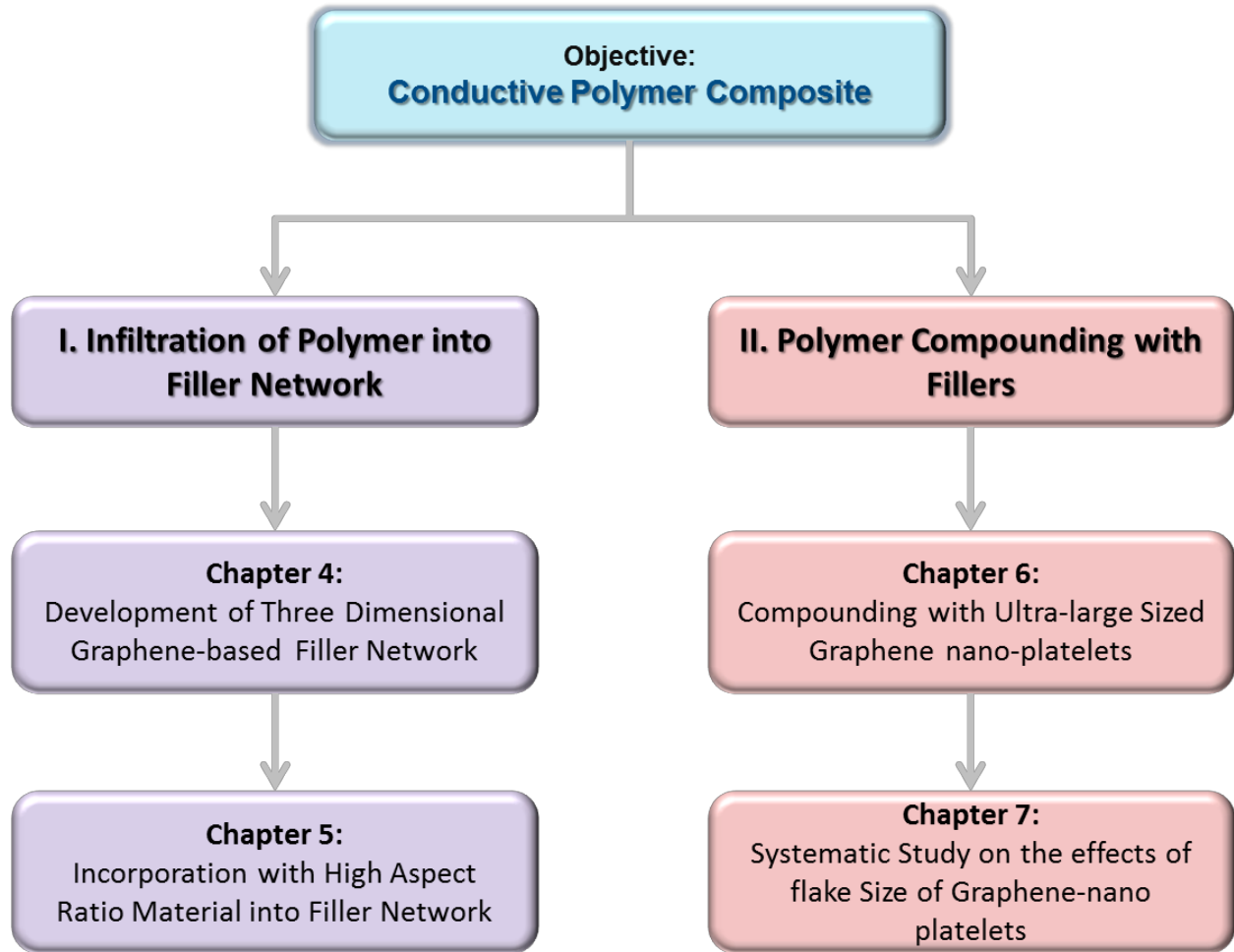
Figure 1-1. The breakdown of work stream

1.3   Thesis outline

This thesis consists of eight chapters organized as follows:

- Chapter 1 provides background information on this research, study objectives, and an outline of the thesis.

- Chapter 2 reviews the characteristics and synthesis methodologies of conductive fillers and the two distinct processing techniques employed in the thesis.

- Chapter 3 describes the materials characterization techniques deployed in this thesis,

including physicochemical characterizations, determination of mechanical properties, and measurement of electrical conductivity.

- Chapter 4 presents the fabrication of polymer composite using the first processing method, which is the infiltration of a three-dimensional filler matrix. The impacts of diameter size of graphene on the electrical conductivity are investigated.

- Chapter 5 discusses the development of a filler matrix using graphene nano-ribbons (GNRs). The variation of electrical conductivity under a uniaxial tensile strain is explored in comparison to the composites prepared from Chapter 4.

- Chapter 6 describes the development of conductive thermoplastic composites processed by means of twin screw extrusion and studies their thermal stability, mechanical, and electrical properties.

- Chapter 7 presents the follow-up study to Chapter 6 extending the inclusion of GnPs of various grades with different dimensions. This chapter provides a comprehensive understanding of influences of GnPs dimensions on the composites' thermal stability, the crystallization of PP, tensile property, and electrical conductivity.

- Chapter 8 summarizes the main results and findings from the thesis and proposes several extended future works to follow this thesis work.

2.   Literature Review

2.1   Composites

According to Fowler and his co-workers, composites are defined as materials that "consist of two or more distinct constituents or *phase*, which when married together result in a material with entirely different properties from those of the individual components"[11]. In general, composites are composed of a reinforcement phase of stiff and strong material dispersed in a continuous matrix phase. Electrically or thermally conductive additives are also incorporated into polymer matrices to impart a specific property of interest that meets the requirement of end-products. The functions of polymer matrices are to transfer externally applied loads to the reinforcement additives and to protect them from environmental and mechanical damage [11]. In this thesis, PP and PDMS were used as main polymer matrices and graphene-based fillers were employed as conducting fillers.

2.1.1   Polymer matrices

2.1.1.1   Polypropylene (PP)

PP is a thermoplastic macromolecule produced by polymerizing propylene monomers into tremendously long polymer chains [12]. PP is categorized into a group of polymers known as polyolefins, which are manufactured in mass production with a great volume of applications. The most common polymerization method for manufacturing PP is the Zieler-Natta system developed in the early 1950s'. PP can have three types of tacticities, which are isotactic, syndiotactic, and atactic. Each tacticity has different molecular configuration, which is determined by the catalyst and the polymerization method used during the production reaction. Depending on their

tacticities, PP can be either a semi-crystalline (isotactic or syndiotactic) or amorphous (atactic) morphology [12].

(a) Polymerization of PP

(b) Isotactic PP

(c) Syndiotactic PP
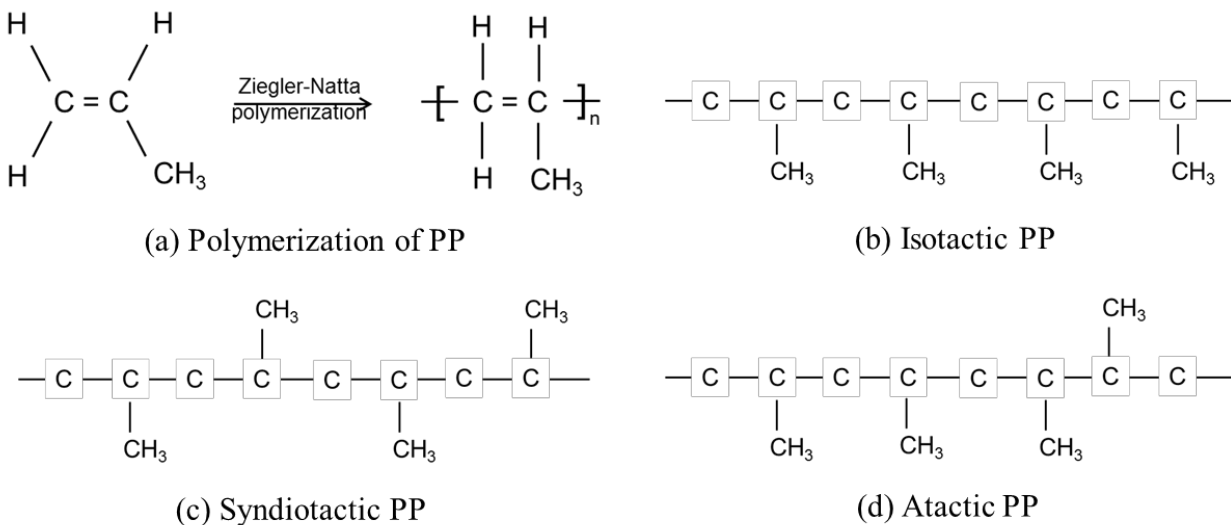
(d) Atactic PP

Figure 2-1. (a) The polymerization of PP, (b) Isotactic PP, (c) Syndiotactic PP, (d) Atactic PP.

The melting temperature of PP is at 176 °C (100% isotactic), and the glass transition temperature is observed at -20 °C, indicating that PP exhibits brittle below -20 °C. The density of semi-crystalline PP falls in a range of 0.9-0.92 g/cm^3 for homopolymer. When used in room temperature, PP provides excellent and desirable physical, mechanical, and thermal properties [12]. PP also has low density and water permeability, and great chemical stability and corrosion resistance. Along with these properties, the low cost and ease of processing of PP allow a vast array of applications including household items, packaging, automotive parts, batteries, bottles and appliances. In particular, great mechanical strength, low gas permeability, and high corrosion resistance make PP suitable for the developments of bipolar plates in PEMFC.

2.1.1.2   Poly (dimethylsiloxane)

Poly (dimethylsiloxane) or PDMS is one of the most widely used commodity polymers

nowadays. PDMS is a silicon-based mineral-organic polymer and often referred to as dimethicone or silicon oil [13]. It consists of repeating unit of dimethylsiloxane, $[(CH_3)_2SiO]_n$ with a molecular weight of 74 g/mol. Since they have low intermolecular forces, PDMS chains exhibit flexibility and solidify at greater molecular weight than other polymers at room temperature [14]. PDMS has been utilized in a variety of applications due to its elastomeric properties, gas permeability, optical transparency, ease of bonding to itself and to glass, ease of moulding, and relatively high chemical resistivity. PDMS is also considered inert, non-toxic and non-flammable. It also can be used for prosthesis and internal body applications since PDMS is biocompatible.

The production of PDMS is based on the E. Rochow's work which presented a method to synthesize dimethyldichlorosilane, $(CH_3)_2SiCl_2$, the initial material for PDMS production [15]. In his experiment, a gaseous mixture of hydrochloric acid (HCl) and methylchloride (CH_3Cl) with a 1:50 ratio was introduced into a heated tube furnace at 370 °C through silicon-copper alloy. The small amount of HCl was first fed in and edged the surface of silicon-copper for increased exposure, and then CH_3Cl was reacted with Si, producing dimethylchlorosilane $(CH_3)_2SiCl_2$ in described in equation 2-1. This dimethylchlorosilane was reacted with nearby water molecules to produce $(CH_3)_2Si(OH)_2$, which then condensated with itself resulting in PDMS as shown in equation 2-2 and 2-3 below [14].

$$Si + 2CH_3Cl \longrightarrow (CH_3)_2SiCl_2 \qquad\qquad (2\text{-}1)$$

$$(CH_3)_2SiCl_2 + 2H_2O \longrightarrow (CH_3)_2Si(OH)_2 + 2HCl \qquad\qquad (2\text{-}2)$$

$$2(CH_3)_2Si(OH)_2 \rightarrow \overset{\displaystyle CH_3 \quad CH_3}{\underset{\displaystyle CH_3 \quad CH_3}{OH-Si-O-Si-OH}} + H_2O \qquad (2\text{-}3)$$
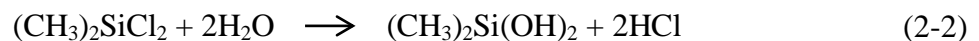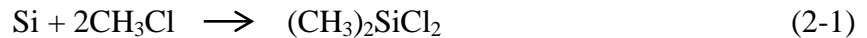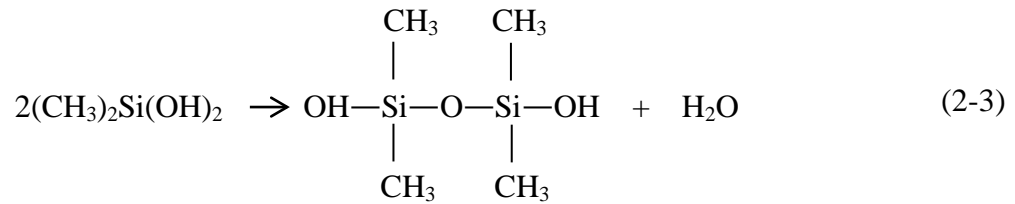
In a market, PDMS comes in a kit consisting of a base (denoted as 1 in Fig. 2-2) and a curing agent (denoted as 2 in Fig. 2-2). Both compounds have siloxane oligomers that contain vinyl groups at the end of chain. The curing agent has cross-linking siloxane oliogomers, which comprise a minimum of three silicon-hydride bonds. A platinum-based catalyst is included in the base, which helps cure the elastomer by an organometallic cross-linking reaction. When the base, the curing agent, and the catalyst are mixed together, the catalyst helps the process called hydrosilation of the double bonds where the Si-H bonds from the curing agent is added to the double bonds of the base, forming Si-CH$_2$-CH$_2$-Si chain. It should be noted that no wastes are produced from this reaction. Three-dimensional networking takes place due to the several reaction sites on the curing agent. The rigidity of the resulting cured elastomer is dependent upon the curing agent-to-base ratio. A more rigid elastomers will be produced when the ratio of curing agent-to-base increases [16].
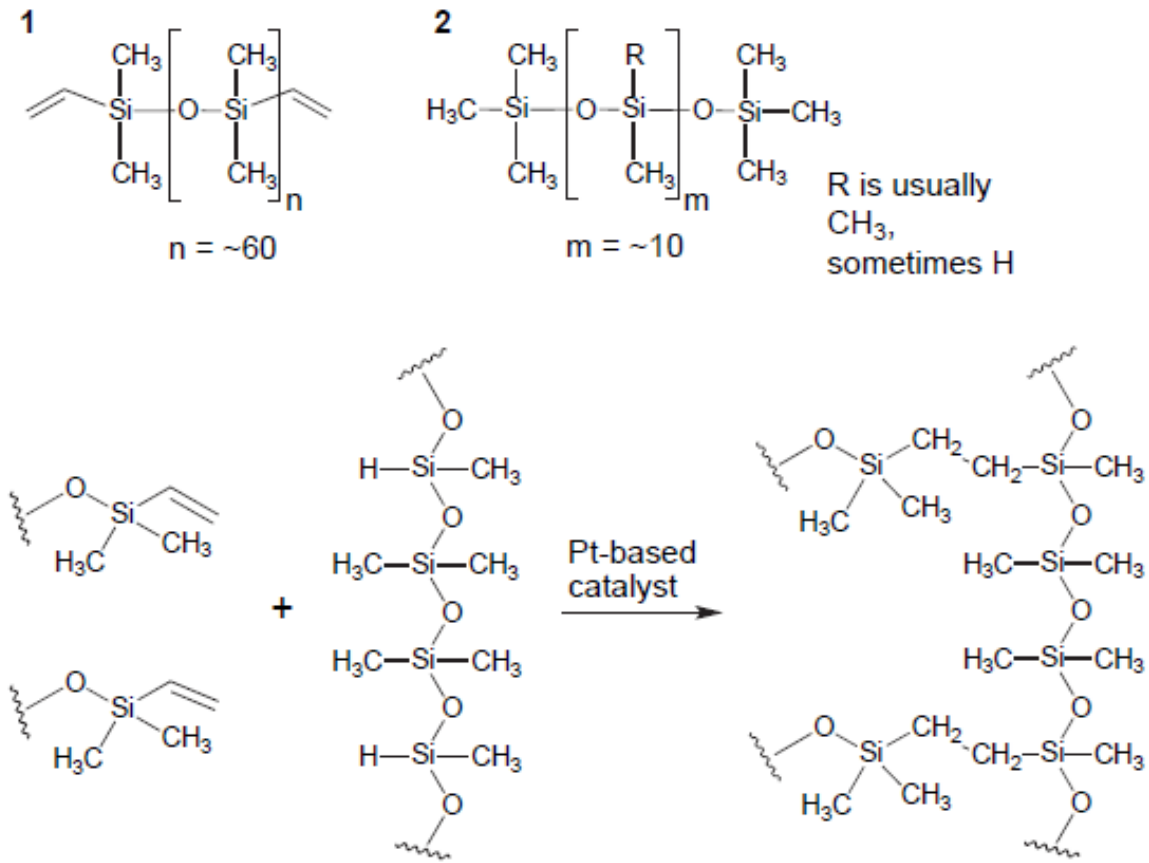
Figure 2-2. The cross-linking polymerization of PDMS [16]. **(copyright @ American Chemical Society)**

2.1.2 Conductive fillers

2.1.2.1 Graphene and graphene oxide (GO)

Graphene is a single layer of sp^2 carbon atoms arranged in a honeycomb structure. A number of graphitic carbon allotropes can be derived from graphene as illustrated in Fig. 2-3. The zero-dimensional fullerenes, one-dimensional CNTs, and three-dimensional graphite are all stemmed from graphene. Recently, graphene has attracted considerable attention due to its extraordinary properties, such as a thermal conductivity of 5000 W/(m•K), an electrical conductivity up to

~6000 S/cm, and Young's modulus of 1 TPa. In addition, graphene exhibit an extremely high surface area up to ~2630 m^2/g and gas impermeability [7]. With its exceptional properties and possibility to be dispersed in various polymer matrices, the advent of graphene has created a new class of polymer nano-composites.

Graphene can be produced by a variety of methods, and the synthesis methods can be generally classified into two large categories: bottom-up and top-down processes. The bottom-up processes include chemical vapour deposition (CVD), arc discharge, and epitaxial growth on SiC [17]. Graphene produced by CVD or epitaxial growth often exhibit a high quality without defects. However, very tiny amount of graphene is produced per process. Therefore, these methods are not appropriate for polymer nano-composite research where a mass production of graphene is desired, but they are more suitable for fundamental graphene research or electronic applications. In the top-down process, a few layered graphene sheets are directly separated or exfoliated from graphite or graphite derivatives such as graphite oxide. The top-down processes include a solution-based oxidation of graphite followed by exfoliation and reduction of graphite oxide, direct exfoliation of graphite such as mechanical cleavage or liquid phase exfoliation of graphite. Among these top-down approaches, the solution-based oxidation and subsequent reduction of graphite oxide are extensively employed for polymer nano-composite application because this method has a significant potential for scale-up production of graphene with low cost [7].
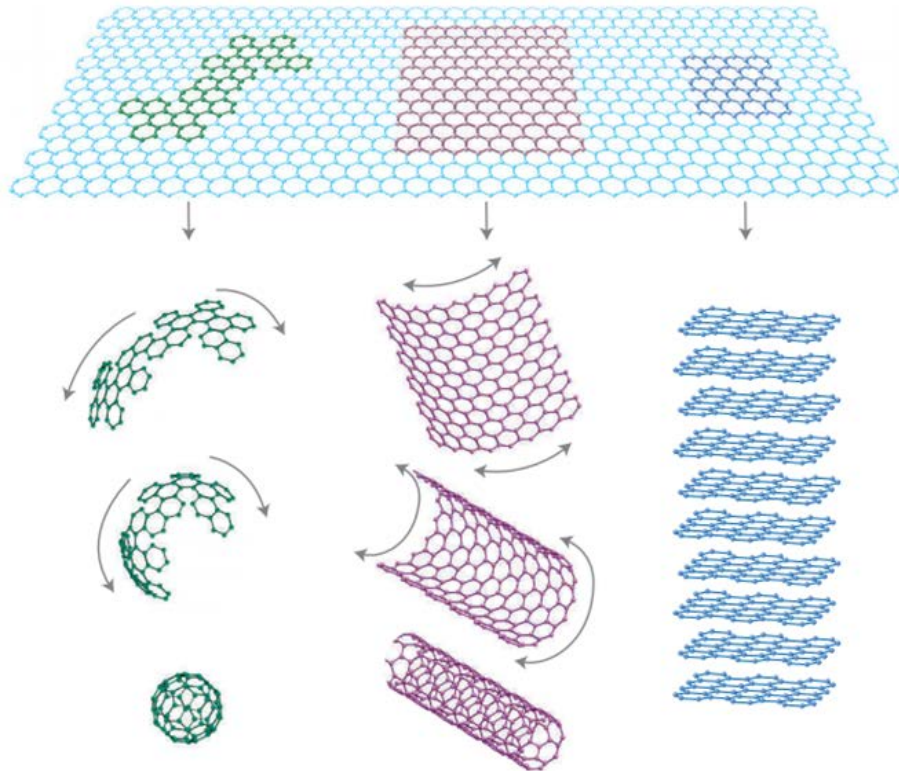
Figure 2-3. A number of graphitic carbon allotropes can be derived from graphene. The zero-dimensional fullerenes, one-dimensional CNTs, and three-dimensional graphite are all stemmed from graphene [18] **(copyright @ 2007 nature publishing group).**

Graphite oxide is prepared by the intercalation and oxidation of graphite powder, usually by Hummer's method [19]. In Hummer's method, graphite powder is heavily oxidized by $KMnO_4$ and $NaNO_3$ in concentrated H_2SO_4 to form graphite oxide. The reaction creates a strong oxidizing species, dimanganese-heptoxide (Mn_2O_7). When graphite is soaked with these oxidizing agents at around 55 °C, a series of micro detonations occur and this functionalizes the graphite surface [20]. The functionalities primarily consist of epoxide and hydroxyl groups, which are highly hydrophilic producing strong hydrogen bonds with water. With strong oxidizing agents with various functionalities formed between layers, the intercalation step expands the distance between the graphite planes from 0.335 nm to 0.6~1.2 nm. Finally, upon introducing these compounds into water, graphite oxide can be easily exfoliated into a few layer of graphene

oxide (GO) by strong mixing or weak sonication. Due to the high solubility and hydrophilic edges of the functionalities formed on the basal plane, GO is easily dispersed in water. GO can be further reduced to remove the functionalities to restore the electrical property. The reduction can be achieved by exposing GO to reducing agents such as hydrazine and $NaBH_4$. The GO reduction also can be achieved by heat treatment, which is named thermal annealing reduction. Upon exposing GO to rapid heating, reduced GO (RGO) is produced and a further exfoliation is obtained along with reduction [21].

Oxidation
Hummer's method

Reduction

Graphite

Graphite Oxide

Reduced Graphene Oxide
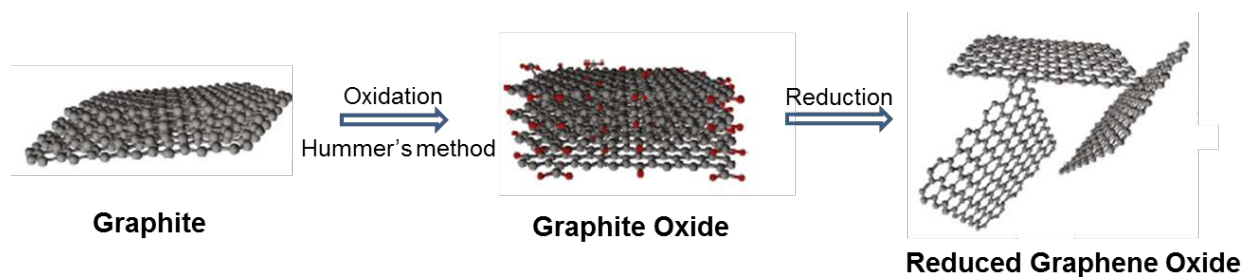
Figure 2-4. The production of graphene via oxidation and reduction of graphite [22]**. (copyright @ 2016 Elsevier)**

2.1.2.2 Graphene nano-platelets (GnPs)

GnPs are layered graphene nano-crystals in the structure of platelets stacked by van der Waal's forces [23]. The GnPs synthesis begins with intercalating graphite with alkali metals or acids, and these intercalated graphite compounds are thermally treated to expand their layered structures [24]. These expanded compounds, called expanded graphite (EG), appear worm-like accordions as described in Fig. 2-5. Upon pulverization using ultrasonication or ball milling, a thinner form of GnPs are obtained (Fig. 2-5b). Since the large diameter and stiffness of graphite is retained during the production process, GnPs can enhance electrical and mechanical properties of polymers at considerably lower loadings in comparison to graphite or EG. Recently, GnPs

16

have been recognized as an inexpensive alternative to graphene due to its possibility of mass production with low cost [25], [26]. The incorporation of GnPs into conventional polyolefins has promising potential in a vast array of applications due to its excellent thermal, mechanical, and electrical properties. Such composites can be employed in the fields of electronics, automobile, aerospace, sensors, and etc [27]–[29].
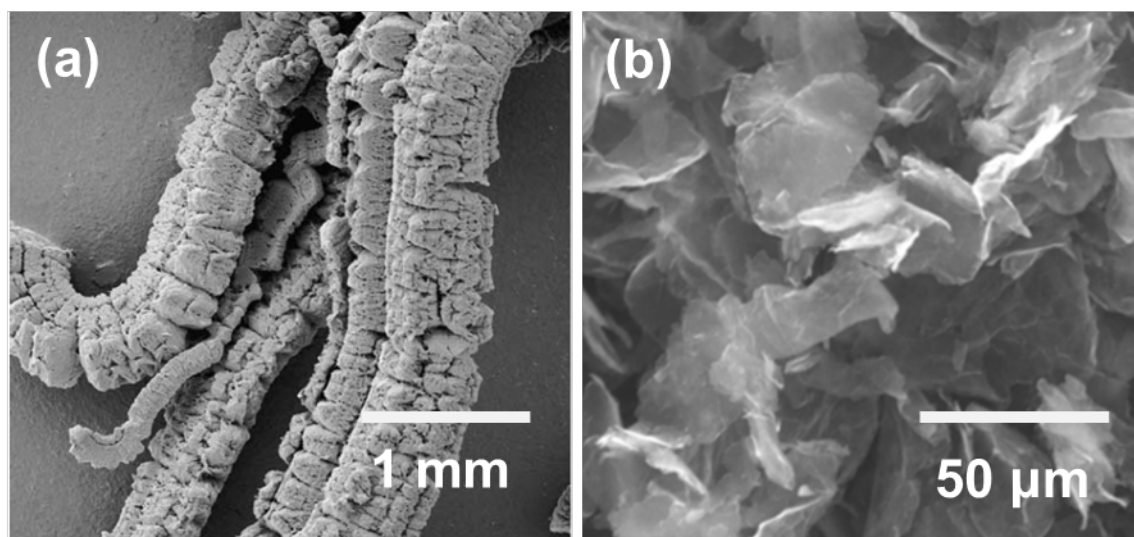
Figure 2-5. SEM images of (a) EG[30] **(copyright @ 2005 Elsevier) and (b) GnPs** [31]**. (copyright @ 2012 IOP Publishing)**

2.1.2.3   Graphene nano-ribbons (GNRs)

GNRs are laterally confined, thin and long strips of graphene sheets with a high length-to-width ratio. GNRs can be produced using a number of different techniques, and most of the techniques use graphene or CNTs as a starting material. Graphene and CNTs are scissored or unzipped by applying various cutting mechanisms. With graphene as a starting material, various techniques such as lithographic patterning followed by plasma etching [32], sonochemical breaking of chemically derived graphene [33], and metal nano-particle catalyzed cutting of graphene sheets [34] have been reported. On the other hand, the techniques employing CNTs as a starting

17

material include Ar plasma etching [35], chemical attack by strong oxidizing agents [36], intercalation and exfoliation by lithium and ammonia [37], and metal-catalyzed cutting [38]. In addition, a few bottom-up techniques have also been suggested. These approaches include chemical vapour deposition [39] and chemical synthesis [40]. Among these techniques, the longitudinal unzipping of CNTs is considered most promising due to its potential for mass production. Specifically, the method of unzipping of CNTs by strong oxidizing agents is a simple, efficient, and scalable technique. Since this technique was employed to produce GNRs used in this study, this method is illustrated in Fig. 2-6b and briefly reviewed as follows.

First presented by James Tour and co-workers [36], this method is based on the previous work of oxidizing alkenes by permanganate in acid [41]. By placing CNTs in contact with $KMnO_4$ in highly acidic environments, manganite ester is formed and converted to dione upon further oxidation. The structural distortion induced by these ketones make the neighbouring β,γ-alkenes (red in Fig. 2-6b) prone to next attack by permanganate. Hence, once the opening is initiated, its further opening is prompted at the neighbouring site rather than unopened or uninitiated sites on the same tube. This cutting process propagates until the tube is entirely unzipped, and the ketones can be transformed to carboxylic acids at the edges of nano-ribbons.

These lengthwise unzipping of CNTs by strong oxidizing reactants can produce long and uniform GNRs in a relatively large amount. Due to their possibility for large-scale production with a high yield (~100%), this method is appropriate for polymer nano-composite research.

18
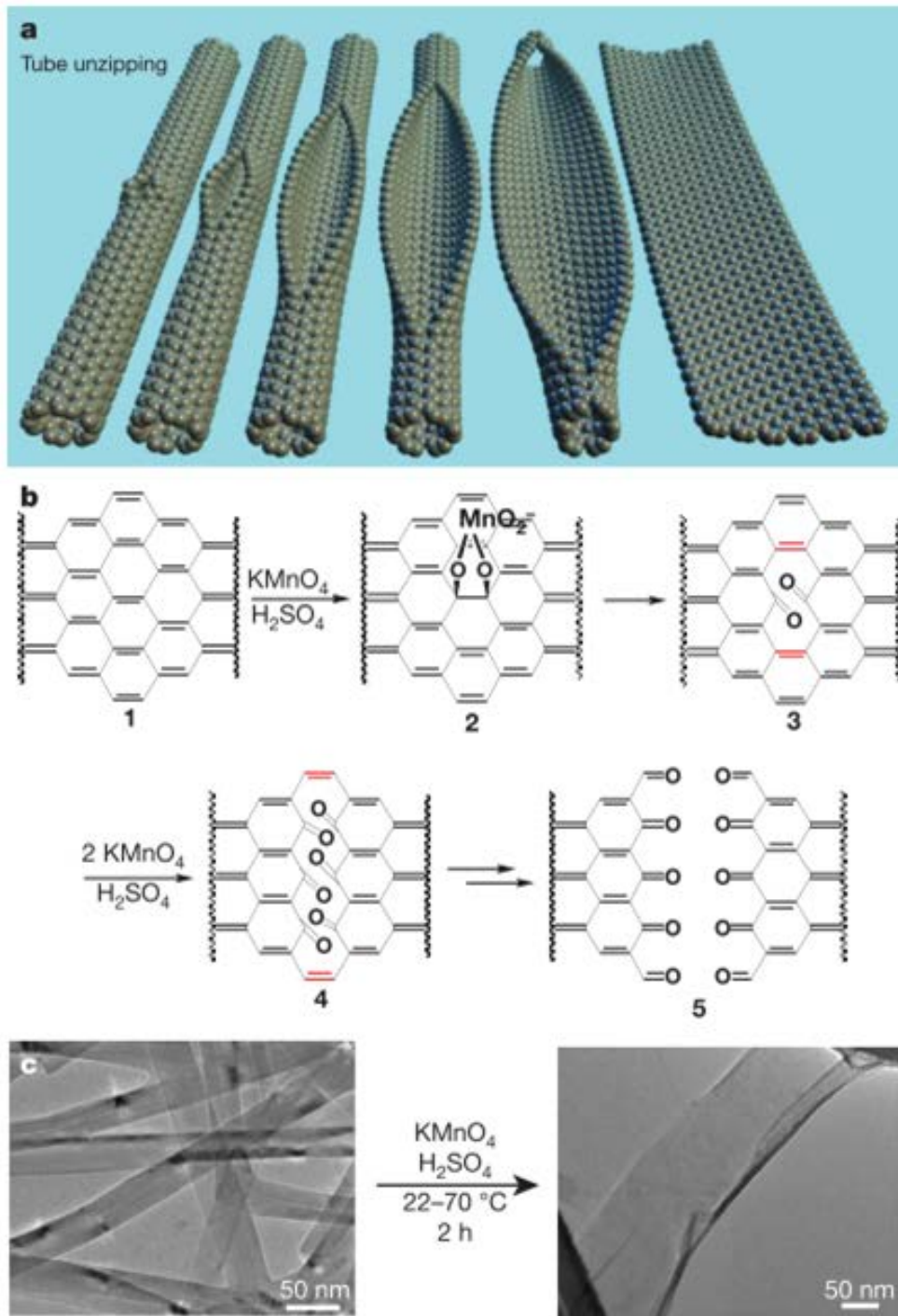
Figure 2-6. (a) Representation of the lengthwise unzipping of the CNTs. (b) The proposed chemical mechanism of CNTs unzipping. (c) TEM images illustrating conversion of nanotubes to nanoribbons [36]. (copyright @ 2009 Nature Publishing Group)

In this thesis, to fabricate the polymer composites via the infiltration method, GO is employed as central fillers. This is because the functional groups formed during the oxidation are desirable to disperse the fillers in water and produce free standing foam. This chemically created GO is thermally reduced to remove the functional groups and restore the electrical conductivity. However, there still exist residual oxygen-containing functionalities on the RGO sheet, and their electrical conductivity is low as compared to pristine graphene. RGO also have less number of layers and great surface area, the viscosity of polymer melt dramatically increases when RGO is added via shear mixing, which makes it inappropriate for use in compounding method. On the other hand, the production of GnPs does not involve a significant oxidation, and hence their content of oxygen is considerably lower than RGO. Since the GnPs have more number of layers and lower surface area, these are preferably utilized when polymer composites are produced by compounding technique. The characteristics of RGO and GnPs are described in Table 2-1.

Table 2-1. The comparison of characteristics of RGO and GnPs used in this study [21], [42]**.**

	Production route	**Oxygen contents (%)**	**Surface area (m^2/g)**	**Thickness (nm)**	**Number of layers**
RGO	Chemical oxidation followed by reduction	< 5	> 300	~2-3	~5-8
GnPs	Thermal expansion followed by ultrasonication (or ball-milling)	< 1	~50-150	~6-15	~20-30

2.2 The incorporation of polymer into filler matrix by infiltration

2.2.1 Direct drying techniques

Direct drying of hydrogels can provide an efficient and facile way to prepare three-dimensional

foam. When drying hydrogels, they are to be dried in a way that does not compromise the original structure. When they are dried from a liquid state, the capillary action and surface tension of water collapse the pore structures. To prevent this, freeze drying is often employed to minimize the stress exerted on the porous structures. Freeze drying, also known as lyophilization, is a process of removing water by sublimation and desorption under vacuum [43]. The capillary stress is reduced by going around the water's triple point boundary. Water is first frozen by lowering temperature, and it is directly gasified from solid by crossing the solid-gas boundary via low pressure. By applying this method, hydrogels composed of two dimensional sheets in frozen solution can preserve their internal network, and macro-scale foam with high surface area can be obtained. The drying process is an essential step in producing porous and three-dimensional architecture from hydrogels [9].

2.2.2 The fabrication of three-dimensional graphene foam

The utilization of a three-dimensional assembly of graphene is a very effective way of improving graphene application because it exhibits high surface area and prevents agglomeration and restacking of the graphene sheets. The three-dimensional network of graphene foams, which is also referred to as hierarchal three-dimension structures, sponges, templates, and aerogels, are mainly synthesized by two methods [9]: I) direct drying of graphene oxide (GO) hydrogels or II) template guided growth of graphene by chemical vapour deposition (CVD). On one hand, the direct drying method includes direct drying from GO precursors, self-assembly by hydrothermal reduction, and cross-linking enhanced self-assembly. In each method, different reducing agents, temperatures, and additives are used according to the targeted products, but these techniques share a common drying process for the formation of the foam structure. On the other hand, bottom-up growth of graphene on metal catalyst template via CVD could provide a

fundamentally different procedure for achieving a high quality and strictly defined porous foam structures at the macro scale.

GO hydrogel is currently the most common predecessor for the production of free-standing graphene foams. Since GO is readily dispersed in water, the GO solution can be directly freeze-dried to form GO foams. Also, graphene foam can be obtained by employing hydrothermal reduction. During the initial stages of low-temperature hydrothermal reduction, the basal plane of GO shifts from a hydrophilic state to more hydrophobic regime. Hydrogen bonding with water gets weakened and the van der Waal attraction between the planes increase, creating sticky graphene sheets and leading to self-assemble [44]–[47]. The self-assembly can be enhanced by the addition of cross-linking agents. The addition of crosslinking agents helps increase the strength and elasticity of GO foams. For example, Ye et al. utilized epoxy monomers to combine with GO solutions [48]. They introduced epoxy monomers into a GO suspension and underwent freeze drying and curing. The final composite exhibited improved elasticity and mechanical strength. Zhao et al. added pyrrole (Py) into GO aqueous suspension and form a homogeneous solution before the hydrothermal reduction [49]. The nitrogen-rich monomer was capable of interacting with the GO sheets through hydrogen and pi-pi bonding to minimize self-stacking of GO during reduction while still stimulating binding between rGO. After reduction, the monomer dispersed hydrogel was polymerized to improve the strength. The final foam showed an excellent electrical conductivity and reversible compression.

2.2.3   Infiltration of polymer into graphene foam

In order to fabricate a polymer nano-composite based on graphene foam, macromolecules should be absorbed and infused into the three-dimensional network of graphene. To fully recognize the

advantages of the graphene foam, there should not be any compromising to the structure of the foam when polymers are integrated into a filler matrix. To this end, polymers in the liquid state are used to be infiltrated into the graphene foam, and this infiltration is a well-known method for fabrication of polymer nano-composite that does not break the original structure and network of graphene foam. The infiltration method can be applied to types of polymers that can exist in a liquid state including thermoplastic and thermoset polymers. When thermoplastics are dissolved in a solvent, it can be infiltrated into graphene foam, but the post-removal of solvent is necessary. The thermoset polymers are preferred because a solvent is not involved in the process and they can be readily backfilled into graphene foam if their wetting on graphene sheets is favoured. Infiltration of polymers is mainly driven by the capillary action and gravity while the capillary action plays a greater role for nano-scale composite. There are several factors that determine the effectiveness of capillary infiltration, such as surface interaction, temperature, and geometry of nano-pores.

The surface properties of the fluid and medium play a central role in capillary infiltration because the molecular level interaction determines the surface wetting capability. For example, at the liquid-solid surface interface, if the molecules of a liquid have a stronger attraction to that of the solid surface than to each other, wetting of the solid surface takes place. In other words, the adhesive forces should be stronger than cohesive forces. However, if the cohesive forces are greater than the adhesive forces, the liquid forms beads and does not wet the solid surface.

One way to investigate a fluid's wetting capability is to measure the contact angle of a drop of liquid placed on the surface of the object. The contact angle is the angle formed by solid-liquid interface and liquid-vapour interface and measured from the side of the liquid (Fig. 2-7). The contact angle is clearly indicative of wetting capability. The higher tendency of a drop to spread

over a flat solid surface, the lower the contact angle. Therefore, the contact angle is an inverse measure of wettability. Usually, the contact angle greater than 90° indicates that the wetting is not favourable whereas the contact angle less than 90° means that the wetting occurs.
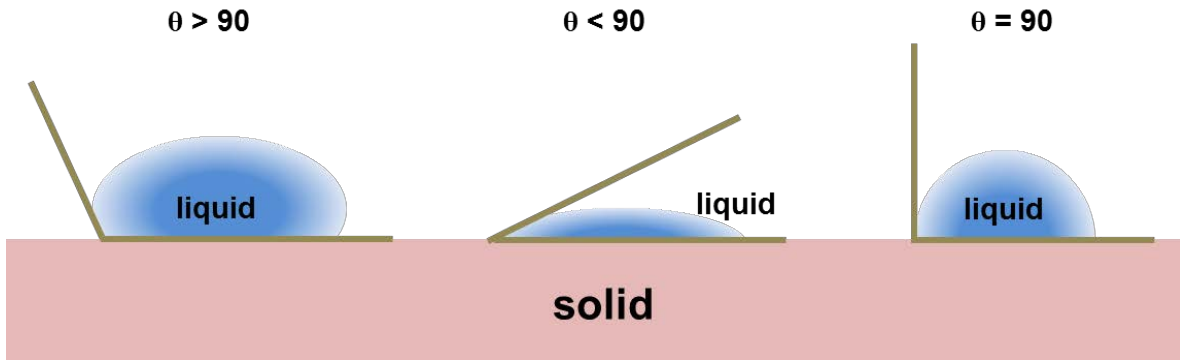
Figure 2-7. Contact angle measurements.

The effect of temperature on the wettability has been investigated. It has been shown that the infiltration is enhanced with increasing temperature [50]–[53]. This thermal effect has been particularly studied in the case of infiltration of water into hydrophobic nano-pores for various nano-fluidic applications including molecular sensors, nano-pipettes, hydrogen storage, and fluid filtration devices. Xu et al. attributed the thermal effect to its relation with the surface tension and the contact angle of water molecules [50]. They reported that the decrease in surface tension and contact angle led to the improved infiltration and found that surface tension and contact angle were closely correlated with variation of temperature. According to them, the contact angle was considerably reduced with increasing temperature, and it was further decreased with a smaller pore size of carbon materials. Furthermore, the surface tension of water also decreased as the temperature or the size of pore increases. Therefore, the thermal dependence of surface tension and contact angle account for the wetting transition of the nano-channels with temperature change.

The effects of pore characteristics on the capillary action also have been studied. Ceratti et al. reported that the capillary filling speed is improved with increasing pore size [54]. In the presence of constrictions such as bottlenecks, the filling rate is diminished as compared to the conditions without constrictions. However, when the constrictions of similar shapes are present with a different size, the capillary action is enhanced with smaller pores than with larger pores (Fig. 2-8). This is due to the easiness for the vapour phase to capillary condense in smaller pores.
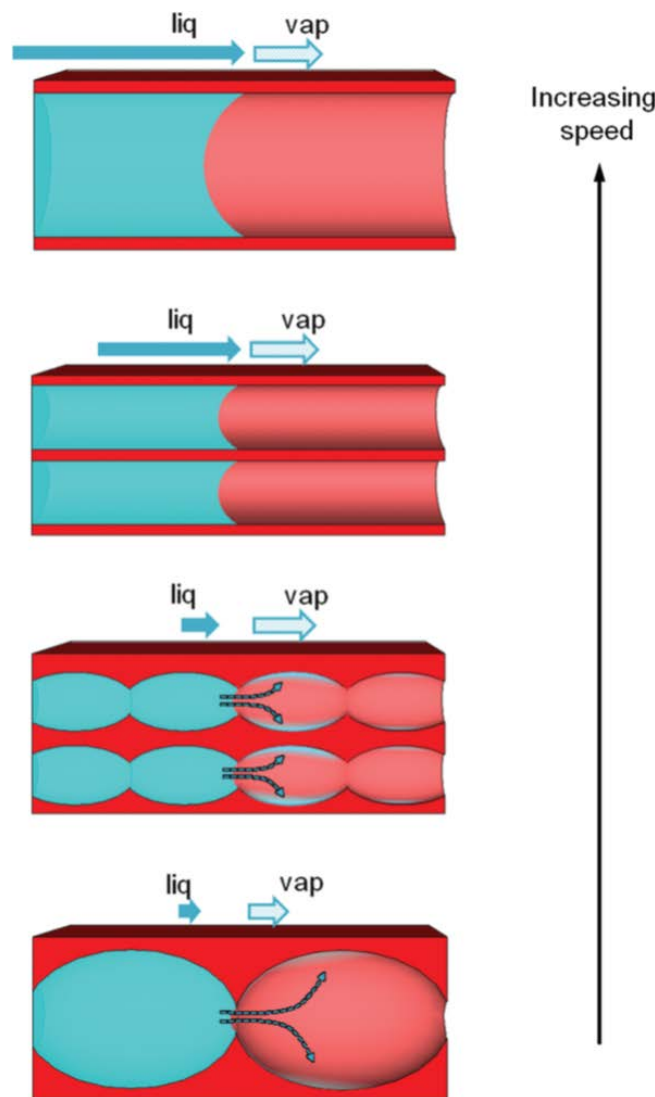
Figure 2-8. The illustration of the capillary infiltration in the various porosities [54]**. (reproduced with permission from the Royal Society of Chemistry)**

2.2.4　Application areas

The infiltration of the polymer into reinforcement filler has been used in industry for a variety of applications. A process called vacuum assisted resin transfer moulding (VARTM) has been developed and employed to fabricate polymer composites, primarily fibre reinforced polymer composites. Within the VARTM process, a reinforcing fabric is placed on a rigid mould that has the shape of the desired composite part. The mould is sealed and vacuum is applied to ensure a complete infiltration with resin. In the final stage of the process, the mould is heated to cure the composite. A schematic diagram of VARTM is illustrated in Fig. 2-9.
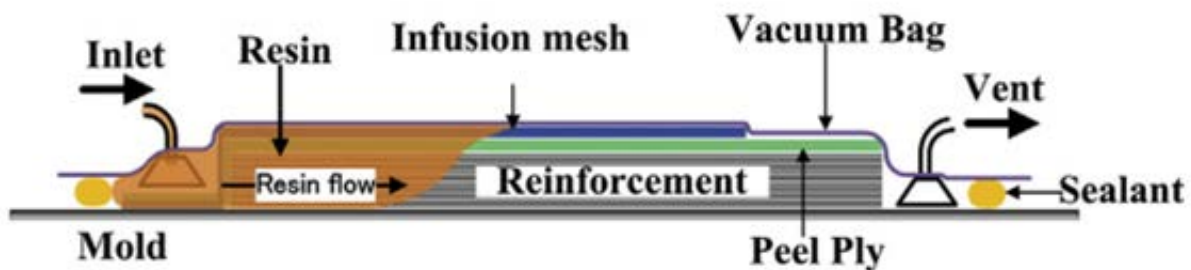
Figure 2-9. A schematic diagram of VARTM [55]**. (copyright @ 2016 Elsevier)**

Fiber reinforced composites (FRC) fabricated by VARTM has been used in many applications [56]. The reinforcing fibre can be glass, carbon materials, boron, or aramid materials. These FRC materials exhibit a high strength-to-weight ratio when compared to conventional metals such as aluminium or steel and have improved chemical stability and advanced design capability. The lightweight and stiff characteristics of these composites have great potential in the manufacture of aerospace vehicles [57]. For example, Boeing Aerospace and Airbus Aerospace have integrated structural composites into the airframe of two commercial jetliners. The carbon fibre reinforced polymer composites have been used in the vertical and horizontal tail sections for the

Boeing 777. The carbon fibre reinforced polymer composites also have been employed in the primary structure of airplane's vertical tail section for Airbus A300-310.

Furthermore, such composites have been incorporated in the fabrication of automotive parts including interior frames, exterior panels, and towing packages, due to the high demand for more fuel-efficient vehicles. For example, new Toyota and Honda truck beds are made of carbon fibre reinforced polymer composites. The US army also has used polymer composites reinforced with carbon, boron, and aramid fibres in many of its ground assault and transport vehicles [57].

The hulls and decks of recreational boats and yachts have been produced using glass fibre reinforced polymer composites. When conventional materials such as wood or steel are replaced with such composites, tremendous cost savings in production labour can be achieved. Further, the final products have much-improved durability under the working environments where they are exposed to salt water for a long term. In addition, a number of recreational products including skis, snowboard, and bicycles are fabricated by incorporating FRP composites. Further, almost all tennis rackets and many golf club shafts are produced with high-performance carbon fibre composites [57].

2.3   The incorporation of filler into polymer matrix by compounding

2.3.1   Polymer processing and compounding

In general, polymer processing plays an essential role in determining the properties of polymer products. By varying processing conditions, one can obtain polymers with very different thermal history, mechanical stress/strain history, and chemical modifications. These will greatly impact the structure of polymers in terms of orientation, crystallinity, crystal size and structure, and so

27

on. Such variations in structure again significantly influence mechanical, optical, and chemical properties of polymers, which are to be controlled and optimized for a variety of fields of applications [58]. Therefore, processing, structure, and properties of polymer products are strongly connected to one another, and processing conditions should be carefully considered to meet the requirement of the final application. There are many different types of polymer processing techniques, such as thermoforming, extrusion, injection moulding, compression and transfer moulding, blow moulding, plastic foam moulding, and etc. By applying a novel processing technique that employs the unique characteristics of polymers, one can significantly improve the particular property of polymer with great productivity and low cost, which can lead to enormous success in the marketplace.

Compounding is one of the most important processing practices in polymer industry that incorporate additives, fillers, or reinforcing agents to facilitate processing or develop innovative polymer materials with particularly improved properties applicable to their proposed use. By compounding with additives such as stabilizers, lubricants, colourants, and etc, one can enhance polymer characteristics and applicability without compromising its mechanical properties and processing easiness. Moreover, a number of desired properties, such as electrical and thermal conductivity, enhanced mechanical property, flame retardancy, ultraviolet stability, weathering and barrier properties can be obtained by incorporating with appropriate fillers [59].

In addition, polymer compounding exhibits several advantages such as simplicity and comprehensiveness. Compounding accommodates the combined polymer and other ingredients with current industrial machinery, which also provides a great compatibility. Also since the processing can be continuous and is not very time-consuming, a number of composites can be prepared in a short period of time, achieving a high production rate with low cost. Furthermore,

28

formulation of polymer matrix and additives can be readily tailored to meet the processing condition and the required properties for the intended subsequent use. Compounding can be carried out by either a batch system (e.g. internal high-speed mixer) or continuous system (e.g. single screw or twin screw extruders), but a co-rotating twin screw extruder is most extensively used [60]. Due to their versatility and extensive use in diverse fields of industry, single screw and twin screw extruders will be briefly reviewed in the following sections.

2.3.1.1 Single screw extruder

Screw extrusion is a unit operation of the greatest significance in the field of plastic processing due to its extensive use and its direct relation to productivity and product quality. Single screw extruders are largely employed to melt solid polymers and deliver the molten polymers for shaping and forming in many major polymer manufacturing processes including continuous extrusion, injection moulding, blow moulding, and thermoforming [58]. In addition to melting, screw extrusion also performs other tasks, such as mixing, devolatilization, and chemical reaction.

A schematic image of a single screw extruder is described in Fig. 2-10. In a single screw extruder, a screw is housed in a heated barrel. A feed section is located at the beginning of the extruder and the hopper is placed on the top of the feed section. A feed polymer is supplied into the screw through the hopper, and the feed section is kept cool by circulating water to prevent the feed polymer from sticking onto the wall. A motor rotates the screw, and the high speed of the initial motor is decreased by a reducer and a transmission connecting the motor and screw. The feed polymer in the hopper falls into the rotating screw through feed throat and melts inside the extruder. At the end of the barrel, a screen pack filters the molten polymer and the filtered

polymer streams out of the extruder through an adaptor and a die [61].
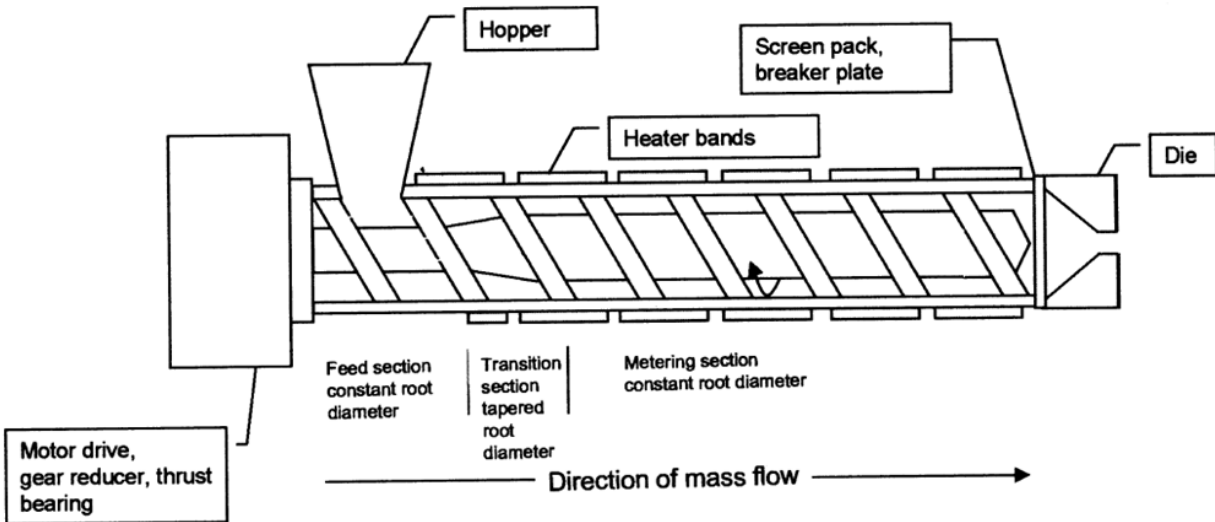
Figure 2-10. A schematic presentation of single screw extruder [61]**. (copyright @ 2002 Elsevier)**

The most critical component of an extruder is the screw since the performance of the extruder is significantly dependent upon the screw design. The production rate and product quality can be considerably enhanced by optimizing the screw design. A conventional screw has three distinct sections as shown in Fig. 2-10, which are a feed section, a compression or transition section, and a metering section. In the feed zone, the feed polymer is readily conveyed into the compression zone due to greater pitch or high flight depth. The pressure in this zone is also low to enable consistent feeding from the hopper. The pressure in the extruder gradually increases from the compression zone as the pitch or flight depth decreases. In the compression zone, the feed polymer is melted, mixed, compressed, and plasticized [61]. The material enters the metering section in the form of a homogeneous melt. The role of the metering zone is to stabilize pulsating and effervescent flow and ensure consistent thickness, shape, and size of extrudates. An even flight depth and pitch will help maintain high pressure in the metering zone, resulting in a

consistent delivery rate of extrudates and hence uniform extruded products. A detailed geometry of screw is described in Fig. 2-11.
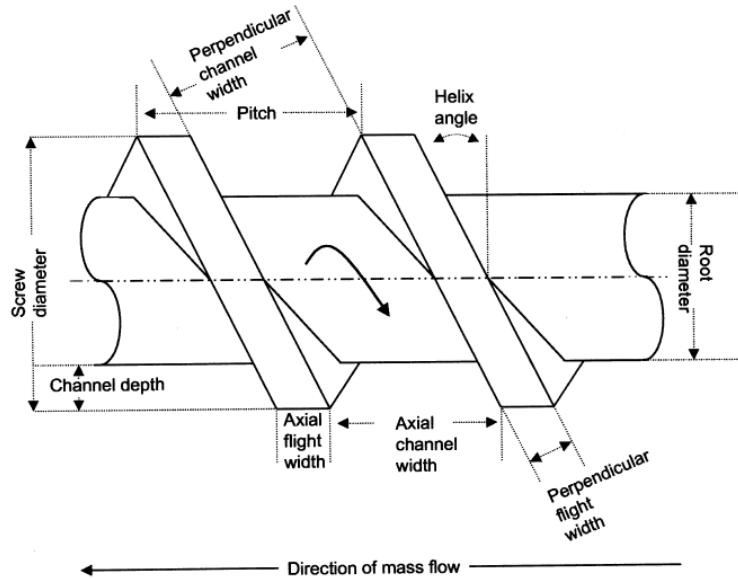
Figure 2-11. A screw geometry [61]**. (copyright @ 2002 Elsevier)**

2.3.1.2   Twin screw extruder

Twin screw extruders are extensively used for compounding polymeric materials with additives and fillers. In general, there are three types of twin screw extruders: (1) intermeshing co-rotating twin screw extruder, (2) intermeshing counter-rotating twin screw extruder, and (3) non-intermeshing counter-rotating twin screw extruder. Due to the rotating motion at the intermeshing zones, intermeshing extruders provide very efficient mixing capability in comparison to single screw extruder. In addition, the intermeshing twin screw extruders exhibit several advantages as follows [58]:

● Improved melting and mixing

● Rapid pressure increase along the screw channel

- Efficient conveying of polymer melt and additives along the screw

- Reduced residence time distribution

- Ease of cleaning when completely intermeshing

The three common types of twin screw extruder are illustrated in Fig. 2-12. The intermeshing co-rotating is broadly used in diverse fields of processing. Large-scale intermeshing co-rotating extruders are employed by resin manufacturers for pelletizing and compounding at great production rates with a screw speed of 200 to 250 rpm. Small-scale extruders are usually operated at lower throughput rates for various processes including glass fibre compounding, blending engineering plastics, devolatilization, and chemical reaction. In comparison to co-rotating extruders, intermeshing counter-rotating extruders exhibit enhanced positive conveying capability, but the maximum operational screw speed is often limited because the greater intermeshing pressure is developed. Small-scale counter-rotating extruders are utilized for final profile/pipe products and colour/filler concentrates at a screw speed lower than 150 rpm. Finally, non-intermeshing counter-rotating extruders are positioned between single screw extruders and intermeshing twin screw extruders in terms of their functions and capabilities. They showed improved mixing performance than single screw extruders, but self-cleaning is not achievable. Non-intermeshing twin screw extruders are often applied for devolatilizing solvents from concentrated polymer solutions [58].
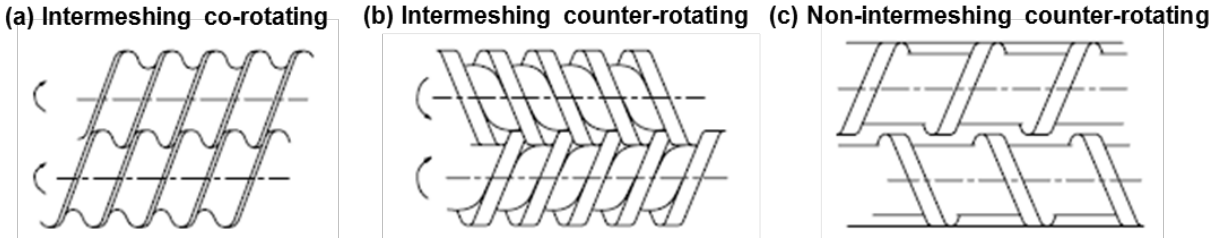
Figure 2-12. Three common types of twin screw extruders: (a) Intermeshing co-rotating, (b) Intermeshing counter-rotating, (c) Non-intermeshing counter-rotating [62]**. (copyright @ 2006 John Wiley and Sons)**

2.3.2   Percolation theory and models

2.3.2.1   Percolation theory

The percolation theory is widely used to understand the principles of forming an electrically conductive network within composite materials where the polymer matrix and the fillers have very different characteristics. The early development of percolation theory was led by Hammersley and Broadbent in 1957. They introduced this theory to explain how the spread of "fluid particles" are influenced by the random properties of a "medium". "Fluid particles" and "medium" can be referred to several different models, such as a solute spreading through the solvent, molecules penetrating a porous solid, and the transport of electrons through an atomic lattice [2].

33
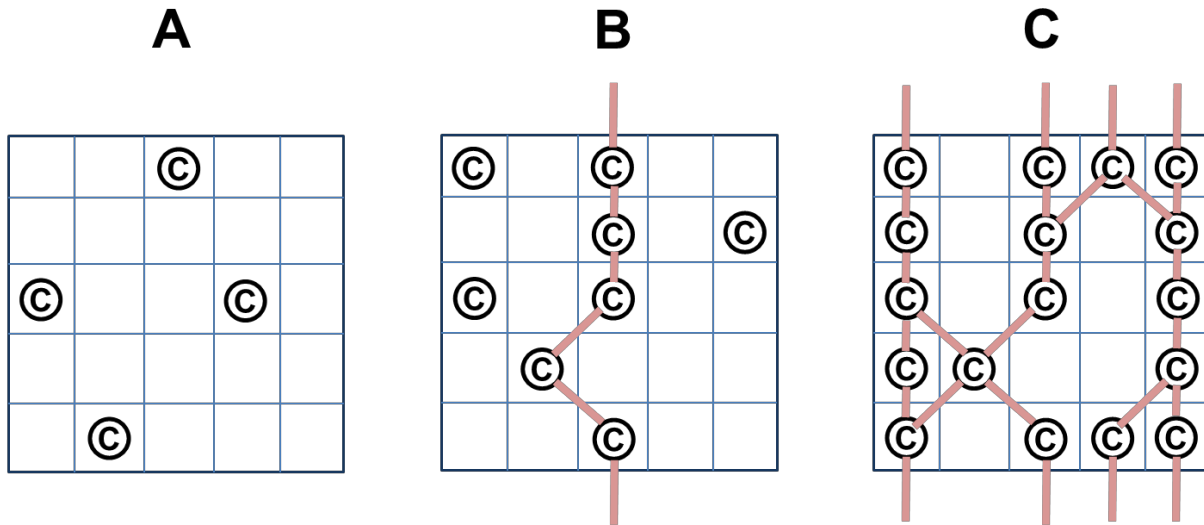
Figure 2-13. The percolation theory development.

One way of understanding the percolation theory is to visualize a large array of lattices as suggested by Stauffer (Fig. 2-13) [63]. The conductive fillers are randomly distributed within the polymer lattice. The lattices occupied by the fillers are denoted ©, and blank sites represent the pure polymer matrix that is not occupied by the conductors. In the beginning (Fig. 2-13a and Fig. 2-14a), the amount of filler added to the matrix is not sufficient, and there does not exist a conductive path that can transport the electrons. At this stage, the electrical conductivity is similar to that of the pure polymer matrix, and the percolation threshold has not been reached yet. When enough amounts of fillers are added, there is a probability that a complete route of transporting electrons is formed, passing through from the bottom to the top of the matrix (Fig. 2-13b and Fig. 2-14b). The specific loading of filler that creates a conductive path is called "percolation threshold". Following a percolation threshold is a regime where a drastic increase in conductivity is achieved by increasing the very small amount of fillers. After this significant increase, the increase in electrical conductivity levels off and eventually reaches the conductivity of fillers (Fig. 2-13c and Fig. 2-14c). This is because the conductive network is complete, and

34

electrons are following the shortest path available to reach the other side.
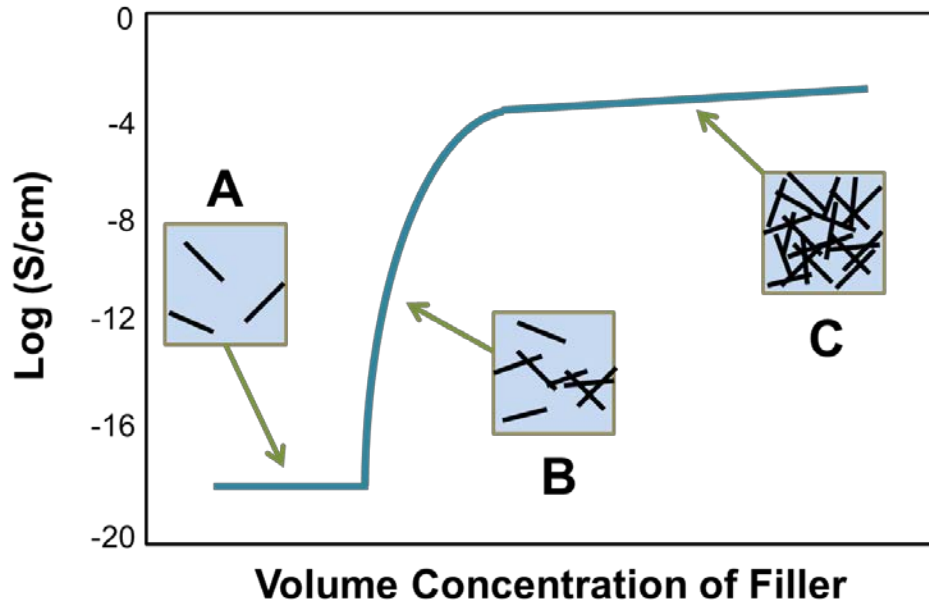
Figure 2-14. Percolation S-Curve.

2.3.2.2   Percolation models

There are many factors that affect the percolation concentration, such as filler distribution, filler shape, the interfacial interaction between the filler and polymer matrix, and processing techniques. By taking these into account, researchers have proposed several percolation models and equations to understand the formation of the conductive network.

2.3.2.2.1 Statistical percolation model

The statistical percolation model occupies the majority of the literature in regard to the electrical percolation phenomenon. This model predicts the conductivity according to the probability of particle contacts within the composite. The breakthrough of the statistical percolation theory in the area of conductive binary mixtures was made by the work of Kirkpatrick [64] and Zallen [65].

According to them, the estimation of percolation concentration begins with finite regular arrays of points and bonds. Typically, such arrays can be a simple cubic lattice. By computer simulation, one is able to predict the fraction of existing points or bonds that exist in a cluster. The points are in contact with one another in the cluster. The percolation point is reached when the cluster spans the boundary of the arrays. To obtain equations that relate conductivity and filler concentration, it is necessary to convert the predicted values into volume fractions. The following equation correlates the electrical conductivity of real mixtures with the volume fraction of the conductive filler:

$$\sigma = \sigma_o(\Phi - \Phi_c)^s \qquad (2\text{-}4)$$

where σ is the electrical conductivity of the mixture, σ_o is the filler conductivity, Φ is the volume fraction of the filler, Φ_c is the percolation threshold, and s is the critical exponent. Although this model is not absolutely accurate in predicting the percolation threshold, it has become the basis for a number of later percolation models.

2.3.2.2.2 Thermodynamic percolation model

Thermodynamic percolation model predicts the conductivity based on the interfacial interactions at the boundary between the individual filler particles and the polymer, particularly by the interfacial tension and the surface energy of the constituents.

Mamunya et al.[66] developed a model that takes filler and polymer surface energies and polymer viscosity into account. This model shows that the percolation behaviour depends on the polymer-filler interaction in addition to the size and amount of the filler material. At all points above the percolation threshold, the conductivity of the composite was determined by the following equations:

$$\log \sigma_m = \log \sigma_c + (\log \sigma_F - \log \sigma_c) \left(\frac{\phi - \phi_c}{F - \phi_c}\right)^k \tag{2-5}$$

$$k = \frac{K \cdot \phi_c}{(\phi - \phi_c)^{0.75}} \tag{2-6}$$

$$K = A - B \cdot \gamma_{Pf} \tag{2-7}$$

$$F = 0.65 \cdot \Phi_c^{1/3} \tag{2-8}$$

where σ_m is the composite conductivity, σ_c is the conductivity at the percolation threshold, σ_F is the conductivity at the maximum loading fraction, F. The volume fraction is represented by Φ, the percolation threshold by Φ_c, interfacial tension by γ_{Pf}, and A and B are constants. The value R is determined by the filler volume fraction, percolation threshold, and the interfacial tension as calculated by the Fowkes equation [67]:

$$\gamma_{Pf} = \gamma_P + \gamma_f - 2(\gamma_P \gamma_f)^{\gamma_2} \tag{2-9}$$

where γ_P is the surface energy of the polymer and γ_f is the surface energy of the filler. Although the filler is limited to carbon black, this model shows a good agreement between the calculated values and the experimental data for many different polymers filled with carbon black.

2.3.2.2.3 Geometrical percolation model

Geometrical percolation model was proposed to predict the conductivity of sintered mixtures of conducting and insulating powders. In this model, it is generally assumed that during the sintering process, the insulating powders form regular cubic particles while the conductive materials arrange in a regular manner on the surfaces of these insulating particles. The main parameters in this model include the diameters of non-sintered powder particles or the edge length of the sintered particles and diameter of the conducting particles.

The most well-known model in this class is the one developed by Malliaris and Turner [68]. They derived two equations for volume percolation concentration. The first one calculates the percolation threshold (Φ_c) and the second equation predicts the volume fraction at the end of conductivity improvement as follows:

$$\Phi_c = 0.5 p_c V \tag{2-10}$$

$$V = 100 \left[\frac{1}{1 + \left(\frac{\theta \cdot D}{4d} \right)} \right] \tag{2-11}$$

where D is the diameter of the insulating powder particles, and d is the diameter of conducting particles. θ is a quantity to estimate the arrangement of conductive fillers on the surfaces of the insulating ones; θ=1.11 for hexagonal, 1.27 for cubic, 1.375 for triangular arrangements. P_c is the first non-zero probability for the occurrence of infinitely long bands of conductive particles on the surfaces of the insulating particles; P_c is 1/3 for hexagonal, 1/2 for cubic, and 2/3 for the triangular array.

2.3.3   Application areas

Conductive polymer nano-composites fabricated by compounding can be applied in a variety of fields, such as electromagnetic interference (EMI) shielding, electrostatic dissipation (ESD), and bipolar plates for PEMFC.

2.3.3.1   Electromagnetic interference (EMI) shielding

The rapid growth of electronic devices has increased the need for injection mouldable thermoplastics for packaging and structural components. Many of these electronic devices must be protected against EMI. EMI is radiation with adverse influences on the performance of

electronic devices. Although EMI exists across the entire electromagnetic spectrum, the majority of EMI problems are associated with the part of the spectrum between 25 kHz and 10 GHz. This portion is known as the radio frequency interference (RFI) area and corresponds to radio and audio frequencies [1].

Conventionally, metals and metallic composites are employed as EMI shielding materials, but they suffer from oxidation, corrosion, poor chemical resistance, high density, and difficulty in processing. This has raised a considerable attention to polymer composite that contains conductive fillers. Such polymer composites are expected to demonstrate numerous advantages including high chemical resistance, great processibility, and wide absorption bandwidth. In addition, lightweight and flexibility of polymer composites are highly favourable for effective and practical EMI shielding applications, especially in the areas of aircraft, spacecraft, automobiles, and next-generation portable and wearable electronic devices. It should be noted that for effective EMI shielding, the minimum conductivity required is greater than 1 S/m [69].

2.3.3.2 Electrostatic discharge (ESD)

Electronic components are vulnerable to damages from electrostatic discharge. The annual losses in products containing sensitive electronic components owing to ESD during manufacturing, assembly, storage, and shipping have been estimated in billions of dollars [1]. With rapid miniaturization, electronic components have become increasingly susceptible to ESD. Moreover, since insulating plastics are largely used in manufacturing and packaging of electronics, sufficiently accumulated charge has the possibility of a sudden discharge resulting in damage to sensitive electronic components.

Many different materials with a range of electrical conductivity have been developed to package

sensitive electronic devices and prevent damages during storage and shipping. The Electronic Industry Association (EIA) classified packaging materials into conductive, dissipative, and insulating based on their surface resistivity [1]. According to EIA, conductive materials have a surface resistivity less than 1.0×10^5 Ω/sq, dissipative materials between $1.0 \times 10^5 \sim 1.0 \times 10^{12}$ Ω/sq, and insulating materials have a surface resistivity larger than 1.0×10^{12} Ω/sq. For many ESD applications, the optimal surface resistivity is in the range of 10^6 to 10^9 Ω/sq. Materials with too low resistivity may result in uncontrolled discharge.

2.3.3.3 Bipolar plates for polymer electrolyte membrane fuel cells (PEMFC)

One of the largest applications of conductive polymer composite in the area of energy storage device is to replace conventional graphite bipolar plates in PEMFC. Graphite has been used for manufacturing bipolar plates for many years due to its numerous suitable characteristics such as excellent electrical conductivity and corrosion resistance that leads to high electrochemical power output [70]. However, graphite bipolar plates suffer from its porosity, poor mechanical strength, high machining difficulty and production cost. The porous structure makes the plate brittle and allows reactant gases to permeate through the channels. Therefore, the graphite bipolar plates are impregnated by resins to seal the pores. This post-processing also increases the production cost for bipolar plates. Also, the machining is required to form the flow channels, which adds to the cost of manufacturing cost. To address these issues, scientists and engineers have been investigating to develop an alternative material to replace graphite [71].

Since the bipolar plates are required to perform a number of different functions, the material for bipolar plates should exhibit specific electrical, thermal, and mechanical properties. The target values have been set up by the Department of Energy (DOE) in US and detailed below [72].

1. High electrical conductivity: The high electrical conductivity is the most essential property of bipolar plate. The electrical conductivity of 100 S/m or higher has been set up by the DOE.

2. High thermal conductivity: The bipolar plates should be highly thermally conductive to maintain a uniform temperature distribution and to prevent hotspots on the membrane. The thermal conductivity must be greater than 20 $Wm^{-1}K^{-1}$.

3. Gas impermeability: The bipolar plates must be highly impermeable to gases to avoid potentially dangerous gases and performance-degrading leaks. The gas permeability should be less than 10^{-4} cm^3/s-cm^2.

4. Corrosion resistance: The operation environment for bipolar plates is favourable for corrosion; the bipolar plates are exposed to warm and high humidity with a range of electrical potentials. Thus the bipolar plates should be of highly corrosion resistive. The acceptable corrosion is 1.6 x 10^{-3} mA/cm^2 per 5000 hr.

5. High mechanical strength: Since the bipolar plates are physically forceful and support the thin components in the cell, the materials must have appropriate mechanical properties (rigidity, tensile strength, and flexural strength) and must not warp. The flexural strength and tensile strength for bipolar plates should exceed 59 MPa and 41 MPa, respectively.

6. Thin and lightweight materials: To achieve the target power level for certain applications, a number of cells are assembled in a fuel cell stack. This requires many bipolar plates to accommodate the flow channels and maintain mechanical stability. The maximum weight of a bipolar plate should be less than 400 g/kW.

7. Low cost and ease of manufacturing: When many bipolar plates are required for a fuel cell

stack, the bipolar plate costs should be low to minimize the total cost of fuel cell. The cost should be less than $25/kW.

8. Environmentally benign: If fuel cell components including bipolar plates are recyclable, they should be highly preferable.

3. Characterization Techniques

3.1 Physicochemical characterizations

3.1.1 Scanning electron microscope (SEM)

Scanning electron microscopy (SEM) is an important characterization technique that allows high-resolution inspection of the morphology of a material in the micro and nano-scale. SEM employs an electron beam focused on the sample's surface to characterize its topology and the sample's morphology. This technique is particularly useful as the electron source has an extremely small wavelength, which allows production of high-resolution images of nano-structured materials. The electron gun emits electrons which are then bombarded onto the sample. Upon interaction of the electrons with the sample's surface, secondary and backscattered electrons are either generated or reflected, which are then captured by the detector above the sample. The detected electrons are converted into an electric signal and processed by a computer to produce the final image.

3.1.2 Transmission electron microscope (TEM)

Transmission electron microscopy (TEM) is one of the essential physical characterization techniques, which allows direct visualization of the sample's morphology similar to SEM. TEM also utilizes an electron beam as the source to create high-resolution images. However, unlike in SEM which detects backscattered or reflected electrons above the sample, TEM detects electrons, which are transmitted through a thin sample and then converted to an electric signal, to produce the final image. TEM will allow investigation of internal morphologies of materials.

3.1.3 X-ray diffraction (XRD)

X-ray diffraction (XRD) is a useful characterization technique which allows the determination of crystal structure. The x-rays from the source interact with the sample to produce diffraction patterns at the angles corresponding to specific crystal planes. The x-ray source is swept over a range of angles and the diffracted x-rays at specific angles are collected and processed by the detector. The angle of diffraction is related to the specific crystal orientation of the sample by Bragg's law as follows:

$$2\mathrm{d}\sin\theta = \mathrm{n}\,\lambda \tag{3-1}$$

where n, λ, d, and θ represent the order of the spectrum (any integer), the wavelength of the X-rays, the spacing between diffracting planes, and the incident angle, respectively. The diffraction pattern at specific angles obtained by XRD can be compared to the theoretical diffraction pattern calculated by the crystal planes to help identify the material. Therefore, XRD patterns cannot be produced by amorphous materials as they do not have ordered crystal planes that interact with X-rays to produce diffracted patterns.

3.1.4 Raman spectroscopy

Raman spectroscopy is a spectroscopy technique based on inelastic scattering of monochromatic light, usually from a laser source. Inelastic scattering means that the frequency of photons in monochromatic light changes upon interaction with a sample. Photons of the laser light are absorbed by the sample and reemitted. The frequency of the re-emitted photons is shifted up or down in comparison with original monochromatic frequency. This shift provides information in regard to vibrational, rotational and other low frequent transitions in molecules [73]. Examining samples in fast and non-destructive manner, Raman spectroscopy has become a powerful method

to characterize graphene and related materials [74]. It is widely used in the field of carbon-based nano-structures to characterize the structural properties of carbonaceous materials, including disorder and defect structures.

3.1.5 Differential scanning calorimetry (DSC)

Differential scanning calorimetry (DSC) is a thermo-analytical technique that detects the heat flow caused by thermal events of materials as a function of temperature. In a DSC measurement, the sample and a reference, which are placed on individual conducting bases, are heated at a constant rate and the temperatures of both are maintained the same. During the thermal event of the sample, heat is either absorbed or released, leading to a temperature difference between the sample and the reference. The heat supply is adjusted accordingly to compensate the temperature difference, and the corresponding heat flux is measured precisely and plotted versus temperature. DSC is broadly employed to measure materials' properties including glass transition, phase changes, melting, crystallization, curing kinetics, and so on.

3.1.6 Thermo-gravimetric analysis (TGA)

Another widely used thermo-analytical technique is thermo-gravimetric analysis (TGA) that meters variation in sample mass as a function of temperature under the desired environment. The analysis is carried by measuring the specimen mass with a microbalance while increasing the temperature at a controlled rate in a furnace under an inert or oxidative atmosphere. TGA is widely used to characterize the materials composition, decomposition patterns, thermal stability, and degradation kinetics.

3.2 Mechanical property characterizations

3.2.1 Tensile strength measurement

The mechanical characterizations in this research include tensile and flexural strength tests. Tensile strength is a measurement of the force required to pull a material to the point where it breaks. The tensile strength of a material is the maximum amount of tensile stress that it can take before failure and is measured according to ASTM D638-14 "Standard Test Method for Tensile Properties of Plastics". Young's modulus is estimated from a slope of the stress-strain curves where a distinct linearity appears at the initial portion of the curve.

3.2.2 Flexural strength measurement

Flexural strength (three-point flexural test) is a material's property to resist failure in bending. The flexural strength is tested in accordance with ASTM D790-03 "Standard Test Methods for Flexural Properties of Unreinforced and Reinforced Plastics and Electrical Insulating Materials". According to ASTM D790-03, the flexural strength (σ_f) is calculated by the following equation:

$$\sigma_f = \frac{3PL}{2bd^2} \tag{3-2}$$

where P is the load at the yield, L is the span length, b is the width and d is the thickness of the sample. Flexural modulus (E_B) is estimated with a slope (m) of the load-deflection curves where a clear linearity is present at the initial portion of the curves and is calculated by the following equation:

$$E_B = \frac{L^3 m}{4bd^3} \tag{3-3}$$

where L is the span length, m is the slope of the load-deflection curve, b is the width, and d is the

thickness of the sample.

3.3　Electrical conductivity measurements

3.3.1　In-plane electrical conductivity

The in-plane electrical conductivity (σ_I) of samples is obtained by employing a four-point probe setup equipped with two multi-meters and DC power supply. The sheet resistance (R_s) is measured by measuring the voltage drop when a constant current is applied. One multi-meter (Agilent 3441 1A multi-meter) measures the current and the other multi-meter (Agilent 3440 1A multi-meter) measures the voltage drop as described in Fig. 3-1a. The electrical conductivity (σ_I) is calculated as follows:

$$\sigma_I = \frac{1}{\rho} = \frac{1}{R_s t} = \left(\frac{ln2}{\pi t}\right)\frac{I}{V} \, \Omega \, cm \tag{3-4}$$

where ρ is the electrical resistivity, t is the sample thickness, I is the applied current, and V is the measured voltage drop [75].

3.3.2　Through-plane electrical conductivity

The through-plane electrical conductivity (σ_T) is measured by a two-probe setup connected with two multi-meters and DC power supply. The specimen is placed in a fixture designed in our laboratory where the specimen is kept at a consistent pressure. The composite specimen is placed between copper foil electrode, and a conductive carbon tape is used to improve the contact surface between the electrodes and the specimen as shown in Fig. 3-1b. The electrical resistance (R) is obtained by dividing voltage drop by the current applied. The through-plane electrical conductivity (σ_T) is obtained by as follows:

$$\sigma_T = \frac{t}{R \times A}$$

(3-5)

where R is the electrical resistance, t is the sample thickness, and A is the area of the specimen [76].
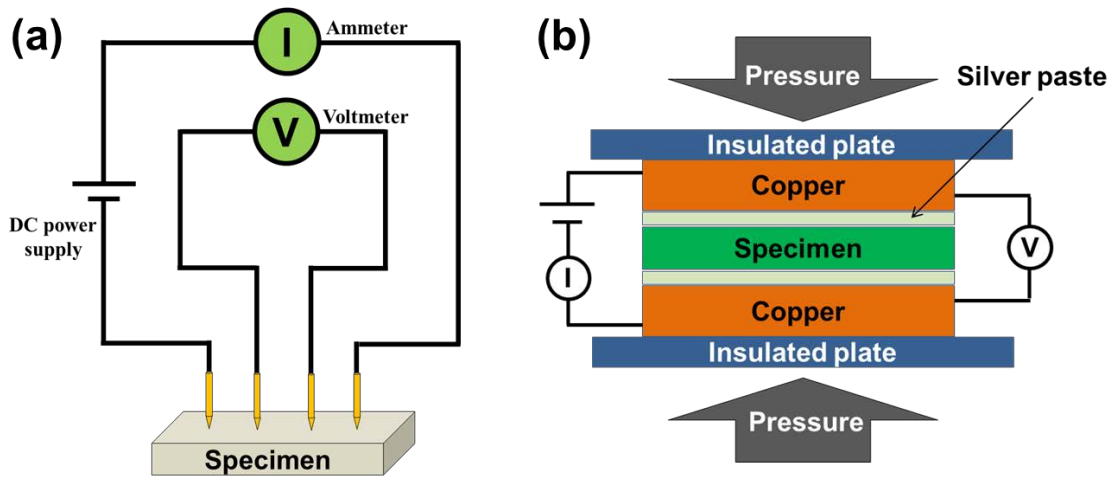
Figure 3-1. The schematic diagrams of measurement setup for (a) in-plane and (b) through-plane electrical conductivity.

4. Highly Conductive and Interconnected Graphene Foam Based Polymer Composites

This chapter is reprinted in adapted form from the article below with permission from Elsevier.

Jun YS, Sy S, Ahn W, Zarrin H, Rasen L, Tjandra R, et al. "Highly conductive interconnected graphene foam based polymer composite", *Carbon*, 2015;95:653–8.

4.1 Introduction

Due to its extraordinary thermal, mechanical, and electrical properties, graphene has been excellent nano-fillers to be integrated into polymers [77]–[81]. The conventional methods for integrating graphene sheets include melt-blending, solution-blending, and *in-situ* polymerization [82]. When combined into polymers by such approaches, however, the exceptional properties of graphene were only partly imparted. The strong π-π interaction triggered agglomeration or restacking of graphene sheets during the fabrication process, which leads to poor dispersion in macromolecules. This resulted in inferior nano-architecture, hindering the full recognition of the exceptional properties of graphene.

To prevent the above-mentioned problems, it was necessary to develop a three-dimensional graphene network that does not suffer from restacking or agglomeration [9], [83]. Polymers were then subsequently infiltrated into graphene foam. Because such composites inherit the unique inter-connected graphene sheets, a high electrical conductivity was achieved as compared to those fabricated by conventional methods. For instance, Tang et al. prepared graphene foam and infiltrated it with epoxy resin. This composite exhibited an electrical conductivity of 0.04 S/m at a loading of only 0.21 vt% [84]. This is nine orders of magnitude higher than those prepared by

solution blending. Further Z. Chen et al. infiltrated polydimethylsiloxane (PDMS) into graphene foam prepared by CVD, and this composite exhibited an electrical conductivity of 1000 S/m with a loading of 0.5 wt% [10]. Moreover, M. Chen et al. demonstrated graphene/multi-walled carbon nanotube (MWCNTs) foam combined with PDMS that reached an electrical conductivity of 280 S/m at a loading of 1.3 wt% [85]. These studies clearly demonstrate recent advancements in the infiltration of polymer materials into three-dimensional graphene foam for improved performance.

Although significant improvements have been achieved, very few studies have linked the physical characteristics of graphene sheets with the electrical conductivity of the infiltrated-composites. When the graphene foam is prepared via chemical oxidation of graphite, it is essential to fully understand the influence of the starting materials' characteristics when integrated into polymers. Thus, in this study, the impact of graphene sheet size on the electrical conductivity of the final composites has been explored. The graphene foam was prepared from large flake graphite (LFG) and small flake graphite (SFG), respectively and subsequently infiltrated with PDMS. The graphene-PDMS (G-PDMS) composite produced from LFG exhibited an in-plane electrical conductivity of ~3.2 S/m with a loading of 0.4 wt%, which is more than two orders of magnitude greater than those made from SFG (~1.4 x 10^{-2} S/m at a loading of 1.9 wt%). A variety of characterizations including XRD, Raman spectroscopy, SEM, TEM, and electrical conductivity measurement have been performed to justify the advantages of using LFG in the fabrication of graphene-based composites.

4.2 Experimental procedures

4.2.1 Materials and methods

Large flake graphite (LFG, >100 μm) and small flake graphite (SFG, 2-15 μm) were purchased from Grafoid Inc. and Alfa-Aesar Inc., respectively. Sulfuric acid, phosphoric acid and hydrogen peroxide (30%) were acquired from Sigma Aldrich. Potassium Permanganate was obtained from EMD Chemicals. PDMS (Sylgard 184 silicone elastomer) was bought from Dow Corning Inc.

4.2.2 Preparation of GO, RGO foams, and G-PDMS composite
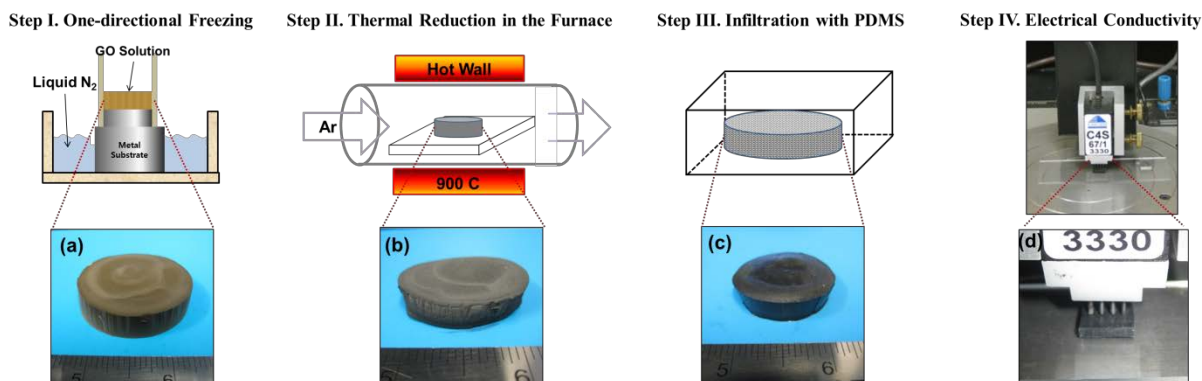
Figure 4-1. Schematic illustrating G-PDMS fabrication procedure followed by electrical conductivity measurement. Optical images of (a) GO foam, (b) RGO foam, (c) G-PDMS composite, and (d) a sliced slab of G-PDMS on a probe fixture. (Graphene-based foams measured in inches).

Fig. 4-1 illustrates the experimental procedures and images of the graphene foams at each stage of preparation. A modified Hummer's method was used to prepare GO solution from LFG and SFG, respectively, and described elsewhere [86]. The prepared GO solution was poured into a house-built mould. The lower component of the mould was immersed in a pool of liquid nitrogen, introducing a unidirectional temperature gradient to the GO solution (Fig. 4-1a). The frozen GO solution was freeze-dried for 72 hr. The freeze dryer was kept at -40 °C with a pressure lower

51

than 0.1 mbar. The freeze dried GO foam was thermally reduced in a furnace at 900 °C (Fig. 4-1b). The reduced graphene oxide (RGO) foam was then infiltrated with PDMS as follows (Fig. 4-1c). Sylgard 184 silicone elastomer base was mixed with its curing agent with 10:1 ratio. The mixture was degassed in a vacuum oven at room temperature for 30 min and infiltrated into the foam. The infiltration was carried out at room temperature without applying vacuum, and the foam did not suffer from any deformation during this process. The infiltrated graphene-PDMS (G-PDMS) composites were sliced into small slabs (0.9 x 0.9 x 0.1 cm) and their electrical conductivities were measured either by a standard 4 point probe station (Fig. 4-1d) for in-plane conductivity or a potentiostat for through-plane conductivity. Table 4-1 shows the G-PDMS composites prepared in this study.

Table 4-1. G-PDMS composites prepared in this study.

Composites	Graphite Size (μm)	GO Conc. (mg/mL)	Loading (wt%)
G-PDMS-1		5.8	0.4
G-PDMS-2	Large (>100)	11.5	0.5
G-PDMS-3		18.0	0.6
G-PDMS-4		25	1.9
G-PDMS-5	Small (2~15)	35	1.6
G-PDMS-6		45	2.2
G-PDMS-7*	Small (2~15)	-	4.0

* G-PDMS-7 was prepared by mechanical mixing of RGO powder from SFG with PDMS

4.2.3   Characterizations

The GO and RGO foams, as well as G-PDMS, were analyzed by SEM (Zeiss LEO 1550) for morphology analysis. Individual graphene sheet and their size were observed by TEM (JEOL 2010F) for size verification. XRD (Brunker AXS D8 Advance) was used to study the crystal

structures of GO and RGO foams. Raman spectroscopy (Bruker Senterra, 532nm) was employed to analyze the defects and disorders of GO and RGO foams.

4.2.4 Electrical conductivity measurement

4.2.4.1 In-plane electrical conductivity

The in-plane electrical conductivity (σ_I) of samples was obtained by employing a four-point probe setup equipped with a probe fixture (Cascade Microtech Inc.) and a source meter (Keithley 2440 5A Source Meter, Keithley Instruments Inc.). The sheet resistance (R_s) was measured by measuring the voltage drop when a constant current was applied. The electrical conductivity (σ_I) was calculated by Eq. (4-1):

$$\sigma_I = \frac{1}{\rho} = \frac{1}{R_s t} = \left(\frac{ln2}{\pi t}\right)\frac{I}{V} \, \Omega cm \tag{4-1}$$

where ρ is the electrical resistivity, t is the sample thickness, I is the applied current, and V is the measured voltage drop.

4.2.4.2 Through-plane electrical conductivity

The through-plane electrical conductivity (σ_T) was measured by a two-probe setup connected with a multichannel potentiostat (Princeton Applied Research, VersaSTAT MC). The specimen was placed in a fixture designed in our laboratory where the specimen was kept under a consistent pressure. The composite specimen was placed between copper foil electrodes, and a conductive carbon tape was used to improve the contact surface between the electrodes and the specimen. The electrical resistance (R) was obtained by dividing voltage drop by the current applied. The through-plane electrical conductivity (σ_T) was obtained by Eq. (4-2):

$$\sigma_T = \frac{t}{R \times A} \qquad (4\text{-}2)$$

where *R* is the electrical resistance, *t* is the sample thickness, and *A* is the area of the specimen.

4.3   Results and discussion

4.3.1   Material characterizations
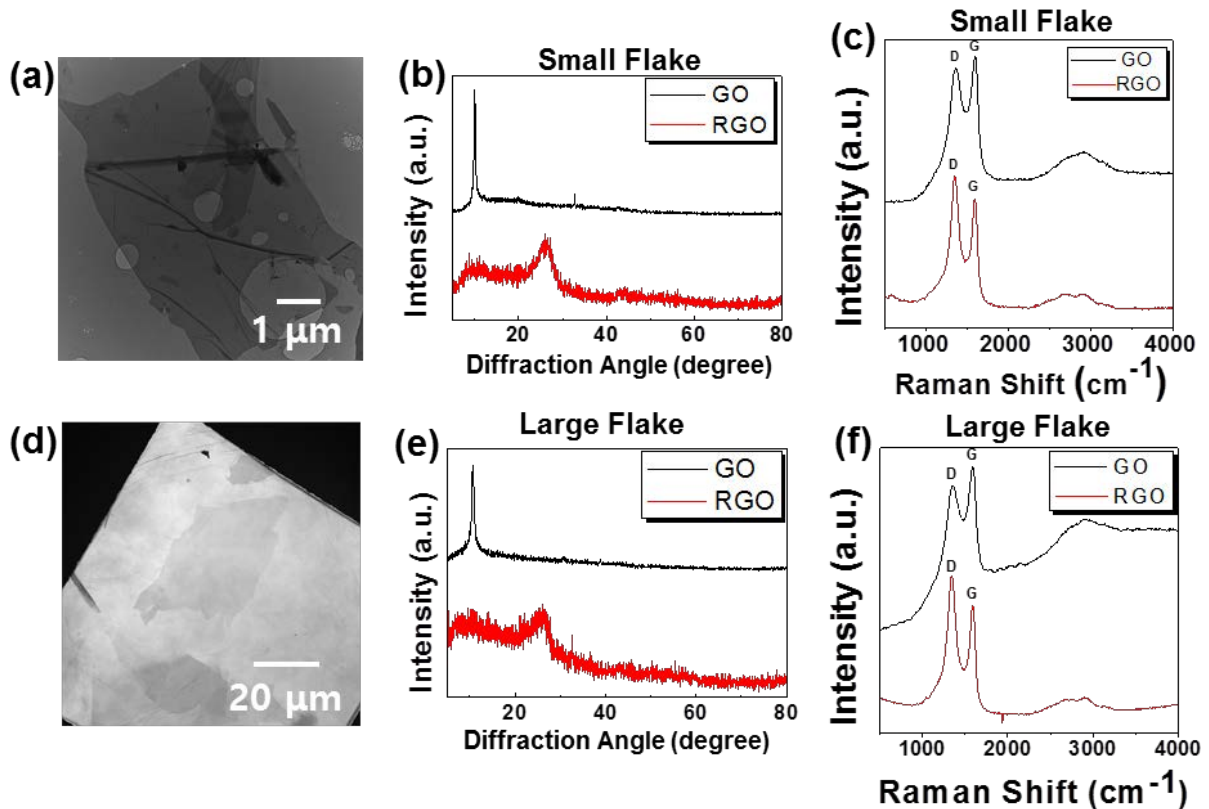
Figure 4-2. The TEM images of GO from (a) SFG and (d) LFG. XRD peaks for GO and RGO foams from (b) SFG and (e) LFG, respectively. Raman spectra for GO and RGO foams from (c) SFG and (f) LFG.

In Fig.4-2 TEM images of GO sheets produced from (Fig. 4-2a) SFG and (Fig. 4-2b) LFG are shown, respectively. It is clear that the individual sheet sizes of GO produced from LFG are

54

considerably greater than that of GO synthesized from SFG. The diagonal graphene sheet size from SFG spans about 10 μm, while the sheet size from LFG reaches 100 μm. It should be pointed out that when imaging GO sheets from LFG, one of the smallest GO was chosen for appropriate image since the majority of GO sheets covered the entire TEM grids (200 mesh).

The XRD peaks for GO and RGO foams produced from (Fig. 4-2b) SFG and (Fig. 4-2e) LFG are presented in Fig. 4-2 to gain insight into their structural evolution. The interlayer distance (Å) was calculated by Bragg's law, and the number of layers was estimated from Scherrer-Debye equation (4-3):

$$ L_c = \frac{0.89\,\lambda}{\beta\,cos(\theta)} \qquad (4\text{-}3) $$

where λ is the wavelength of X-ray, β is the Full Width at Half Maximum of peak [87]. The interlayer distance from the peak of GO for SFG and LFG are 8.83 Å (2θ=10.01°) and 8.27 Å (2θ=10.68°), respectively. This is attributed to the formation of functional groups during oxidation [88]. Upon thermal reduction, the interlayer distance for RGO foam SFG and LFG contract to 3.44 Å (2θ=25.92°) and 3.50 Å (2θ=25.43°), respectively owing to the removal of functional groups. Furthermore, the estimated number of layers for GO foams from SFG is ~19, and this is further reduced to ~7 after the thermal reduction. For LFG, ~15 layers are calculated to be in the GO foams and ~7 layers of RGO foams. This confirms that thermal reduction triggers additional exfoliation of the graphene layers.

Raman spectroscopy is widely used to characterize the structural properties of carbonaceous materials, including disorder and defect structures [89]–[91]. To further compare the order/disorder degree on the graphene sheets produced from different graphite, Raman spectra for GO and RGO foams synthesized from (Fig. 4-2c) SFG and (Fig. 4-2f) LFG are described in

Fig. 4-2. The G band is associated with C-C bond stretching and the D band is attributed to disorders or defects in the graphene sheets. The relative intensity ratio of both peaks (I_D/I_G) is frequently used as a measure of disorder degree. The I_D/I_G ratio for RGO from SFG is 1.32, while the ratio for RGO from LFG is 1.17. An appropriate quantification of a number of defects can be obtained by integrating the relative intensity ratio into Tuinstra & Koenig equation to estimate the inter-defect distance (L_a) as follows in Eq. (4-4):

$$L_a = \left(2.4 \times 10^{-10}\right) \lambda^4 \left(\frac{I_D}{I_G}\right)^{-1}$$
(4-4)

where λ is the excitation laser wavelength (532 nm) [92]. The inter-defect distance of RGO from LFG was 16.45 nm, and this is higher than that of RGO foam from SFG (14.56 nm). The higher inter-defect distance (L_a) indicates the lower amount of defects on the graphene sheets. Several defects are associated with a number of edge structures of graphene sheets present in the bulk of nano-composite. The use of LFG reduces the total amount of edge structures in bulk RGO foam. Thus, the higher L_a value obtained for RGO from LFG indicates a lesser amount of defects on graphene sheets leading to an improved intrinsic electrical conductivity. This contributes to the attainment of higher overall electrical conductivity when RGO foam is made from LFG. The parameters calculated from XRD peaks and Raman spectra are summarized in Table 4-2.

Table 4-2. Parameters estimated from XRD peaks and Raman spectroscopy.

Graphite Size	Materials	XRD					Raman Spectroscopy	
		2θ degree	Interlayer Distance (Å)	FWHM (radian)	L_c(Å)	Number of layers	I_D/I_G	L_a (nm)
Small	GO	10.01	8.83	0.00821	169.45	19.20	0.97	19.91
	RGO	25.92	3.44	0.05637	25.43	7.33	1.32	14.56
Large	GO	10.68	8.27	0.01110	125.44	15.16	0.96	20.11
	RGO	25.43	3.50	0.05364	26.49	7.57	1.17	16.45

4.3.2 Morphology of RGO Foam and G-PDMS Composites

The cross and lateral sections of the RGO foams prepared from SFG and LFG are imaged and shown in Fig. 4-3a-d and Fig. 4-3e-h, respectively. The SEM images at low magnification confirm that RGO foams are highly porous, and this structure promises a number of future applications by infiltrating with polymers. The SEM images for lateral sections of RGO foams reveal that the pores are randomly distributed, but the graphene sheets are well oriented. It is clearly shown that the graphene sheets are aligned along the direction of freezing (arrow) for both sizes of graphite. This confirms that one directional freezing method is an effective way of producing graphene foams exhibiting well-ordered graphene sheets. The SEM images at higher magnifications clearly demonstrate that RGO foams from LFG consist of graphene sheets greater in size as compared to those from SFG. This is in line with TEM images showing that GO produced from LFG consists of larger size graphene sheets. Furthermore, the graphene sheets from SFG display more wrinkles in comparison to the graphene sheets from LFG, probably due to higher defect ratio as indicated by Raman spectra. The graphene sheets from LFG appear to be flatter and less crumpled. This more flat-like and less wrinkled graphene sheets from LFG

contribute to reaching higher electrical conductivity for G-PDMS.
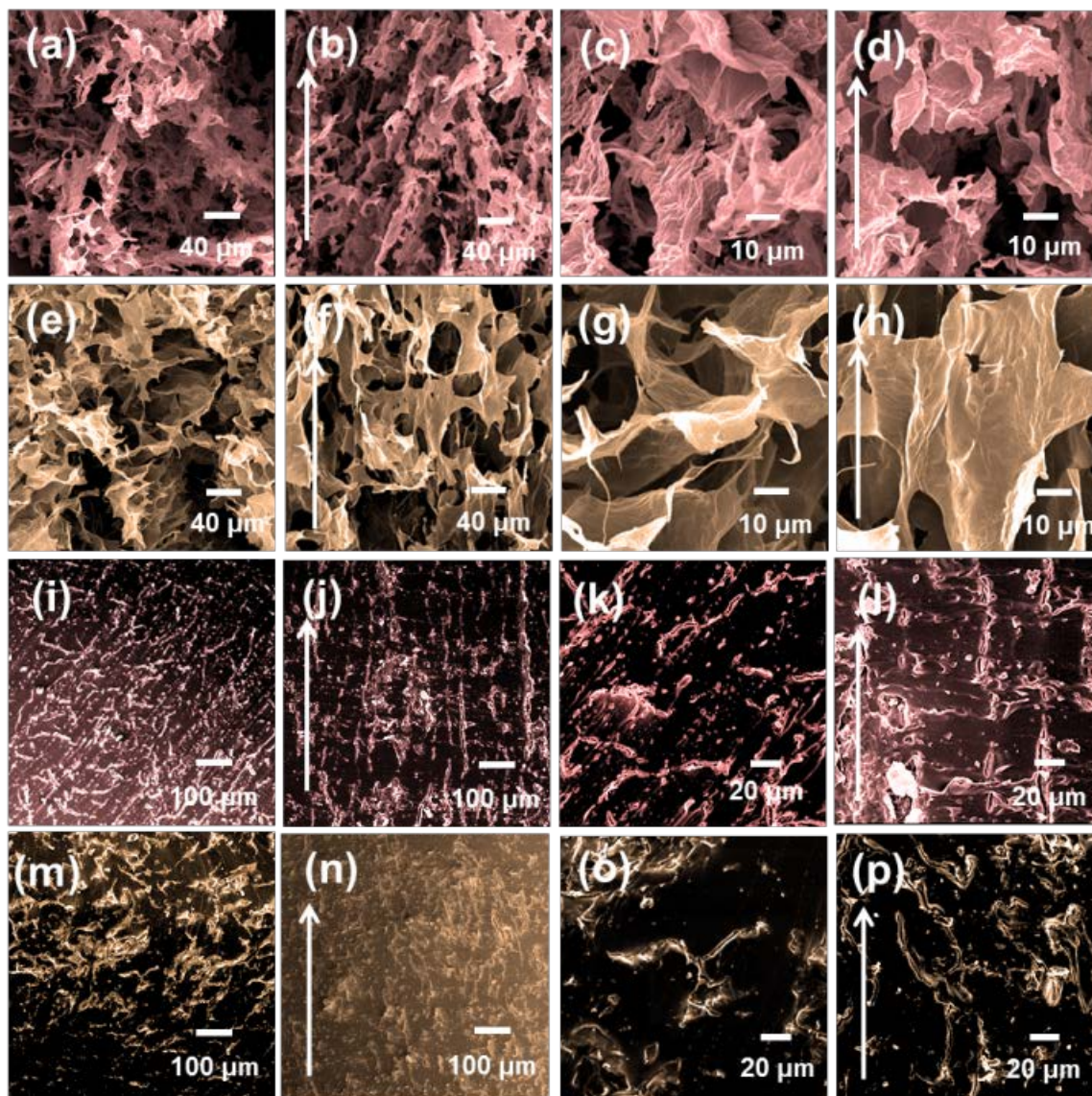
Figure 4-3. The SEM image of RGO foams from SFG for (a and c) cross and (b and d) lateral section. RGO foams from LFG for (e and g) cross and (f and h) lateral sections. G-PDMS composites from SFG for (i and k) cross and (j and l) lateral sections. G-PDMS composites from LFG for (m and o) cross and (n and p) lateral sections. The arrows indicate the direction of freezing

The SEM images of G-PDMS composite demonstrate its combined structure of graphene sheets with PDMS (Fig. 4-3i-p). The graphene networks that provide the electrical conductivity of the

composite are clearly observed. The larger size of graphene sheets is observed in the images of G-PDMS from LFG (Fig. 4-3m-p) as compared to G-PDMS from SFG (Fig. 4-3i-l). It is also evident that the pores of the RGO foams are completely filled with PDMS and the graphene sheets are well distributed in the G-PDMS. The alignment of graphene sheets along with the direction of freezing is also clearly presented in the SEM images for the lateral section. This suggests that RGO foams retain its unique structure after being filled with PDMS, and the infiltration of PDMS does not introduce any discernable deterioration or inhomogeneity to the structure of the RGO foams. Therefore, this method allows the fabrication of flexible and electrically conductive conductors that overcome the problems of agglomeration and segregation of graphene sheets in the polymer-combined composites [83], [93].

4.3.3   Electrical conductivity of G-PDMS composites

The (a) in-plane and (b) through-plane electrical conductivity of all the prepared G-PDMS composites is illustrated in Fig. 4-4. G-PDMS composites based on LFG show significant enhancements in both in-plane and through-plane electrical conductivity. The G-PDMS-1 exhibits an in-plane electrical conductivity of ~3.2 S/m with a loading of 0.4 wt% while the G-PDMS-4 shows ~1.4 x 10^{-2} S/m with a loading of 1.9 wt%. This more than two orders of magnitude gap is a significant difference considering the fact the loading of graphene of small size is four times higher than that of large size. The G-PDMS composites originated from LFG also showed improved through-plane electrical conductivity (Fig. 4-4b). The G-PDMS-2 shows a through-plane electrical conductivity of ~3.2 x 10^{-2} S/m with a loading of 0.5 wt% whereas the G-PDMS-4 shows ~5.0 x 10^{-3} S/m with a loading of 1.9 wt%. This significantly improved electrical conductivity is mainly attributed to the fact that G-PDMS-1, G-PDMS-2, and G-PDMS-3 consisted of the greater size of individual graphene sheets (~100 μm), which is 10 times

larger than the small size graphene (~10 μm) is. Furthermore, although the in-plane electrical conductivity of G-PDMS is reduced with the use of SFG (G-PDMS-4, 1.4 x 10^{-2} S/m with a loading of 1.9 wt%), it is still significantly higher than G-PDMS-7 (4.2 x 10^{-5} S/m with a loading of 4.0 wt%), which was prepared by mechanical mixing RGO powder made from SFG and PDMS. This was also observed in through-plane electrical conductivity. This indicates that the inter-connected graphene foam provides more efficient paths for electron transfer inside the polymer than conventional graphene powder. In addition, the electrical conductivity does not significantly vary with a change of loading of graphene in the composite. For polymer composites fabricated by conventional methods, the percolation theory plays an important role in the relationship between the loading of conductive filler and the electrical conductivity [94]. However, the G-PDMS composites retain the three-dimensionally inter-connected network of graphene, and once the network is formed, the electron can be moved freely along the graphene network inside the polymer matrix. Thus the popular percolation theory does not play a role for this graphene foam infiltrated composite [84].
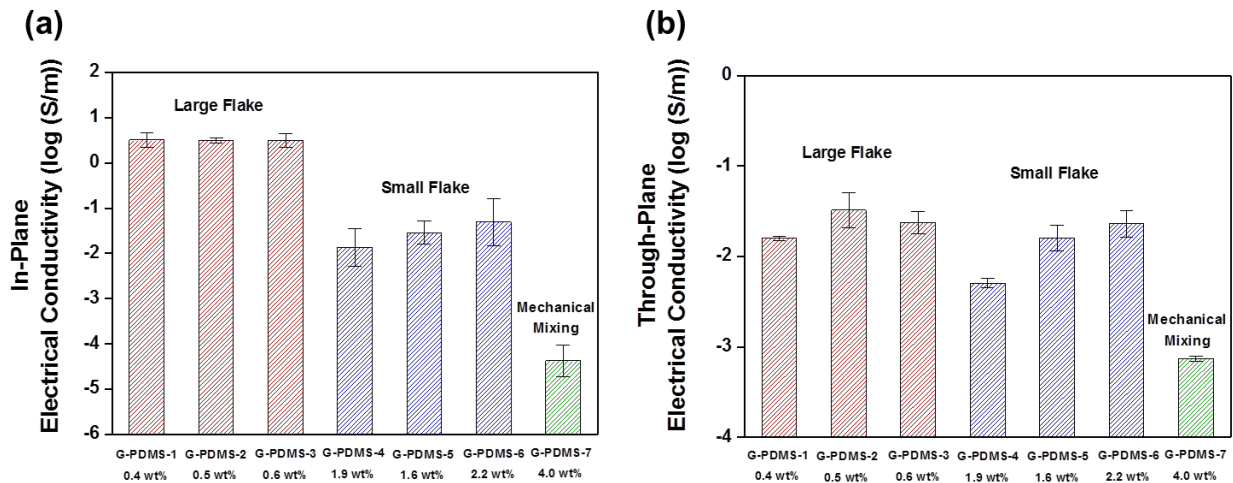
Figure 4-4. (a) In-plane electrical conductivity (σ_I) and (b) Through-plane electrical conductivity (σ_T) of G-PDMS composites produced from LFG and SFG, respectively. G-PDMS-7 was produced by mechanical mixing of RGO powder produced from SFG. The error bars are standard deviations.

The use of large-sized graphene sheets has several advantages in achieving higher electrical properties of composites. Firstly, individual graphene sheets from LFG shows superior mechanical and electrical properties as it possesses fewer defects during GO production. This is proved by Raman spectra that RGO made from LFG has a lower I_D/I_G ratio. This is also supported by the morphology of graphene sheets, where SEM images show that large-sized graphene sheets have fewer ripples and wrinkles compared to smaller graphene sheets, indicating that they are mechanically stronger and electrically more conductive. Secondly, since the use of large-sized graphene increases overlapped areas between graphene sheets, the contact resistance of inter-connected graphene network is reduced, and thereby boosting the overall electrical conductivity of the polymer composites. This is in agreement with Hicks' modelling study that graphene sheet area affects nano-composite resistivity more strongly than sheet density, and nano-composites composed of larger sheets are preferred for electrical conductivity applications [95]. Lastly, the large-sized graphene sheets diminish the total number of contact junctions on the path for carrying electrons compared to small-sized graphene sheets and therefore enhance the electrical conductivity.

4.4　Summary

In summary, we compared the electrical conductivity of G-PDMS from LFG and SFG, respectively. G-PDMS that originated from LFG exhibited significant improvements in both in-plane and through-plane electrical conductivity although the loadings of graphene in the G-PDMS composites from SFG are considerably higher. G-PDMS fabricated from LFG also showed enhanced through-plane electrical conductivity. This confirms that the size of graphene sheet plays a central role in determining the electrical conductivity of the composite. The greater size of the graphene sheet reduces the inter-sheet resistance when fabricated into a bulk

composite, and the SEM images and Raman spectra from RGO foams suggest that the large-sized of graphene sheets possess intrinsically better mechanical and electrical properties. This study demonstrates that graphene-polymer composites made of LFG can significantly reveal the excellent properties of graphene and increase the electrical conductivity of the polymer composite. The inter-connected graphene foam network provides more efficient paths for electron transfer inside the polymer than conventional graphene powder. Such composites synthesized by as-prepared methods can be applied to a variety of applications, especially EMI shielding. Metals and metallic composites have been employed as EMI shielding materials, but they suffer from severe oxidation and corrosion, and have poor chemical resistance, unfavourably high density, and are difficult to process. G-PDMS composites demonstrate numerous advantages including high chemical resistance and great processibility. In addition, light weight and flexibility of the polymer composites make themselves highly effective and practical for EMI shielding applications, especially in the areas of aircraft, spacecraft, automobiles, and next-generation portable and wearable electronic devices.

5. GNRs Incorporated Three-dimensional Foam Based Polymer Composites

5.1 Introduction

In the previous chapter, we have shown that polymer composite was prepared via infiltration of polymer into three-dimensional graphene foam, resulting in very low percolation threshold. Due to the nature of elastomer matrix, the composite exhibits both electrical conductivity and great flexibility, showing a great potential for wearable electronics. However, for polymer composites to be successfully employed in the stretchable and wearable electronics, their capability to retain high electrical conductivity under elongation is a necessity.

It was shown that the use of large-sized graphene sheets led to significantly enhanced electrical conductivity with an exceptionally low percolation threshold, implicating the dimensions of conductive fillers play an important role in determining the electrical property of final composite. Since it has been reported that the incorporation of high aspect ratio materials considerably boosts electrical conductivity at low loading of filers [5], [94], it appeared imperative to incorporate higher aspect ratio conductive fillers for further improvement and explore conductivity consistency as a function of elongation. In this chapter, we have utilized graphene nano-ribbons (GNRs) to construct three-dimensional foam and its variation in conductivity as a function of tensile strain was investigated in comparison to composites incorporated with graphene sheets of different size prepared from Chapter 4. Overall, polymer composites prepared with GNRs showed the greatest electrical conductivity and the highest consistency in electrical conductivity under a tensile strain up to 20%. This is because the GNRs were highly accumulated, creating macro-scale GNRs-accumulated sheets upon freeze casting, providing a

great contact area between the conducting sheets in their percolated network.

5.2   Materials and Methods

5.2.1   Materials

MWCNTs with a length of 10-30 μm and a diameter of 20-30 nm were purchased from Cheap-Tubes Inc. Hydrogen peroxide (30%), phosphoric acid, and sulphuric acid were obtained from Sigma Aldrich. Potassium Permanganate was acquired from EMD Chemicals. PDMS from Dow Cornings Inc was used in this study.

5.2.2   Preparation of graphene oxide nano-ribbons (GONRs) and reduced graphene oxide nano-ribbons (rGONRs) foams and GNRs-PDMS composite

The improved Hummer's method, proposed by James Tour and co-workers, was used to longitudinally unzip MWCNTs to synthesize graphene oxide nano-ribbons (GONRs) solution [36]. As-produced GONRs solution was used to produce three-dimensional GONRs foam by means of unidirectional freezing as described in Chapter 4. As-prepared GONRs foam was thermally reduced at 900°C to restore electrical conductivity. The reduced graphene oxide nano-ribbons (rGONRs) foam was then infiltrated with PDMS mixture to fabricate GNRs-PDMS composites. PDMS mixture was prepared by mixing Sylgard 184 silicone elastomer based with a curing agent with a 10:1 ratio. The electrical conductivity of GNRs-PDMS was measured and compared with G-PDMS made of SFG and LFG, which were prepared from Chapter 4. Hereafter, G-PDMS composites made with SFG and LFG is named SFG-PDMS and LFG-PDMS, respectively.

Table 5-1. Description of GNRs-PDMS, SFG-PDMS, and LFG-PDMS composites used in this study.

Composites	Raw material	GO (or GONRs) conc. (mg/mL)	Loading (wt%)
GNRs-PDMS	MWCNTs (l=10-30 μm, d=20-30 nm)	23	1.2
LFG-PDMS	Large-sized graphite (d>100 μm)	11.5	0.5
SFG-PDMS	Small-sized graphite (d=2-15 μm)	25	1.9

5.2.3   Characterizations

The morphology of GONRs and rGONRs and dispersion of fillers within the PDMS matrix was examined by means of SEM (Zeiss LEO 1550). The individual MWCNTs and the unzipped GONRs were observed by TEM (JEOL 2010F) for verification of lengthwise unzipping process. The variation of a crystal structure due to oxidation and reduction process was explored by means of XRD (Rigaku Miniflex 600). The analysis of the defects and disorders of graphene sheets and GNRs was carried out by means of Raman spectroscopy (Bruker Senterra, 532 nm).

5.2.4   Electrical conductivity measurement with elongation

The infiltrated composites were sliced into small slabs (1.4 x 0.7 x 0.1 cm) and their in-plane conductivity was measured as a function elongation by means of 4 point probe method. The 4 point probe testing cell capable of measuring the electrical conductivity under strain was designed and assembled in our lab and illustrated in Fig. 5-1. First, the sliced samples are mounted on the clamps of the house-modified stretching device (Fig. 5-1a). The specimen is stretched as shown in Fig. 5-1b and the elongated specimen is fixed. The elongated and fixed specimen mounted on the stretching device is then placed into the house-built 4 point probe

testing cell designed to fit the house-modified stretching device to measure electrical conductivity under elongation (Fig. 5-1c and d).
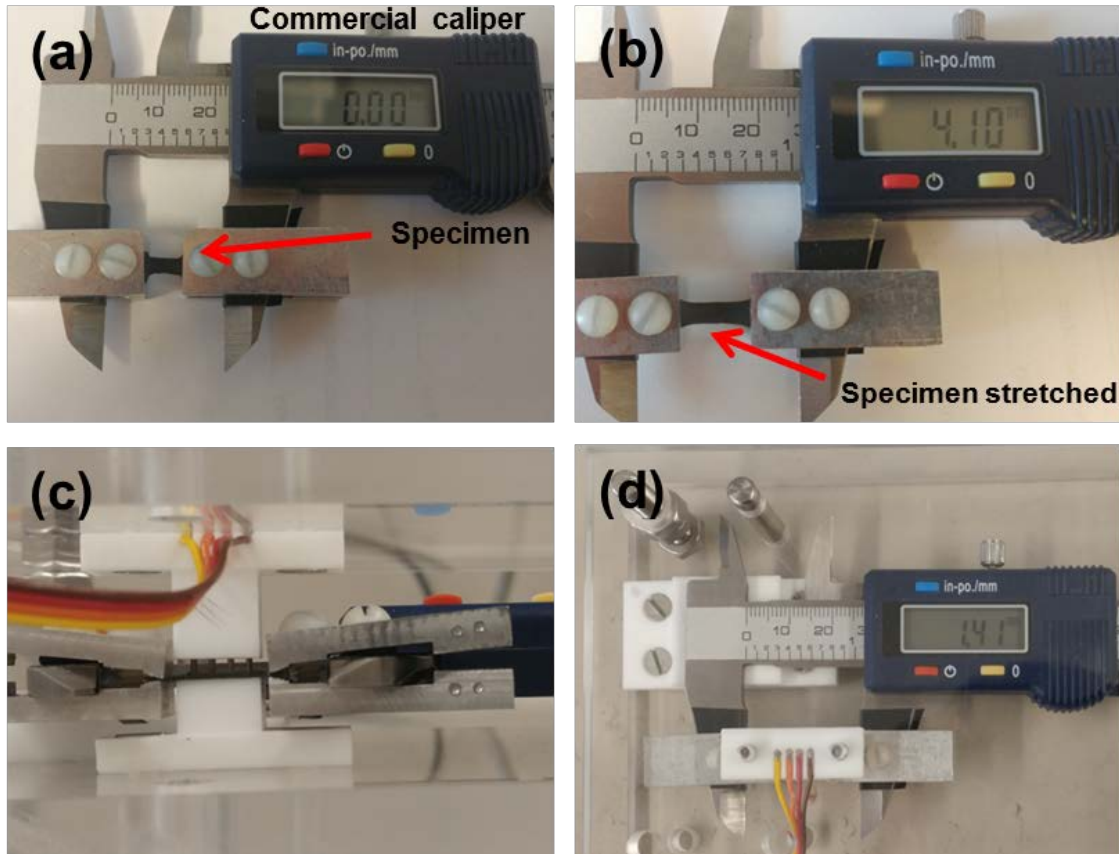
Figure 5-1. Description of measuring electrical conductivity with elongation. The specimen is clamped in the house-modified stretching device (a). The specimen is elongated and fixed (b). The stretched sample is placed in the house-built 4 point probe testing cell and the conductivity under elongation is measured (c and d).

5.3   Results and discussion

5.3.1   Material characterization
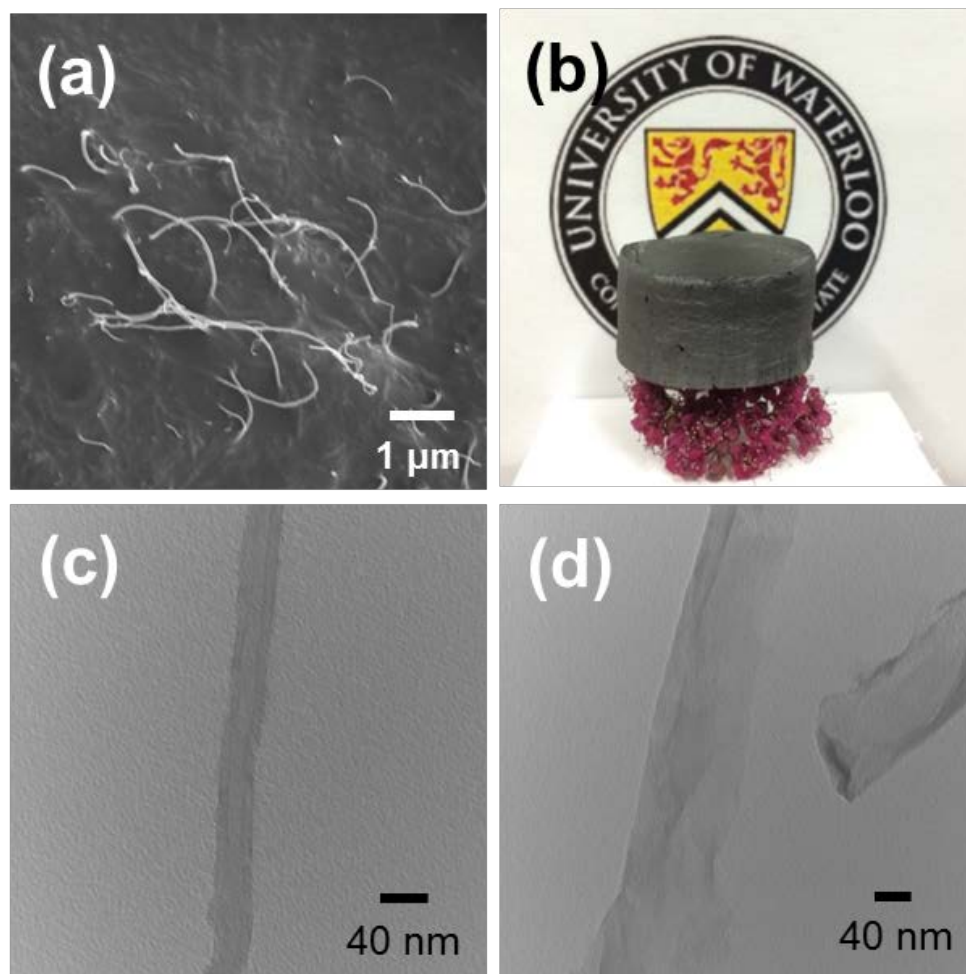
Figure 5-2. (a) SEM images of MWCNTs. (b) Photo image of rGONRs foam. TEM images of (c) MWCNTs and (d) lengthwise unzipped GONRs.

The SEM image of MWCNTs is shown in Fig. 5-2a, and the low density and light weight of rGONRs are demonstrated in Fig. 5-2b. The TEM images of MWCNTs (Fig. 5-2c) and GONRs (Fig. 5-2d) clearly show that the MWCNTs are longitudinally unzipped, and thin and long strips of GNRs with a high aspect ratio of length-to-width are successfully synthesized. The unzipped GONRs are estimated to have a length of 10-30 μm and a width of 60-90 nm, approximately,

which has a very high length-to-width aspect ratio (100-500).

The structural variation induced by the evolution of MWCNTs are investigated by means of XRD and Raman spectroscopy and described in Fig. 5-3 with extracted parameters from each analysis shown in Table 5-2. The XRD data indicate that MWCNTs experienced a similar structural evolution to graphite as was shown in chapter 4.3.1. The 2 theta peak for MWCNTs appeared at 25.94 indicating an interlayer distance of 3.43 Å, which is consistent with other layered graphitic structures. Upon oxidation reaction by the improved Hummer's method, the 2 theta peak shifted to 9.62 as shown from GONRs. This indicates the formation of functional groups intercalated between the multi-layers of MWCNTs. Upon thermal reduction, the 2 theta peak appeared at 26.18, implicating that the functional groups introduced from the oxidation reaction were removed.
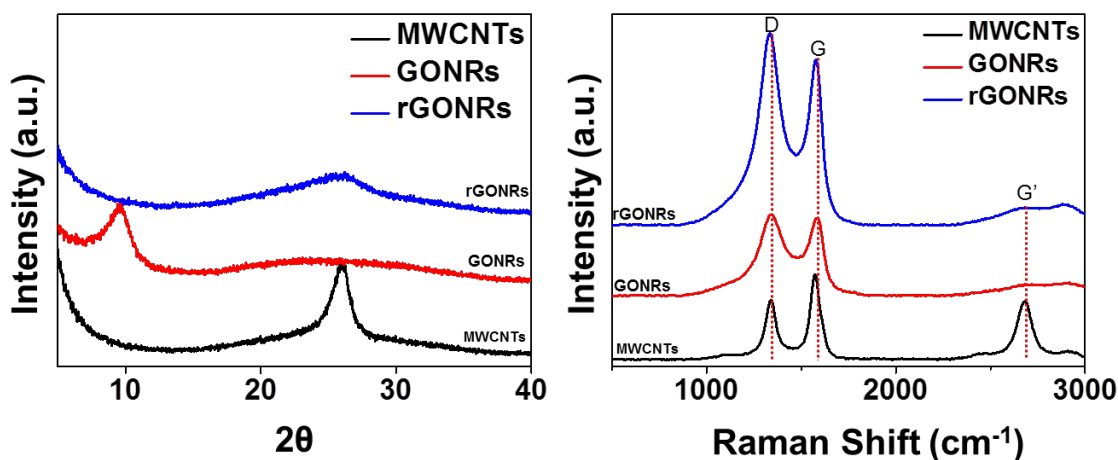
Figure 5-3. (a) XRD and (b) Raman spectra of MWCNTs, GONRs, and rGONRs.

Raman spectroscopy is widely employed to characterize the structural variation of carbon materials caused by oxidation or reduction. MWCNTs show three characteristics peaks of D, G, and G' in Fig. 5-3b. When oxidized and converted to GONRs, the D peak intensified and G' peak

disappeared. This indicates that the edge structures acting as defects were formed by unzipping process [96] and the size of in-plane sp^2 domains was reduced due to extensive oxidation [97]. Upon thermal reduction, the intensity of D peak further increased, enhancing the I_D/I_G ratio from 1.04 to 1.16 (Table 5-2). This has been previously reported and understood that the reduction process increases the number of small domains of sp^2 carbons, but not their overall sp^2 domain size on the plane [98]. It also should be noted that I_D/I_G ratio and L_a of rGONRs are similar to that of LFG calculated from Chapter 4.3.2. This indicates that the intrinsic electrical conductivity of rGONRs foams might be similar to that of reduced graphene foams made of LFG.

Table 5-2. The parameters extracted from XRD and Raman spectra, respectively.

Materials	XRD					Raman	
	2θ degree	Interlayer Distance ($\mathring{A}$)	FWHM (radian)	L_c ($\mathring{A}$)	Number of layers	I_D/I_G	L_a (nm)
MWCNTs	25.94	3.43	1.42	57.48	16.75	0.72	26.7
GONRs	9.62	9.18	2.76	28.91	3.15	1.04	18.5
rGONRs	26.18	3.40	15.77	5.19	1.53	1.16	16.6

5.3.2 Morphology of rGONRs foam and GNRs-PDMS composites
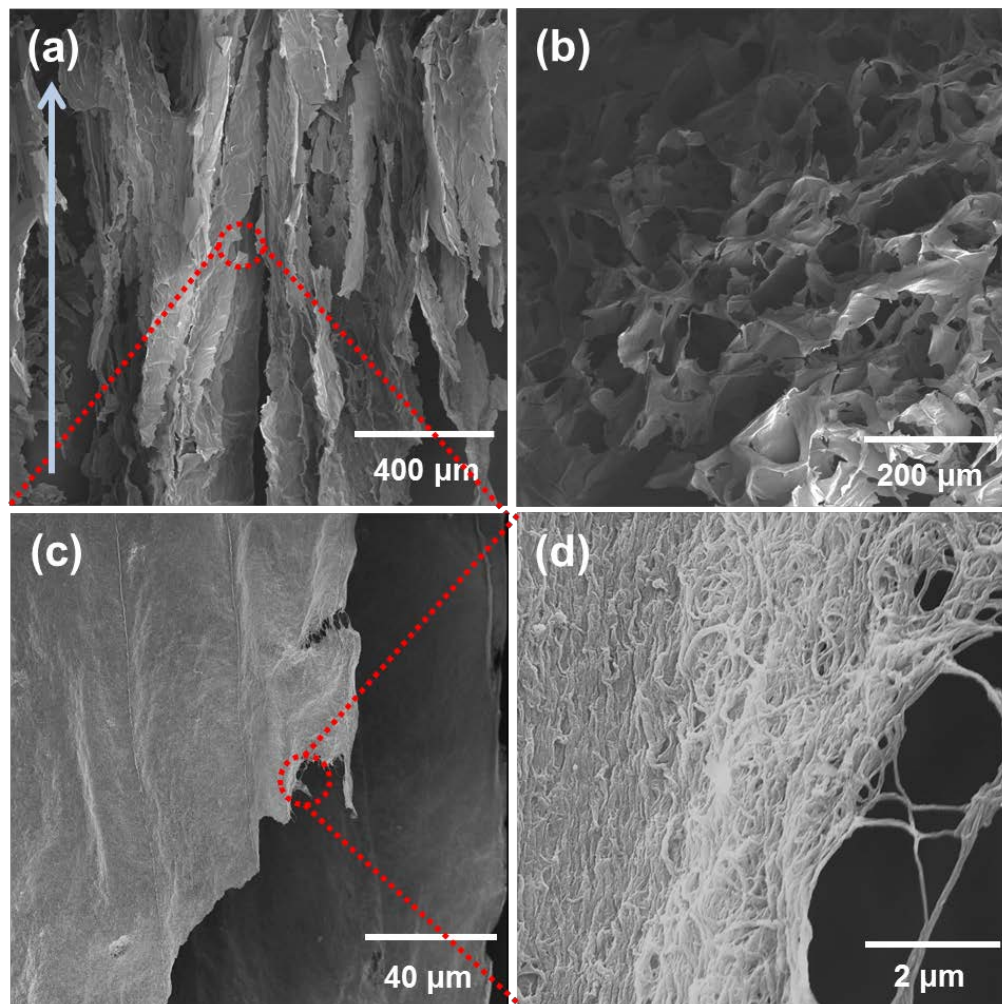
Figure 5-4. SEM images of (a,c,d) lateral and (b) cross-sectional view of rGONRs foams. It is clearly seen that GNRs are highly entangled and accumulated to create extremely large-sized sheets. The arrow indicates the direction of freezing.

The morphology of rGONRs foam has been explored by means of SEM and described in Fig. 5-4. The lateral view of the foam is shown in Fig. 5-4a, c, and d with increasing magnitude while the cross-sectional view is available in Fig. 5-4b. It was observed that the individual GNRs strips are highly accumulated and concentrated (Fig. 5-4d), constructing ordered micro-channelled sheets, called GNRs-accumulated sheets hereafter, with a high aspect ratio of length to width

(Fig. 5-4a). It is clearly evident from the lateral view that large-sized GNRs-accumulated sheets are well oriented along with the direction of freezing. The orientation of large GNRs-accumulated sheets induces the macroporous honeycomb-like structure as can be seen from the cross-sectional view (Fig. 5-4b). It appears that this formation is due to the growth of ice crystals that initiated from the bottom of the metal substrate during freezing [45]. It has been reported that when a liquid suspension of nano-particles is frozen, phase separation occurs, leading to the rejection of nano-particles from the moving solidifying front of the ice crystals. These rejected nano-particles are accumulated and piled up between the ice crystals. As the ice crystals grow, the individual GNRs are pushed toward each other and entrapped [99]. Upon further growth of crystals, the individual GNRs strips are more densely concentrated, creating large-sized GNRs-accumulated sheets that are highly aligned with the direction of ice crystal growth as schematically illustrated in Fig. 5-5. This processing technique for producing aligned macroporous materials by freezing a liquid suspension followed by sublimation of the solidified phase from the solid to gas phase under low pressure is often referred to as freezing casting [100].
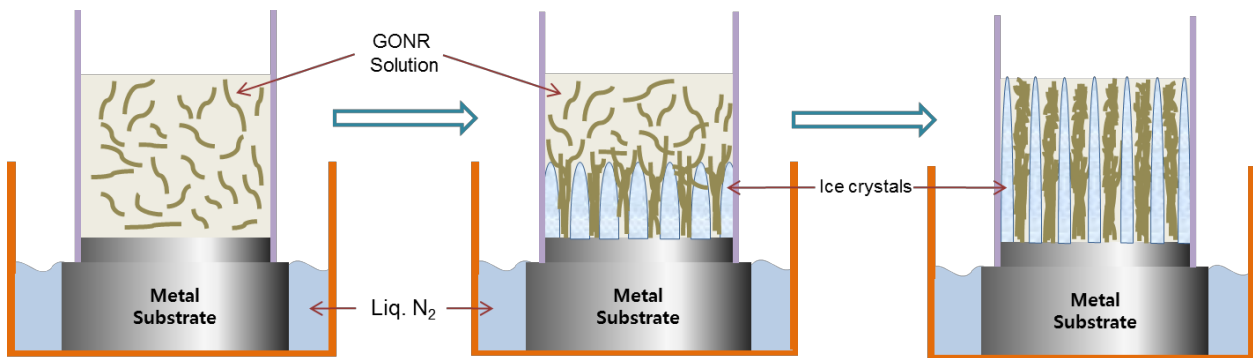
Figure 5-5. Schematic illustration of forming large-sized GNRs-accumulated sheets upon unidirectional freezing.

The freeze casting and pores morphology, in general, are influenced by several different factors, such as crystallization behaviour of solvents and interaction of all species in solution. Firstly,

crystallization behaviour of solvents is greatly dependent upon freezing condition, which will play a central role in determining the size of pores. For example, freezing temperature governs the relative dominance of ice nucleation versus crystal growth. At sufficiently low temperature, nucleation rate is higher than crystal growth, thus a large number of small ice crystals will be formed. If the solution is exposed to relatively higher freezing temperature, the ice crystal growth will be favoured, leading to the formation of less number of ice crystals with greater size. Another important parameter is the nature of the solvent. The main appearance of the structure will be largely determined by the crystallographic properties of solvents. For instance, the use of water as a solvent will give lamellar structure while the use of camphene or prismatic with tert-butyl alcohol will result in dendritic appearance [100]. Secondly, the interaction between the species and their chemistry is also very crucial. In our system with oxidized graphene nano-ribbons dispersed in water, the oxygen-containing functionalities attached on the basal plane are one of the key parameters. These functional groups are known to be negatively charged, creating considerable electrostatic repulsion between sheets [101]. The functional groups, on one hand, are essential to exfoliate stacked layers and achieve a good dispersion of graphene sheets in water. On the other hand, this could hinder constructing highly inter-connected network during the freezing process. Qui and co-workers reported that partial reduction of graphene oxide was advantageous to produce their cork-like graphene monoliths due to reduced repelling force [45]. When entrapped and concentrated between the growing ice crystals, the interaction between sheets with reduced repelling force will help create a continuous network. Moreover, the π-π attraction between the sheets due to partial restoration of π-conjugation during the reduction can enhance inter-connection between sheets once they are accumulated and stacked together.

From the SEM images of a lateral view of GNRs-PDMS composites (Fig. 5-6), it can be

72

observed that GNRs-accumulated sheets are dispersed with an orientation along with the direction of freezing. The cross-sectional view of SEM images demonstrated that the GNRs-accumulated sheets are well-dispersed, and the pores between the GNRs-accumulated sheets are filled with PDMS. These images confirmed again that the fabrication via infiltration of graphene foam is an effective way of engineering polymer composites that does not compromise the original network of filler, achieving a high degree of dispersion with excellent electrical conductivity at low loadings of fillers within the composite.
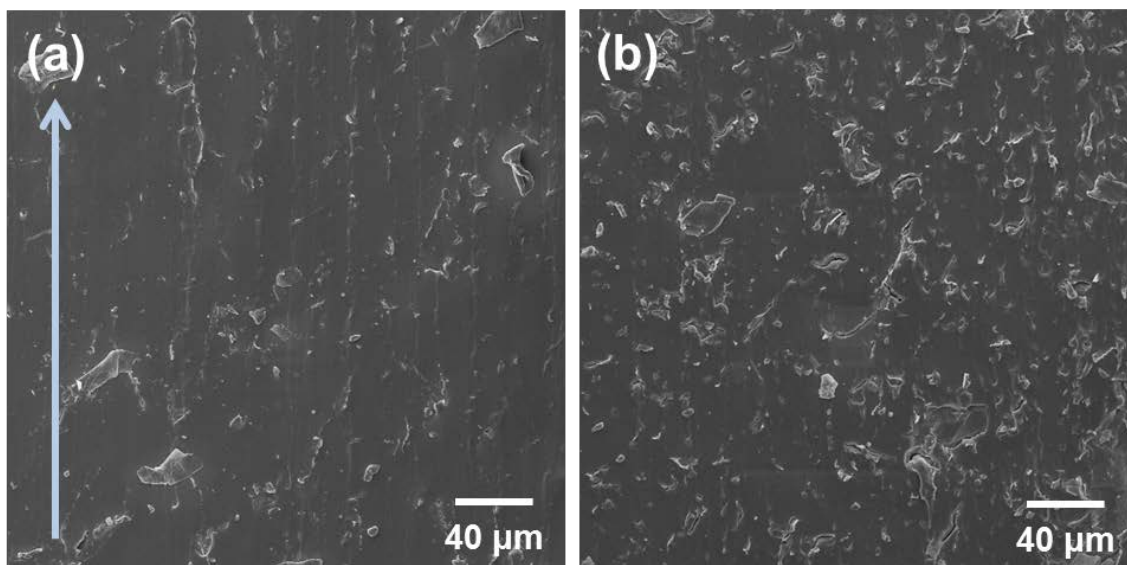
Figure 5-6. SEM images of (a) lateral and (b) cross-sectional view of GNRs-PDMS composites. The arrow indicates the direction of freezing.

5.3.3 Electrical conductivity of GNRs-PDMS composites
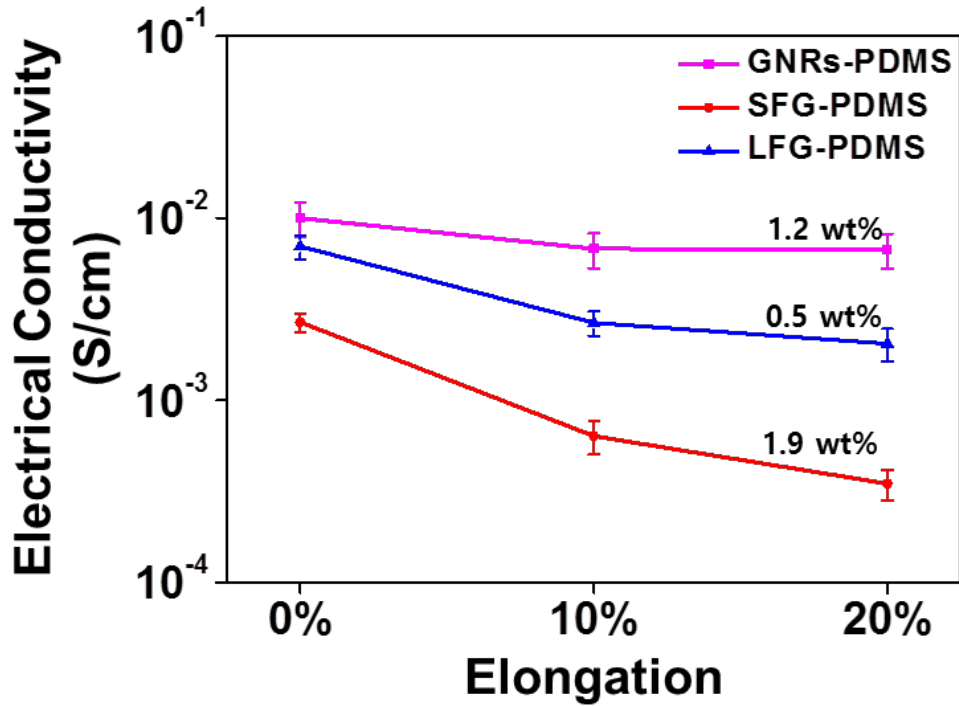
Figure 5-7. The variation of in-plane electrical conductivity as a function of elongation of specimen. The error bars are standard deviations.

The variation of in-plane electrical conductivity with elongation was measured and described in Fig. 5-7. All the three composites experienced a conductivity drop as the specimen is stretched. At 0% elongation, GNRs-PDMS exhibited the highest electrical conductivity of 10×10^{-3} S/cm, and LFG-PDMS and SFG-PDMS showed conductivity of 7.0×10^{-3} S/cm and 2.7×10^{-3} S/cm, respectively. By elongating each specimen by 10%, a significant conductivity drop occurred, but each specimen exhibit various degree of decrease depending on the size and connectivity of fillers incorporated within the composite. The least reduction in conductivity was observed for GNRs-PDMS and the greatest decrease was detected for SFG-PDMS. As described in Table 5-3, GNRs-PDMS showed 32% of conductivity drop upon 10% elongation while 62% of

conductivity drop was measured for LFG-PDMS. The most dramatic decrease (76%) was found

for SFG-PDMS composite. Upon further elongation up to 20%, each composite experienced an

additional drop in conductivity, but the magnitude of the drop again varied with the size and

connectivity of filler within the composite. GNRs-PDMS showed consistent conductivity when it

was further elongated from 10 to 20%, and the electrical conductivity only slightly decreased by

1%. This is a considerably less reduction in comparison to other composites. The electrical

conductivity of LFG-PDMS showed an additional drop of 9%, and 11% drop in conductivity was

detected for SFG-PDMS composite.

Table 5-3. The in-plane electrical conductivity and the percentage drop of conductivity with respect to elongation.

Elongation (%)	GNRs-PDMS (10^{-3} S/cm)	Conductivity drop (%)	LFG-PDMS (10^{-3} S/cm)	Conductivity drop (%)	SFG-PDMS (10^{-3} S/cm)	Conductivity drop (%)
0%	10		7.0		2.7	
10%	6.8	32	2.7	62	0.64	76
20%	6.7	33	2.1	71	0.35	87

The reduction in electrical conductivity upon elongation is presumably considered due to a

decrease in the contact area and loss of contact junctions between conducting fillers within the

composite [83]. When a large contact area is established, the conducting sheets within the

percolated network can slide past one another without losing their contact junctions. The size of

contact area will be proportional to the dimensions and aspect ratio of initial building materials.

The greatest consistency of electrical conductivity against a tensile strain from GNRs-PDMS

implicates that there exist large contact areas overlapped between GNRs-accumulated sheets.

This is clearly observed from Fig. 5-4 that GNRs-PDMS possesses the large overlapped contact

area with a number of contact junctions due to the large-sized GNRs-accumulated sheets. GNRs-accumulated sheets are densely packed in rGONRs foams and we can see these sheets share substantial contact areas in between. On the contrary, we can see that from Fig. 4-3 there exists a greater porous area between the sheets and less contact area is available from RGO foams made of LFG and SFG, respectively. As the size of graphene sheet decreases, the contact area between fillers will be significantly reduced, leading to a dramatic drop in electrical conductivity upon stretching. A further stretch will eventually destroy the percolation network. However, the percolation network will be retained up to a greater tensile strain when large-sized conducting sheets are densely packed and overlapped within the composite.

5.4   Summary

The thin and long strips of GNRs were successfully synthesized by unzipping MWCNTs by the improved Hummer's method suggested by James Tour and co-workers. MWCNTs were oxidized and transformed into GONRs which were dispersed in water solution. The GONRs solutions were directly used to create three-dimensional GONRs foams by means of freeze casting. SEM images revealed that GNRs were entrapped between the growing ice crystals and highly accumulated to form an extremely large scale sheets (GNRs-accumulated sheets) in GONRs foams. As-produced GONRs foams were thermally reduced to restore electrical conductivity and subsequently infiltrated with PDMS to fabricate a stretchable polymer composite. As-fabricated GNRs-PDMS composites were slices into small slabs, and their electrical conductivity was measured while being uniaxially stretched. When their electrical conductivity as a function of tensile strain was compared with the previous composites consisting of LFG and SFG, a significantly improved consistency in electrical conductivity was observed. GNRs-PDMS only experienced 33% conductivity drop at 20% stain while LFG-PDMS and SFG-PDMS exhibited

71% and 87% conductivity drop, respectively. This could be due to large contact area available between GNRs-accumulated sheets. The percolated network is well maintained due to this large contact area, and the contact junctions are not disconnected under a high stain. The consistency of electrical conductivity under elongation is a great advantage for producing flexible electronics, and therefore the use of GNRs for fabricating polymer composite has a promising potential for numerous applications including smart clothing, flexible display, and electronic textiles.

6. Ultra-large Sized Graphene nano-platelets (GnPs) Incorporated Polypropylene (PP)/GnPs Composites Engineered by Melt Compounding and its Thermal, Mechanical, and Electrical Properties

This chapter is reprinted in adapted form from the article below with permission from Elsevier.

Jun YS, Um JG, Jiang G, Lui G, Yu A. "Ultra-large sized graphene nano-platelets (GnPs) incorporated polypropylene(PP)/GnPs composites engineered by melt compounding and its thermal, mechanical, and electrical properties", *Composite Part B: Engineering*, 2018;133:218-225.

6.1 Introduction

In Chapter 4 and Chapter 5, polymer composites were fabricated via infiltration of free-standing graphene foam. In this chapter, we have employed a different polymer processing technique, which is twin screw extrusion followed by injection moulding to fabricate conductive thermoplastic composites. In this technique, GnPs are incorporated into an engineering polymer, PP in our study.

In the field of polymer composites produced by compounding, nowadays particular interest has been given to GnPs and their composites with PP [102]–[111]. PP is one of the most widely used polyolefins in a variety of applications due to its numerous advantages, such as great physical and mechanical properties, ease of processing, low cost, and recyclability [112]–[115]. Moreover, significant weight reduction can be achieved when PP is integrated into products due to its low

density. PP also exhibits great thermal and chemical resistance and excellent moisture barrier [27], [116]. GnPs are graphite nano-crystals in the form of platelets consisting of multiple layers of graphene linked by van der Waal's forces. Recently, GnPs have received considerable attention due to its numerous advantages including exceptional thermal, mechanical, and electrical properties, and low cost [31], [116]–[121]. Therefore, the PP composites incorporated with GnPs have promising potentials in a number of applications including electronics, aerospace, automobile, military to green technology [27], [122].

Several researchers have explored the properties and characteristics of PP/GnPs composites [123]–[126]. Kalaitzidou et al. compared the performance of GnPs-reinforced composites with other composites incorporated with conventional fillers including carbon black, carbon fibres, and clays [123]. Approximately 9 GPa of flexural modulus was obtained for the composites blended with 20 vol % of GnPs, whereas less than 7 GPa of flexural moduli were gained for the composites incorporated with other conventional fillers. In addition, the mechanical properties were further improved with a smaller size of GnPs (with a diameter of 1 μm). However, large-sized particles with high dispersibility are preferred for increasing electrical conductivity since a significantly reduced percolation threshold can be attained as was shown in Chapter 4. The use of large-sized fillers with a high aspect ratio expedites the formation of a percolation network within the polymer matrix when compared to the small-sized fillers with a low aspect ratio at the same loading. This is very crucial because when lower amounts of nano-particles are used, composites with desired properties can be produced without compromising the properties of the polymer matrix. Using a reduced amount of filler can also avoid possible mechanical failure. Nonetheless, no studies have been conducted on the nano-composites that are comprised of large-sized GnPs with a diameter greater than 100 μm and a high aspect ratio.

The objective of this chapter is to investigate the thermal, mechanical, and electrical properties of PP/GnPs composites when very large-sized GnPs are employed as fillers via melt compounding. The thermal behaviour and crystallinity were explored by means of DSC and XRD to investigate whether the incorporation of GnPs can initiate any crystalline change to the PP matrix. Any change in the crystallinity can further alter the properties of the composite in addition to the improvements made by the fillers. High electrical conductivity and low percolation thresholds were obtained by incorporating large-sized GnPs in the PP matrix. An in-plane conductivity of 1.7×10^{-2} S·cm^{-1} was achieved with a percolation threshold of 2.99 vol%, and a through-plane conductivity of 3.3×10^{-3} S·cm^{-1} was obtained with a percolation threshold of 2.98 vol%. Nonetheless, the use of large-sized GnPs was less satisfactory for improving mechanical properties due to their high probabilities of being distorted during compounding process, resulting in a reduction in aspect ratio and poor interfacial bonding and adhesion between fillers and polymer matrix.

6.2   Materials and Methods

6.2.1   Materials

HM20/70P PP powder was purchased from Goonvean Fibres Ltd. and used as the matrix material. This powder has a particle size range of 0.055 to 0.077 mm and a density of 0.90-0.91g·cm^{-3} [127] (Fig. 6-1). The melt flow index was determined using Dynisco Polymer Test Systems (D4002) at 230°C and 2.16 kg in accordance with ASTM D1238 and was 19.4 g·10min^{-1}[128]. Grade H GnPs (~0.150 mm in diameter) were obtained from XG science and used as fillers (Fig. 6-1). According to the technical data sheet provided by XG Science the grade H GnPs have a density of 2.2 g·cm^{-3}, and an average thickness of ~20 nm with a typical surface

area of 50 to 80 $m^2 \cdot g^{-1}$ [42].
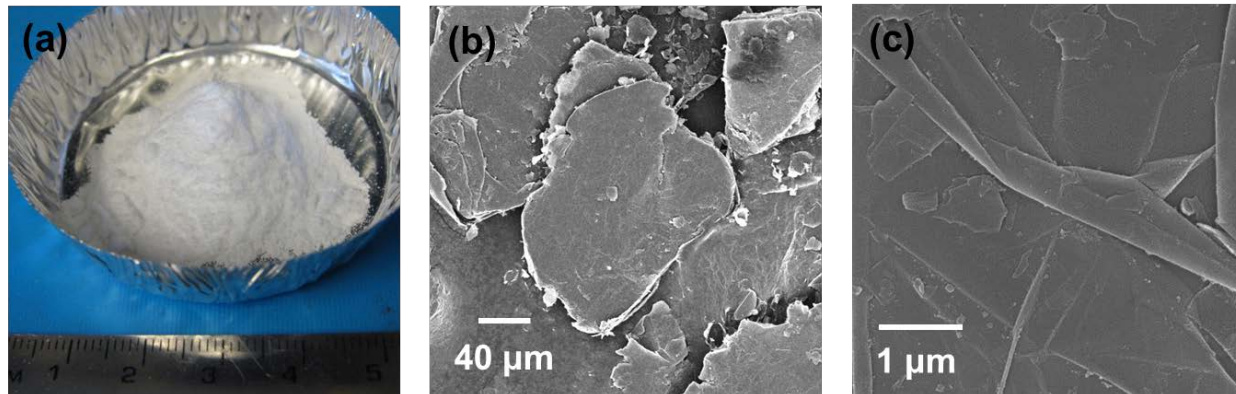
Figure 6-1. (a) Optical images of HM20/70 PP powder and SEM images of Grade H GnPs used in this study at (b) low and (c) high magnifications.

6.2.2 Composites preparation

PP composites with various GnPs contents (0.0, 1.6, 3.2, 3.8, 4.4, 5.5, and 9.3 vol%) were prepared by melt extrusion and injection moulding. The composites were prepared by weight basis and converted to a volumetric fraction. For improved dispersion of fillers within the polymer matrix, PP and GnPs were pre-mixed prior to extrusion. PP and GnPs were dispersed in ethanol and mechanically mixed, then dried in a vacuum oven at 60°C for 24 hr. The pre-mixed mixtures were then added into the counter-rotating conical micro compounder (Wuhan Ruiming Plastics Machinery Co., Ltd, SJZS-07A) with a screw speed of 24 rpm. The temperature setting from the hopper to the die was 165/170/175/185°C. The mixture was circulated and mixed in the extruder for 5 min and extruded. The extrudates were then pelletized by pelletizing machine (SQS-120) and dried again at 60°C for 12h prior to injection moulding to prevent moisture inclusion. Finally, the pelletized extrudates were fed into an injection moulding machine (SZS-20). The temperature for hopper and mould were set up 220°C and 65°C, respectively. The pressure employed for injection and moulding were ~0.7 MPa and ~0.3 MPa, respectively.

81

6.2.3 Characterizations

6.2.3.1 Thermal property measurements

TGA was carried out to investigate the residual amount of GnPs by a thermal analyzer (TA Q500, USA). The specimens were scanned from 20 to 800°C at a heating rate of 10°C·min^{-1} under a nitrogen atmosphere. To study the crystallization of the composites, DSC was performed with a thermal analyzer (TA Q2000, USA) and scanned from -30 to 250°C under a nitrogen atmosphere with a heating and cooling rate of 10 °C·min^{-1}. The samples were kept at 250°C for 3 minutes to remove the thermal history. The samples for both TGA and DSC weighed ~5 mg.

6.2.3.2 Structural and morphological analyses

XRD characterization of the composites was carried out on a Rigaku Miniflex 600, using the Cu-Kα radiation (λ=1.54184 Å). The morphology of the specimens was characterized by SEM (Zeiss Leo 1550).

6.2.3.3 Mechanical property measurements

Flexural strength was determined by the three-point bending method using an Instron 4465, according to ASTM D790-03 (Cell 5kN) with a span length of 45 mm [129]. A flexural bar with dimensions of 80 mm x 10 mm x 4 mm was prepared and tested at ambient conditions with a cross-head speed of 10 mm·min^{-1}. Five samples were prepared and tested, and the average value and standard deviation were obtained. The calculation of the flexural strength and modulus is provided in the supplementary information.

The tensile strength of the composites was measured on a universal testing machine (4.4 kN, eXpert 7603, ADMET, USA) at ambient conditions with a cross-head speed of 5 mm·min^{-1}. Five

samples with a length of 75 mm, a thickness of 2 mm, and a parallel length of 30 mm were prepared and tested according to ASTM D638-14 [130].

6.2.3.4 Electrical conductivity measurements

Electrical conductivity was measured on the flexural specimens by a four-point probe method. Specimens were cut into dimensions of 15 mm x 10 mm x 3.5 mm to measure the in-plane electrical conductivity (σ_I). The rich skin layer of the polymer was removed to accurately measure the electrical conductivity. The in-plane and through-plane electrical conductivities of G-PDMS composites were measured in accordance with the methodology introduced in Section 3.3.

6.3   Results and Discussion

6.3.1   Thermal properties of PP/GnPs composites

The thermal stability parameters were extracted from TGA (Fig. 7-2) and differential thermo-gravimetric (DTG) curves (Fig. 7-3) and described in Table 6-1. The amount of GnPs in each composite was also confirmed and provided in Table 6-1. It is shown that T_{max} is gradually improved with the increasing amount of GnPs whereas the inferior $T_{5\%}$ was observed with GnPs contents up to 4.4 vol%. In general, the improved thermal stability is achieved since GnPs serve as a mass transport barrier which obstructs the transport of polymer degradation products to the surface [131]. However, the reduced thermal stability at the initial stages of decomposition is reported in several studies when carbonaceous materials are used as fillers [132]–[135]. The inferior $T_{5\%}$ in our study could be due to the superior thermal conductivity of GnPs [133], [134]. For the neat polymer, the thermal decomposition will begin at the surface of the material. If the

composite is filled with highly thermally conductive fillers, the heat will be efficiently transferred deep into the composites, especially with high aspect ratio fillers. It will help heat distribution across the composite, and the thermal degradation can also be initiated both at the surface and internal areas of the composites simultaneously upon exposure to very high temperatures. This will lead to negative influences on the thermal stability of composites and can accelerate the thermal decomposition and cause $T_{5\%}$ reduced. However, GnPs also have significant positive influences on improving thermal stability by serving as barriers to volatile gases and by scavenging free-radicals that trigger thermal decomposition [131], [136]. As the thermal decomposition continues, the produced volatile gases (decomposition products) can be trapped within the composites due to the barrier effect of GnPs. Also, the free radicals will be removed by GnPs as the contents of GnPs increase and hence T_{max} can be improved. Therefore, there exist both negative and positive effects of GnPs and they are competing against each other. As the loading of GnPs increases, the barrier effect and free radical removals prevail, and the improved thermal stability can be achieved.

Table 6-1. Thermal stability parameters and residual amounts (%) collected from TGA. The weight fraction (wt%) is also converted to volume fraction (vol%).

Loading of GnPs (wt%)	0.0	3.0	7.5	10.0	20.0
Residual amount (wt%)	0.0	3.1	6.9	9.5	18.9
$T_{5\%}$ (°C)	393	350	373	372	402
T_{max} (°C)	447	445	452	450	457
Loading of GnPs (vol%)	0.0	1.3	3.2	4.4	9.3
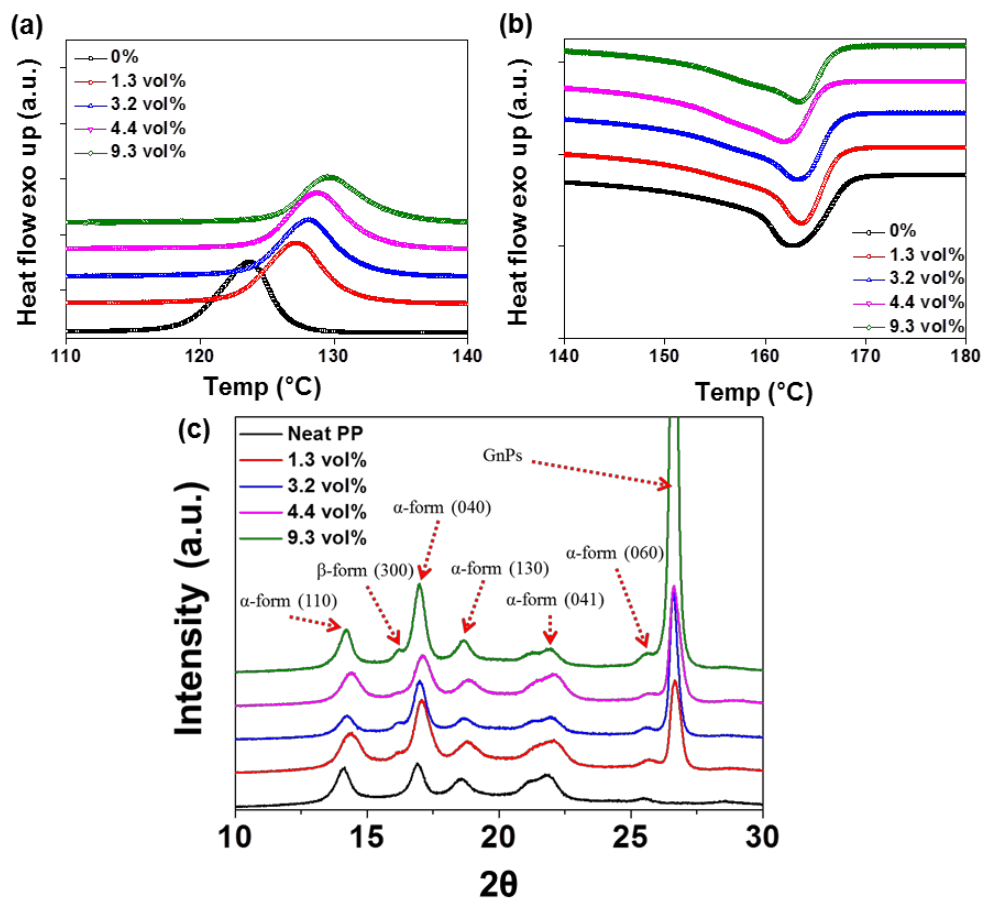
Figure 6-2. **(a) Crystallization thermograms and (b) melting thermograms of PP/GnPs composites. (c) XRD curves of neat PP and PP/GnPs composites.**

Since the crystallinity of polymers plays a central role in determining the number of properties, it was essential to investigate the variation of crystallization behaviour of polymers upon addition of GnPs. The crystallization and second melting curves of PP/GnPs composites are described in Fig. 6-2 with extracted parameters illustrated in Table 6-2. It is clearly shown that the crystallization temperature (T_c) increased with increasing amounts of fillers, indicating that crystallization of polymer matrix was accelerated in the presence of GnPs. An increase in T_c is equivalent to a decrease in the degree of super-cooling ($\Delta T = T_m - T_c$). The degree of super-cooling is proportional to the free energy of melting which is associated with the driving force for

nucleation [137]. Therefore, reduction in the degree of super-cooling indicates that crystallization was achieved at a lower driving force, suggesting that the crystallization was facilitated with GnPs. This is due to a role of GnPs as seeds for heterogeneous nucleation. Many researchers have revealed that several types of fillers including MWCNTs, clay, and GnPs can be nucleation agents that introduce other forms of crystals, often increasing crystallinity [138]–[140].

Table 6-2. Parameters extracted from DSC thermograms of PP/GnPs composites.

Contents of GnPs (vol%)	T_c (°C)	T_m (°C)	ΔT	ΔH_{crys} (Jg^{-1})	ΔH_{melt} (Jg^{-1})	X_c
0.0	123.5	162.7	39.2	171.5	124.8	60
1.3	127.1	163.6	36.5	166.6	122.5	60
3.2	127.9	163.2	35.3	162.7	117.3	60
4.4	128.6	162.0	33.4	150.5	113.1	60
9.3	129.6	163.3	33.7	133.5	100.6	59

While all the crystallization thermograms were characterized by uni-modal curves, the second melting thermograms slightly exhibit a bimodal pattern, as shown in Fig. 6-2b, especially for the composites with GnPs contents greater than 3.2 vol%. Since these bimodal curves can be indicative of the existence of crystals other than α-form, a further qualitative analysis for determining crystallinity was explored by means of XRD. Fig. 6-2c presents the XRD peaks for neat PP and PP/GnPs composites. The neat PP peaks show a typical pattern of α-form crystals for PP, and the four peaks at 14.08, 16.95, 18.5, and 21.85 correspond to (110), (040), (130), and (041) planes of α-form crystals, respectively. The peaks representative for any other form of crystals does not appear for neat PP. As the contents of GnPs increased, a very small peak

responsible for β-form crystals appears at 2θ angles of 16 which accounts for (300) planes [138]. However, it is evident that α-form crystal peaks dominate in the crystal structure. DSC analysis found that the second modes in melting thermograms were not highly distinct, and the crystallization thermograms clearly exhibited a single peak. Therefore, it is conceivable that the formation of β-form crystals could be induced, but the content of the β-form crystals is minimal. The relative contents of β-form crystals are calculated and provided in the appendix (Table A-2). Overall, the introduction of GnPs did not induce significant change to the crystallinity of the PP polymer matrix. The melting thermograms obtained with additional ramping rates of 2°C·min^{-1} and 20°C·min^{-1} were provided in Fig. A-4.

Although it has been shown that the incorporation of GnPs may boost the crystallization of polymer matrix and induce the formation of different types of crystals, the degree of crystallinity (X_c) did not vary significantly (Table 6-2). This implicates that the incorporation of GnPs did not induce significant crystallinity change that could influence the mechanical property of the polymer matrix, and thus any variation in mechanical properties is solely due to the reinforcing effect of fillers.

6.3.2   Mechanical properties of PP/GnPs composites

Flexural strength, modulus of elasticity, tensile strength and Young's modulus were determined as a function of GnPs loadings and described in Fig. 6-3, with extracted parameters detailed in Table 6-3. The modulus of elasticity was gradually increased as GnPs' loading increased. However, the flexural strength steadily decreased upon addition of GnPs in a polymer matrix. The decrease in flexural strength can be associated with several factors, such as the low degree of filler dispersion and the inferior surface interaction between filler and polymer matrix, which

87

leads to failure in effective load transfer [141], [142].
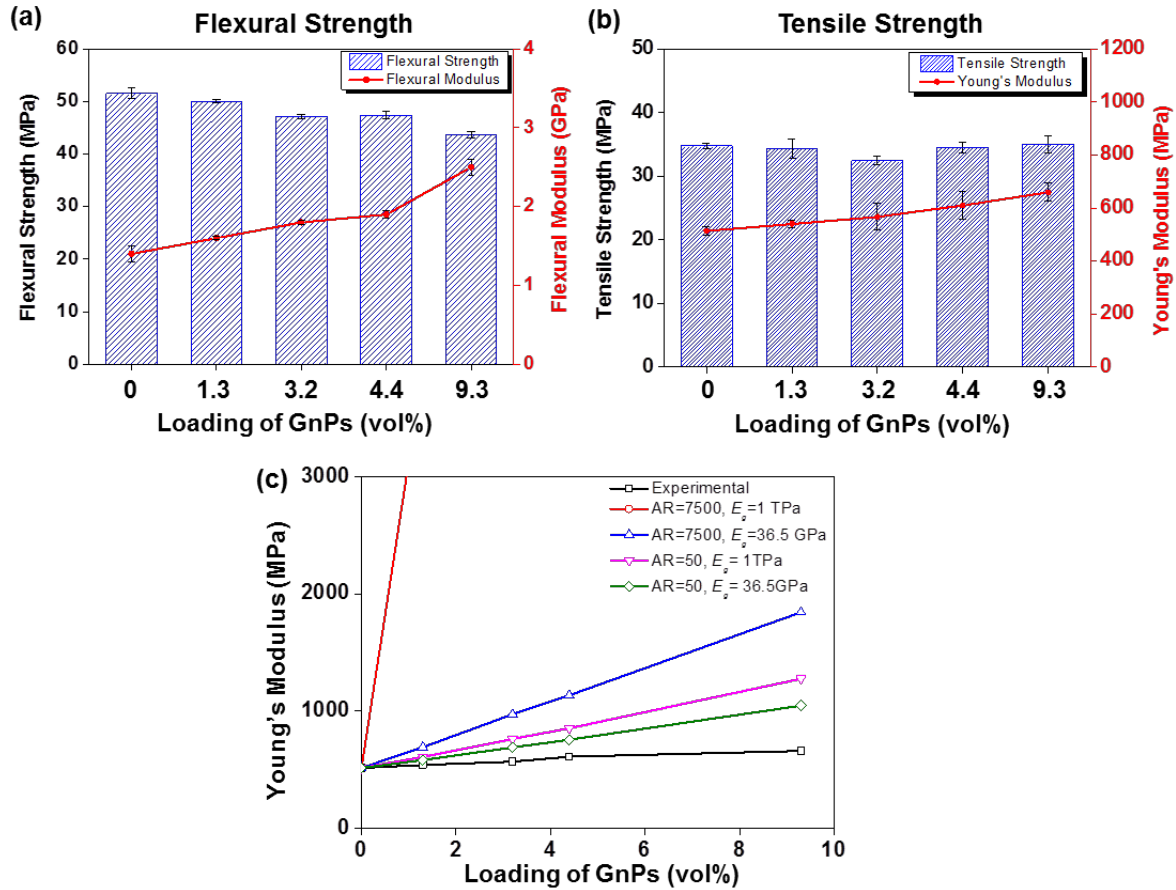
Figure 6-3 (a) Flexural strength and modulus of PP/GnP composites. (b) Tensile strength and modulus of PP/GnP composites. (c) The comparison between experimentally determined Young's modulus and the predicted modulus by the Halpin-Tsai equation with different GnPs parameters including the aspect ratio and Young's modulus. The error bars are standard deviations.

The tensile modulus was gradually improved with the incorporation of GnPs while the tensile strength was not significantly affected. The neat PP showed 908% elongation at break, indicating it is highly ductile and tough. Upon the addition of even a small amount of GnPs (1.3 vol %), the elongation at break was significantly reduced to 17%. This trend, together with the enhancement of modulus, indicated that the incorporation of GnPs led to an increase in stiffness but a decrease in toughness.

Table 6-3. Flexural and tensile properties of PP/GnPs composites.

Contents of GnPs (vol%)	Flexural strength (MPa)	Modulus of elasticity (GPa)	Tensile strength (MPa)	Young's modulus (MPa)	Elongation at break (%)
0.0	51.5±1.0	1.4±0.1	34.8±0.4	513.7±17.1	908
1.3	50.0±0.3	1.6±0.02	34.4±1.5	539.9±14.1	17
3.2	47.1±0.4	1.8±0.03	32.5±0.6	567.3±49.3	15
4.4	47.4±0.8	1.9±0.05	34.5±0.9	609.9±52.5	12
9.3	43.7±0.6	2.5±0.1	34.3±1.4	659.5±35.0	7

By applying a well-known mechanical property prediction model proposed by Halpin and Tsai, we can understand the influences of filler dispersion and morphology on reinforcement effects. Assuming that GnPs are randomly dispersed as three-dimensional system within the composite, the Halpin-Tsai equation is given by

$$E_c = E_m \left[\frac{3}{8} \frac{1 + \eta_L \xi \varphi_{vt}}{1 - \eta_L \varphi_{vt}} + \frac{5}{8} \frac{1 + 2\eta_T \varphi_{vt}}{1 - \eta_T \varphi_{vt}} \right] \tag{6-1}$$

$$\eta_L = \frac{\left(\frac{E_g}{E_m}\right) - 1}{\left(\frac{E_g}{E_m}\right) + \xi} \tag{6-2}$$

$$\eta_T = \frac{\left(\frac{E_g}{E_m}\right) - 1}{\left(\frac{E_g}{E_m}\right) + 2} \tag{6-3}$$

$$\xi = \frac{2\alpha_g}{3} = \frac{2l_g}{3t_g} \tag{6-4}$$

where E_c, E_g, and E_m represent Young's modulus of the composite, GnPs, and polymer matrix, respectively. α_g, l_g, and t_g refer to the aspect ratio, length and thickness of the GnPs, respectively

[143]. The degree of dispersion and possible morphology of fillers in the composite can be inferred by exploring how the experimental data deviate from predicted data [143]. The comparison between the experimentally measured Young's modulus of composites and the modulus predicted by the Happin-Tsai equation with various GnPs parameters is illustrated in Fig. 6-3c.

It is noteworthy that the prediction by the Halpin-Tsai equation largely depends on the parameter values used for E_g and the aspect ratio of GnPs. Theoretically, E_g for a single layer of graphene is ~1000 GPa and the aspect ratio (α_g) of GnPs used in this study is ~7500 based on the data sheet provided by XG Science. However, these values deviate greatly from the actual GnPs incorporated into the composites. In fact, the GnPs fillers employed in this study consisted of ~60 layers and in this case, the theoretical value of ~1000 GPa is not applicable for prediction due to the disturbance by the van der Waal's forces exerted between layers. The value of 36.5 GPa for GnPs has been suggested, and this value showed an improved accuracy when employed in the Halpin-Tsai equation [25], [144]. The theoretical aspect ratio of GnPs is ~7500 based on the data sheet given by XG Science. However, the structure of GnPs is deteriorated by sheer force during the melt-compounding process and aggregated due to van der Waal's forces. The distortion and agglomeration of GnPs can be observed in their SEM images as shown in Fig. 6-4. The XRD peak analysis by the Scherrer-Dye equation also suggested that the GnPs in the composites further aggregated and consisted of more layers (Table A-3). Therefore, the real aspect ratio of GnPs has significantly reduced and a decreased aspect ratio should be used for improved accuracy of prediction. When the theoretical GnPs parameters were replaced by the measured parameters, the predicted modulus greatly approached experimental values. This indicates that the characteristics of GnPs within the composite differ from theoretical parameters

90

and appropriate adjustment should be made for accurate prediction. Nonetheless, even after adjustments there still exists a gap between the experimental and predicted modulus. This is attributed to the imperfect interfacial bonding between GnPs and polymer matrix and a detrimental shape change of fillers induced during the compounding process. Moreover, the complete exfoliation of fillers and perfect interfacial bonding is assumed in the Halpin-Tsai equation, which is not the case in an actual composite. The gap between the experimental and predicted moduli can be reduced by improving the interfacial adhesion, such as via functionalization of fillers.
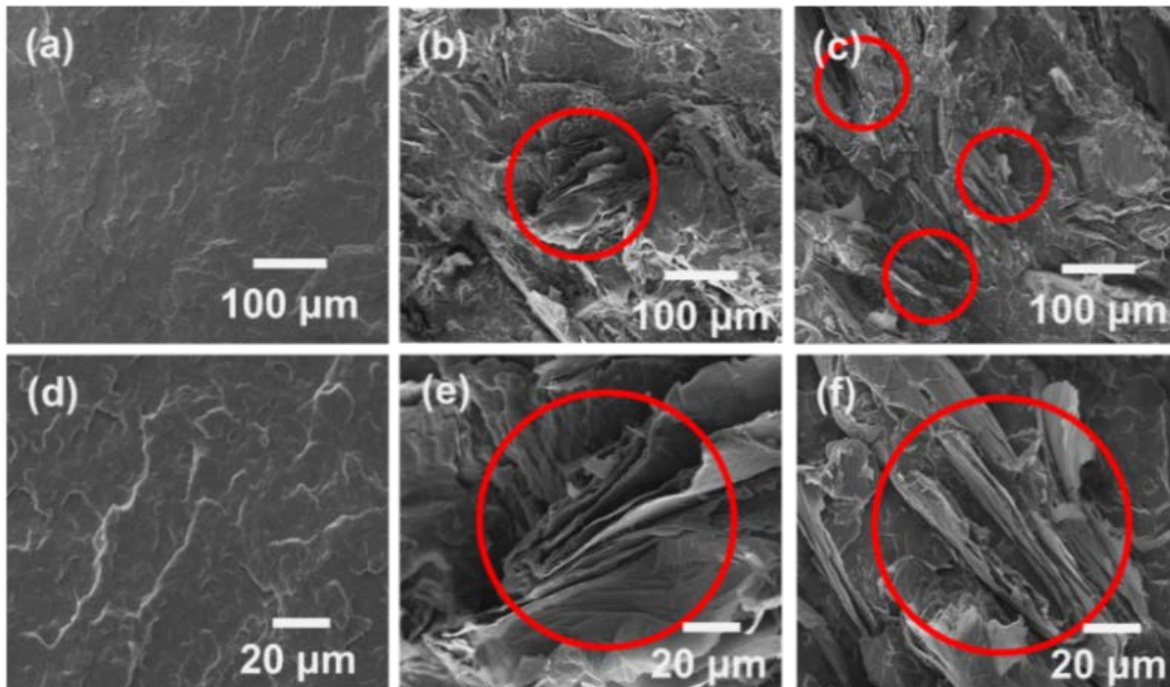
Figure 6-4. SEM images of (a and d) neat PP, (b and e) PP/GnPs _3.2 vol%, and (c and f) PP/GnPs _9.3 vol%, respectively. The GnPs were distorted and agglomerated by the sheer force induced during the compounding process. The size of GnPs in the composites should range 50~150 μm. The red circles indicate the GnPs dispersed within the composites.

6.3.3   Electrical properties of PP/GnPs composites

The in-plane and through-plane electrical conductivities of the composites were measured and illustrated in Fig. 6-5. Both in-plane and through-plane conductivities have steadily increased with increasing amount of GnPs. The in-plane electrical conductivity was 3.4×10^{-5} S·cm^{-1} with an addition of 3.2 vol% and reached 1.7×10^{-2} S·cm^{-1} with a loading of 9.3 vol%. The through-plane conductivity was 7.3×10^{-6} S·cm^{-1} with a loading of 3.2 vol % and increased up to 3.3×10^{-3} S·cm^{-1} upon addition of 9.3 vol% of GnPs. While both types of conductivities exhibited similar trends, the in-plane electrical conductivity was consistently greater than the through-plane conductivity by approximately an order of magnitude. This is due to the larger contact resistance when through-plane conductivity was measured.
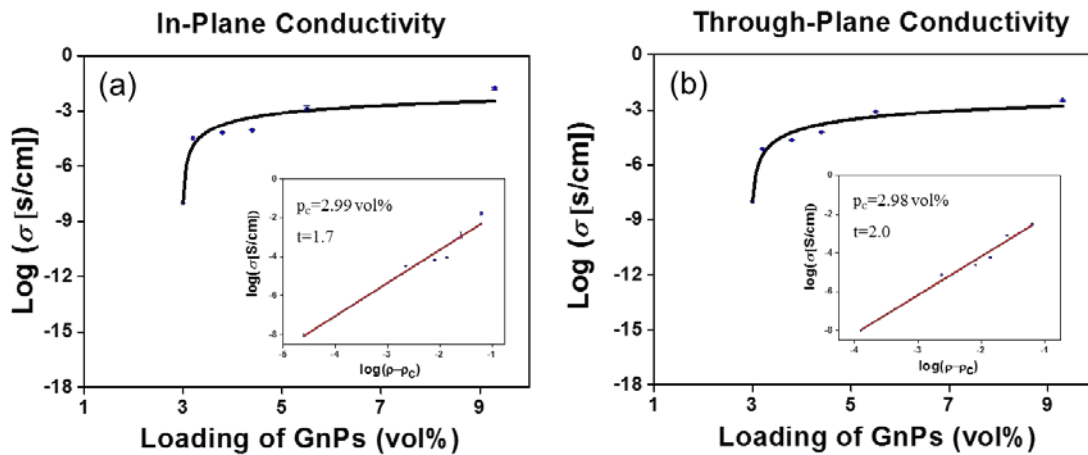
Figure 6-5. The in-plane (a) and through-plane (b) electrical conductivity of PP/GnPs composites as a function of volume concentration of GnPs. The inset shows a log-log plot of electrical conductivity versus (p-p_c) with p_c=2.99 vol% and t=1.7 for in-plane conductivity and p_c=2.98 vol% and t=2.0 for through-plane conductivity, respectively. The error bars are standard deviations.

The electrical properties of the composites are some of the characteristics that undergo the most dramatic transition upon addition of carbonaceous fillers. As GnPs are incorporated into a polymer matrix, both in-plane and through-plane electrical conductivities show a sudden increase

at a certain concentration of filler – approximately ~3 vol % in this study (Fig. 6-5). This particular concentration is called the percolation threshold and can be more accurately estimated by fitting experimentally obtained values to the power law as follows:

$$\sigma \sim (p - p_c)^t \qquad (3)$$

where σ is the electrical conductivity of the composite, p is the volumetric concentration of the filler, p_c is the percolation threshold, and t is the critical exponent which is related to the dimensionality of the composite system [145]. The drastic insulator-conductor transition of the composites for both in-plane and through-plane conductivities are depicted in Fig. 6-5 and the insets show a log-log plot of electrical conductivity as a function of (p-p_c). The percolation threshold was determined to be 2.99 vol % for in-plane and 2.98 vol % for through-plane conductivity, respectively. This is very low considering that the composites were processed by melt-compounding. Table 6-4 compares the percolation thresholds for composites with various polymer matrices and fillers from the literature [124], [146]–[148]. For example, Park et al. introduced xGnPs with a diameter less than 1 μm into PP by melt injection and obtained the percolation threshold greater than 15 wt% [147]. Kuvardina et al incorporated xGnPs with a diameter ~10 μm into PP via melt mixing and attained a percolation threshold of ~6.0 vol% [124]. This is clearly attributed to the usage of large-sized GnPs, and it has been shown that the electrical conductivity significantly benefits from the use a greater size of graphene [149]. By using larger-sized GnPs, the electrical percolation network can be achieved at lower filler concentration.

Table 6-4. Comparison of percolation thresholds for composites with various polymer matrices and fillers from the literature.

Ref.	Polymer matrix	Filler (size in µm)	Percolation threshold	Processing
[146]	High-Density Poly Ethylene (HDPE)	Graphite (5~8)	22.2 wt %	Single screw extruder
[147]	PP	XGnP-1 (1)	15 wt%	Twin screw extruder
[124]	PP	xGnP-5 (5) xGnP-10 (10)	6 vol % 4 vol %	Two roller mixing chamber
[148]	Phenylene Sulfide (PPS)	Expanded Graphite (20-200)	1 wt%	Twin rotary mixer
This study	**PP**	**GnP-H-100 (~150)**	**2.99 vol %**	**Twin screw conical extruder**

The critical exponents for in-plane and through-plane were close to one another, being 1.7 for in-plane and 2.0 for through-plane, respectively. A t value within the range of 1.6~2.0 indicates that the percolation networks were formed in three dimensions [150]. Having similar t values in the range of 1.6~2.0 and the adjacent percolation thresholds for both in-plane and through-plane, GnPs are highly likely to be dispersed in all three dimensions.

6.4   Summary

Very large-sized of GnPs (~150 µm) were incorporated into PP via melt extrusion followed by injection moulding. Although the initial nucleation for crystallization of the polymer matrix was likely to be promoted by the introduction of GnPs, the degree of crystallinity and the types of crystalline remained unchanged with increasing concentration of fillers. The inferior improvements in flexural and tensile strength could be attributed to the lack of efficient matrix-filler interfacial bonding. Also the discrepancy between the experimentally measured Young's

moduli and the moduli predicted by the Halpin-Tsai equation suggested that the aspect ratio and morphology of GnPs were compromised during the compounding process. Nonetheless, the use of very large-sized GnPs increased the electrical conductivity considerably and resulted in a very low percolation threshold of ~2.9 vol%. The fitting of experimental conductivities into the percolation theory suggested that GnPs were three-dimensionally dispersed within the composites. The electrical properties of the composite were greatly improved, but a higher degree of dispersion with enhanced interfacial interaction is desired to achieve excellent mechanical properties.

7. A Systematic Study on the Effects of Graphene nano-platelets (GnPs) Sheet Sizes on the Thermal, Mechanical, and Electrical Properties of Polypropylene (PP)/GnPs Composites

7.1 Introduction

In the previous chapter, we fabricated PP composites with very large sized GnPs. It was found that the use of ultra-large sized GnPs resulted in a very low percolation threshold, but relatively inferior enhancements were observed for flexural and tensile strength. In order for PP composites to be employed in a variety of fields, it is desirable that electrical, mechanical, and thermal properties of PP/GnPs are all improved. Particularly thermal stability and mechanical properties are important properties of interest for the field of automobile, aerospace, and military.

Previous studies in the literature have revealed that the performance of the PP/GnPs composites is highly dependent upon the physical characteristics of GnPs. For example, Liang et al. showed that Young modulus of neat PP (1.25 GPa) was 100% improved up to 2.5 GPa with use of GnPs with diameter less than 10 microns and thickness smaller than 5 nm while less reinforcement was achieved (Young's modulus reached 1.9 GPa) when greater sized GnPs (with diameter between 10 and 50 microns and thickness between 3.4 and 7 nm) was employed [110]. Kalaitzidou et al. revealed that neat PP with an initial flexural modulus of ~1.2 GPa reached a flexural modulus of 9 GPa with the addition of 20 vol% GnPs with a diameter of 1 μm whereas 5 GPa was obtained when 5 μm diameter GnPs were used [103]. Chunhui et al. also revealed that the flexural strength is inversely proportional to the size of graphite [151]. The percolation threshold of GnPs is also closely associated with the sheet size. Park et al. showed that exfoliated graphite nano-

platelets with a sheet size of 1 micron gave a percolation threshold of 15 wt% [147]. It was also reported that the use of GnPs with 5 μm and 10 μm in diameter exhibited a percolation threshold of 6 vol% and 4 vol%, respectively [124]. Therefore, it is essential to understand the effects of GnPs' physical properties on the performance of the composites from a manufacturing point of view when the composites are fabricated via conventional industrial machines. However, there are few studies that systematically investigate the influences of a wide range of GnPs' sheet size spanning from a few to hundreds of microns on the various properties of the composites.

As a follow-up study to the previous chapter, the objectives of this study were to investigate the effects of a physical property of GnPs on the thermal stability, crystallization behaviour of PP, tensile strength, and electrical conductivity of PP_GnPs composites. The size of GnPs used in this study spanned from a few microns to several hundred microns in diameter. Overall, it was revealed that the composites processed with a few micron-sized GnPs achieved an enhanced dispersion status and exhibited superior thermal stability. It was also shown that a significantly enhanced nucleation effect was achieved with a few micron-sized GnPs although the degree of crystallization (X_c) did not vary significantly. The best tensile property reinforcement was obtained with the incorporation of smaller-sized GnPs (M5 and C300). Tensile strength reached 46.3 MPa with the addition of 9.3 vol% of C300, which is 33.0% improvement of neat PP. Young's modulus of 817.2 MPa was achieved with the use of 9.3 vol% of M5, which is 59.1 % enhancement. This could be due to an enhanced state of dispersion with less agglomerated GnPs retained in original morphology within the composite. The lowest percolation threshold was achieved when the GnPs with the largest sheet size was used. The incorporation of H100, M25, and M5 exhibited percolations thresholds of ~2.99, 3.66, and 5.05 vol%, respectively. To maximize the advantage of large sheet size of GnPs, it is imperative to have a high degree of

dispersion with less agglomeration of fillers within the composite. The original morphology of fillers also should be retained during the incorporation process by conventional polymer machinery. An improved interfacial bonding between GnPs and PP is also essential to achieve further reinforcement of composites.

7.2   Materials and Methods

7.2.1   Materials

PP (HM20/70P) was obtained from Goonvean Fibres Ltd. and used as received. The average size of PP for this grade falls in the range of 0.055 to 0.077 mm with a density of 0.90 to 0.91 g/cm^{-3}. The melt flow index was measured to be 19.4 g/10min at 230°C and 2.16 kg (D4002, Dynisco Polymer Test Systems). Three different grades (Grade M, C, and H) of GnPs and two different sizes of grade M (5 and 25 µm) were purchased from XG Science. The dimensions and physical properties of GnPs are detailed in Table 7-1. The SEM images of each grade of GnPs are provided in Fig. 7-1.

Table 7-1. Dimensions and physical properties of GnPs used in this study. These values were provided in the technical sheet from XG science.

Grades of GnPs	H100	M25	M5	C300
Diameter (µm)	>150	>25	>5	>2
Thickness (nm)	~15	~6-8	~6-8	~5
Surface area (m^2/g)	50-80	120-150	120-150	~300
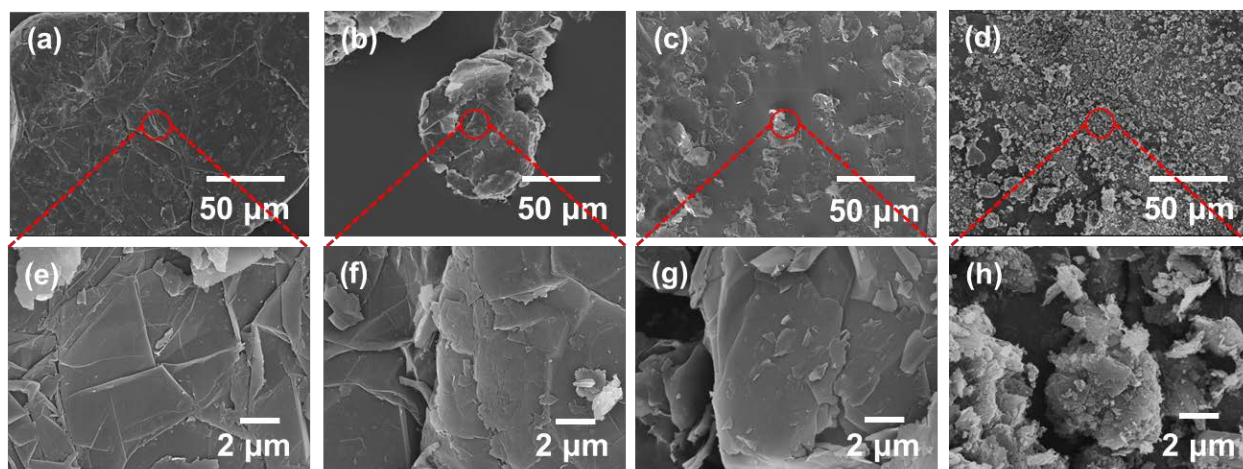
Figure 7-1. The SEM images of GnPs for each grade: (a and e) H100, (b and f) M25, (c and g) M5, and (d and h) C300.

7.2.2 Composites preparation

PP was compounded with grade M25, M5, and C300 GnPs with desired mass fractions ranging from 5 to 20 wt%. The mass fraction was converted to volume fraction, and the compositions of all the samples are summarized in Table 7-2. The data for PP composites with H100 was reproduced from Chapter 6. Both PP and GnPs were suspended in ethanol and mechanically stirred for an improved dispersion. The mixture was dried in a vacuum oven at 60°C for 24 hr and fed into the counter-rotating conical micro-compounder (Ruiming, SJZS-07A). The compounded strands were pelletized by a pelletizing machine and desiccated again at 60°C for 12 hr to avoid moisture inclusion. The dried and pelletized extrudates were then added into an injection moulding machine. The settings for extruder and injection moulding machine was identical to Chapter 6.

Table 7-2. Summary of composite compositions and corresponding volume percent.

Filler		PP	
wt%	vol%	wt%	vol%
H100			
0	0	100	100
3	1.3	97	98.7
7.5	3.2	92.5	96.8
10	4.4	90	95.6
20	9.3	80	90.7
M25			
5	2.1	95	97.8
10	4.4	90	95.6
15	6.7	85	93.3
20	9.3	80	90.7
M5			
5	2.1	95	97.8
10	4.4	90	95.6
15	6.7	85	93.3
20	9.3	80	90.7
C300			
5	2.1	95	97.8
10	4.4	90	95.6
15	6.7	85	93.3
20	9.3	80	90.7

7.2.3   Characterizations

7.2.3.1   Thermal behaviour and stability

The thermal behaviour of the PP/GnPs composites were examined by means of DSC using a thermal analyzer (TA Q2000, USA). The samples were scanned from -30 to 250°C under a nitrogen atmosphere with ramping rates of 10°C/min. The specimens were treated at 250°C for three minutes to eliminate the thermal history. The thermal stability was studied by means of TGA using a thermal analyzer (TA Q500, USA). The samples were treated from 20 to 800°C with a heating rate of 10°C/min under a nitrogen condition.

7.2.3.2   Structural and morphological measurements

The structural analysis of PP/GnPs composites were conducted by means of x-ray diffraction (XRD) using Rigaku Miniflex (Cu-Kα radiation, λ=1.54184 Å). The morphology of the composites was investigated by SEM (Zeiss Leo 1550).

7.2.3.3   Tensile strength measurement

Dog bone tensile specimens were prepared by our injection moulding machine, and each specimen has a length of 75 mm, a thickness of 2 mm, and a parallel length of 30 mm. Five samples were tested on a universal testing machine (4.4kN, eXpert 7603, ADMET, USA) with a cross-head speed of 5 mm/min at an ambient atmosphere in accordance to ASTM D638-14.

7.2.3.4   Electrical conductivity measurement

The in-plane electrical conductivity (σ_I) was measured by a four-point probe method. Specimens were trimmed into dimensions of 15 x 10 x 2 mm, and the polymer-rich surface was removed prior to measurement. The in-plane and through-plane conductivities were determined by the

methodologies described in Section 3.3.

7.3 Results and Discussion

7.3.1 Thermal stability
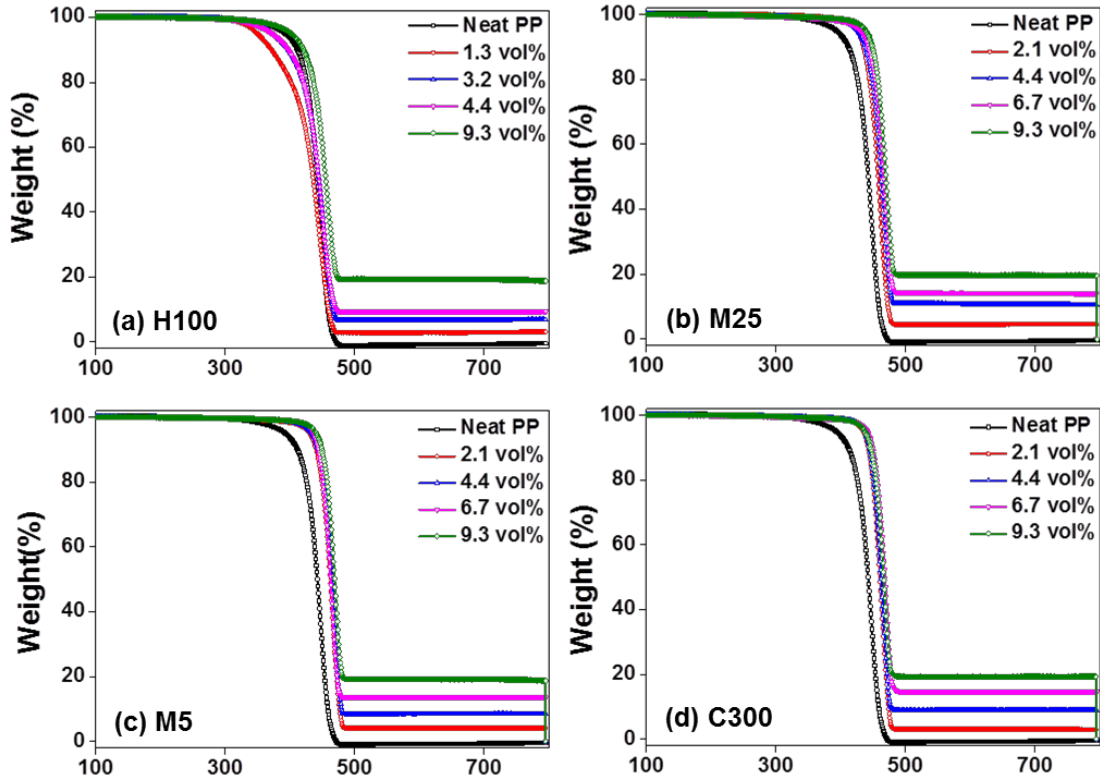
Figure 7-2. The TGA curves of PP/GnPs composites with (a) H100, (b) M25, (c) M5, (d) C300, respectively.

TGA and differential thermo-gravimetric (DTG) curves of PP/GnPs composites with all different grades of GnPs were described in Fig. 7-2 and 7-3, respectively, and the thermal stability parameters estimated from TGA are provided in Table 7-3. $T_{5\%}$ (5% weight loss temperature) and T_{max} (the maximum mass loss temperature) are shown in Table 7-3 with respect to each GnPs grade.
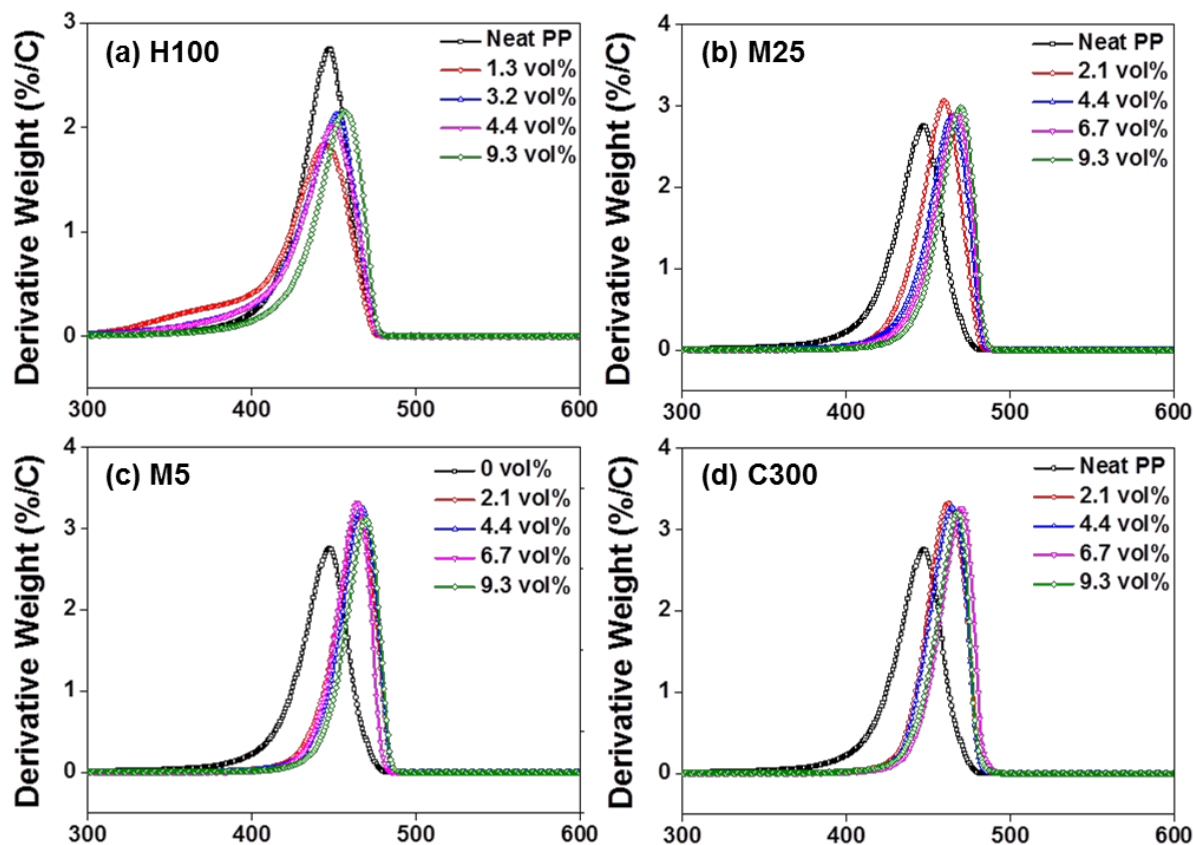
Figure 7-3. DTG curves of PP/GnPs composites with (a) H100, (b) M25, (c) M5, (d) C300, respectively.

Fig. 7-4 illustrates an improved thermal stability as the contents of GnPs increases within the composite for all the grades. It is evident that the GnPs with a diameter less than 25 μm (M25, M5, and C300) shows superior effectiveness as compared to H100. While T_{max} is heightened with the addition of any grade of GnPs, the composites incorporated with very large sized GnPs (H100) exhibited inferior thermal stability at the initial stage of thermal decomposition in comparison to neat PP as indicated by $T_{5\%}$ (Fig. 7-4a). In general, GnPs are known to improve a thermal stability due to its barrier effect and removal of free-radicals initiating the decomposition of polymers [131], [136]. In addition, the dispersed GnPs sheets allow the thermal conduction and uniform distribution of heat spread in the polymer matrix, leading to an improved thermal

stability. However, the SEM images show that H100 GnPs are highly re-stacked and agglomerated as compared to other small-sized GnPs (Fig. 7-8), and this inferior dispersion of H100 could result in a reduced thermal stability. Since the advanced distribution of fillers within the matrix is achieved with smaller-sized GnPs, a significantly increased thermal stability is observed with these fillers such as M25, M5, and C300.
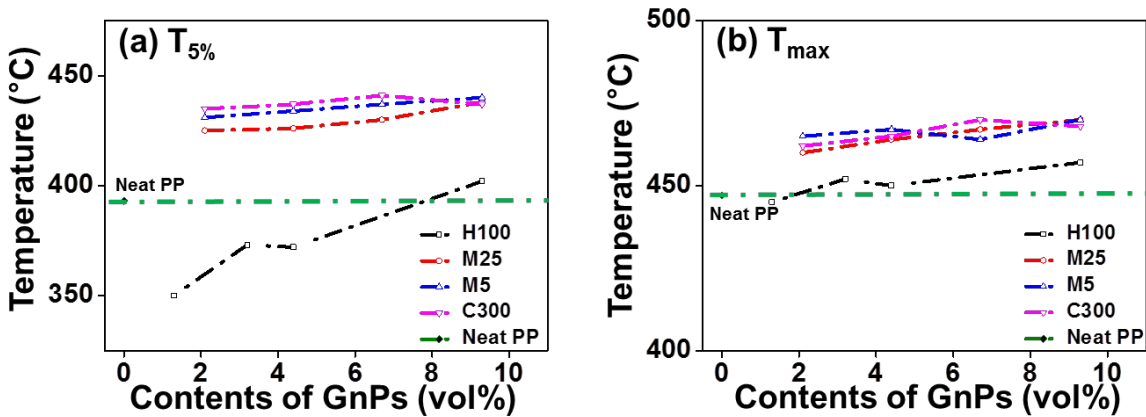
Figure 7-4. The variations of (a) $T_{5\%}$ and (b) T_{max} with increasing amount of GnPs with respect to each grade.

Table 7-3. Parameters extracted from TGA with respect to GnPs grades and their contents in the composites.

	Neat PP	H100				M25				M5				C300			
Contents of GnPs (vol%)	0.0	1.3	3.2	4.4	9.3	2.1	4.4	6.7	9.3	2.1	4.4	6.7	9.3	2.1	4.4	6.7	9.3
Contents of GnPs (wt%)	0.0	3.0	7.5	10.0	20.0	5.0	10.0	15.0	20.0	5.0	10.0	15.0	20.0	5.0	10.0	15.0	20.0
Residual Amount (wt%)	0.0	3.1	6.9	9.5	18.9	4.5	10.4	14.2	19.5	4.1	8.5	13.6	19.2	5.9	8.9	14.7	19.3
$T_{5\%}$	393	350	373	372	402	425	426	430	438	431	434	437	440	435	437	441	437
T_{max}	447	445	452	450	457	460	464	467	470	465	467	464	470	462	465	470	468

104

7.3.2 Effect of GnPs on the crystallization of PP

Crystallization (T_c) and melting temperatures (T_m) of PP composites with each grade of GnPs were measured by means of DSC and described as a function of GnPs contents in Fig. 7-5. The crystallization parameters extracted from DSC are detailed in Table A-1. It is evident that the addition of GnPs considerably increases T_c, indicating that GnPs serve as nucleating agents [140]. This nucleating effect is amplified as the size of GnPs decreases. T_c increased by 14.3 °C with the addition of 9.3 vol% of C-300 whereas the addition of 9.3 vol% H100 only escalates T_c by 6.1°C. This is likely due to well-dispersion and large surface area of C-300. Since the GnPs fillers act as seeds for heterogeneous nucleation, crystallization can be facilitated at relatively higher temperatures when larger surface areas are available from small-sized GnPs. While the crystallization temperature is largely influenced by the addition of GnPs, the degree of crystallinity (X_c), calculated by melting enthalpy (ΔH_m) measured from DSC, of the composites was not changed very significantly with the addition of any size of GnPs as shown in Table A-1. The degree of crystallinity of neat PP was 60, and it increased up to 63 with 9.3 vol% of M25 GnPs, and up to 62 with 9.3 vol% of M5 GnPs. This enhancement is rather insignificant considering a number of fillers incorporated into the PP matrix. Moreover, unlike the T_c, T_m of composites does not deviate considerably from that of neat PP (Fig. 7-5b). Addition of 9.3 vol% of H100 only increases T_m by 0.6 °C, and only 2.9 °C rises with 9.3 vol% of C300. The less variation in T_m indicates that the crystal types of PP remain invariant with the addition of all different grades of GnPs. T_m is largely dependent upon the forms of crystals. For instance, α-crystals show a melting point around ~165°C and β-crystals around 150-160°C, respectively [152]. In the XRD analysis below, β-crystals are observed from the composites with H100, M25, and M5, but it can be seen that amount of β-crystals formed is insignificant and hence does not

affect T_m.
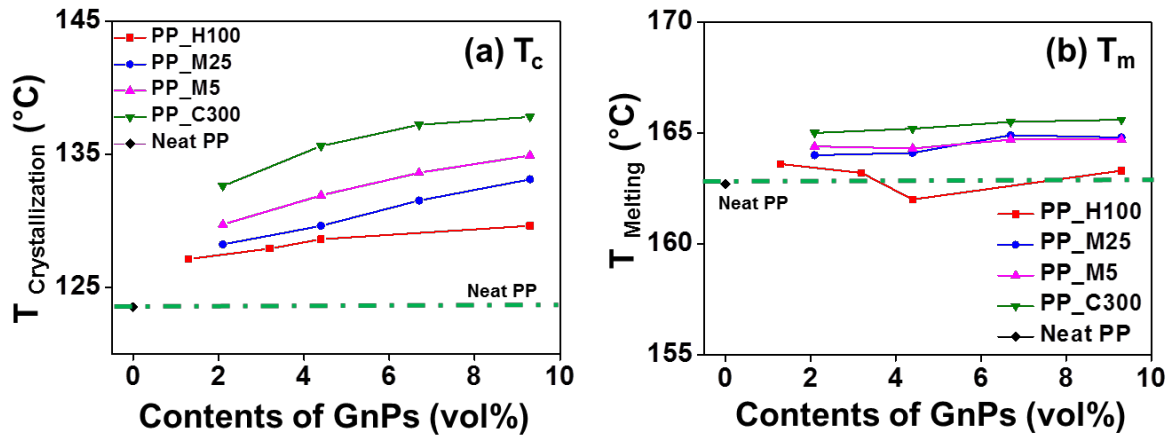
Figure 7-5. (a) Crystallization (T_c) and (b) melting temperatures (T_m) of PP_GnPs composites as a function of GnPs contents.

The investigation on the crystallization of PP by means of XRD is illustrated in Fig. 7-6. Neat PP exhibits five main peaks at 14.08°, 16.95°,18.5°, 21.2°, and 21.85°, which are responsible for (110),(040),(130),(111), and (041) of α-crystals, respectively. Upon addition of GnPs, (040) plane at 16.95° become significantly dominant, and the growth of (060) plane peak is also observed. Further, (300) plane of β crystals also appeared for the composites incorporated with H100, M25, and M5. It should be noted that all the planes that showed significant peak growth with the presence of GnPs are in the general form of (0x0) type, which can be crystallographically in line with the GnPs (002) plane. It was shown the GnPs may serve as a nucleation site and the nucleation begins around the GnPs [138], [140]. When this occurs, it is possible that the PP chains can exhibit epitaxial growth on GnPs as c-axis of GnPs is merged with b-axis of PP, indicating that (002) plane of GnPs is matched with (040) plane of PP. Similar phenomena were also reported in several studies [27], [138], [153].

The appearance of β-crystals is not observed with the composites with C300, and this could be

106

due to saturation effect associated with the small size of C300. When the size of GnPs is small, the greater number of GnPs particles will be present per unit volume as compared to larger-sized GnPs for the same loading. In this case, there might not be enough polymer chains that can orient and align along with all the GnPs particles when the GnPs are of high loading. Kalaitzidou et al. showed that this saturation occurred with only 1 vol% of GnPs with a sheet size of 1 μm [138]. The saturation effect diminishes as the size of GnPs increase, and hence the particular plane induced by GnPs can be observed with high contents of GnPs if their diameter is sufficiently large. For example, the (300) plane was observed from PP_M5 composites with up to 4.4 vol% of GnPs while the PP_M25 composites exhibited the peak for (300) plane with GnPs contents up to 6.7 vol%. The peak for (300) appeared from the all the PP_H100 composites with GnPs loading of up to 9.3 vol%. This saturation was also observed from the PP composites incorporated with CNTs [154].

It is known that β-crystals of PP give an enhanced impact strength [155]. Since GnPs promote the formation of β-crystals of PP, the impact strength will increase with the addition of GnPs and the highest impact strength will be obtained at a GnPs loading that saturates the β-crystal formation. Therefore, the particular GnPs loading that shows the maximum impact strength will vary with the different size of GnPs due to the saturation effect. Such trend has been observed elsewhere [156].
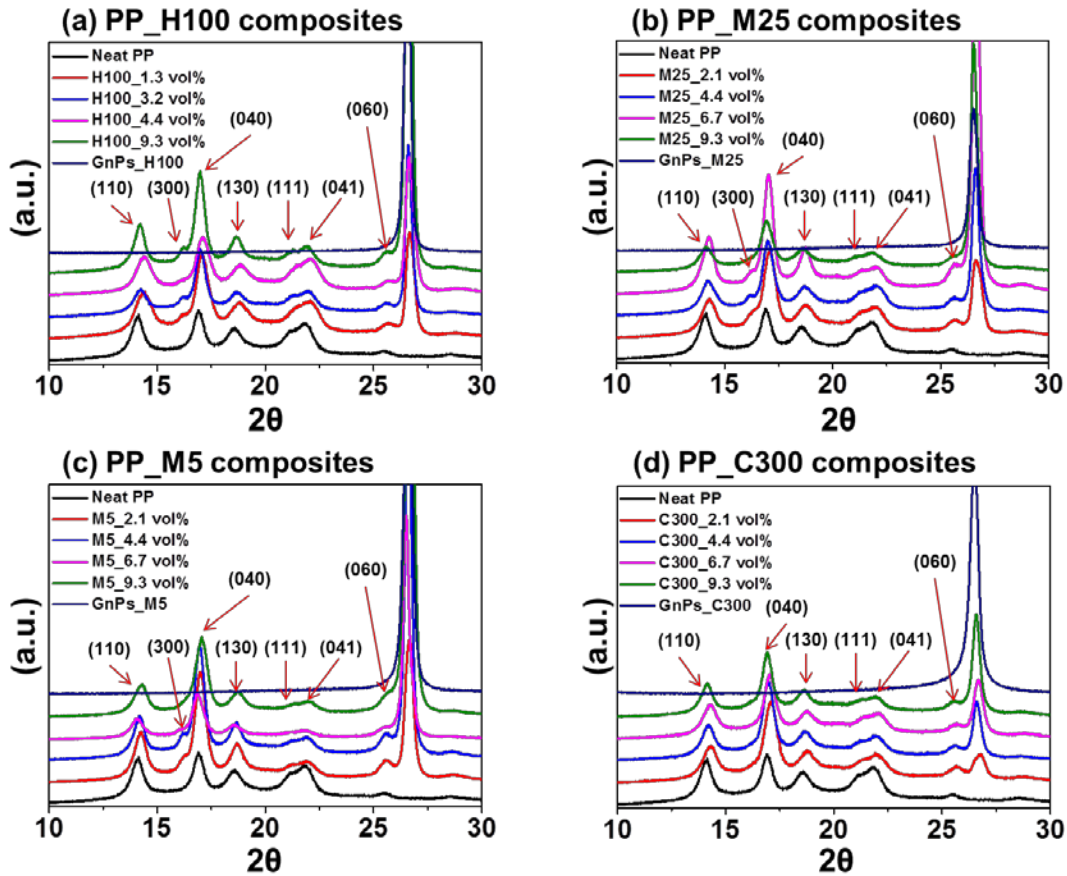
Figure 7-6. XRD curves of neat PP and PP composites compounded with (a) H100, (b) M25, (c) M5, and (d) C300, respectively.

7.3.3   Tensile strength

Tensile strength and Young's modulus were determined as a function of GnPs contents (vol%) within the composites. The stress-strain (SS) curves of all the composites are described in Fig. 7-7 with extracted parameters detailed in Table 7-4. The entire SS curve for neat PP is available in the supplementary information (Fig. A-1). Overall, tensile strength and Young's modulus were consistently enhanced as the amount of GnPs incorporated increased except for the composites processed with H100. For the PP_H100 composites, Young's modulus was significantly enhanced while the tensile stress failed to show a considerable improvement. However, both

tensile strength and Young's moduli were improved for all the composites incorporated with M25, M5, and C300, respectively. The failure of increasing tensile strength with H100 can be attributed to inferior interfacial bonding between the polymer matrix and filler, largely caused by agglomeration, and thereby prevent the composites from achieving a high degree of dispersion. Further, the morphology of H100 has been changed from platelets to spherical shapes as seen in Fig. 7-8a, which can also give adverse influences on reinforcement.
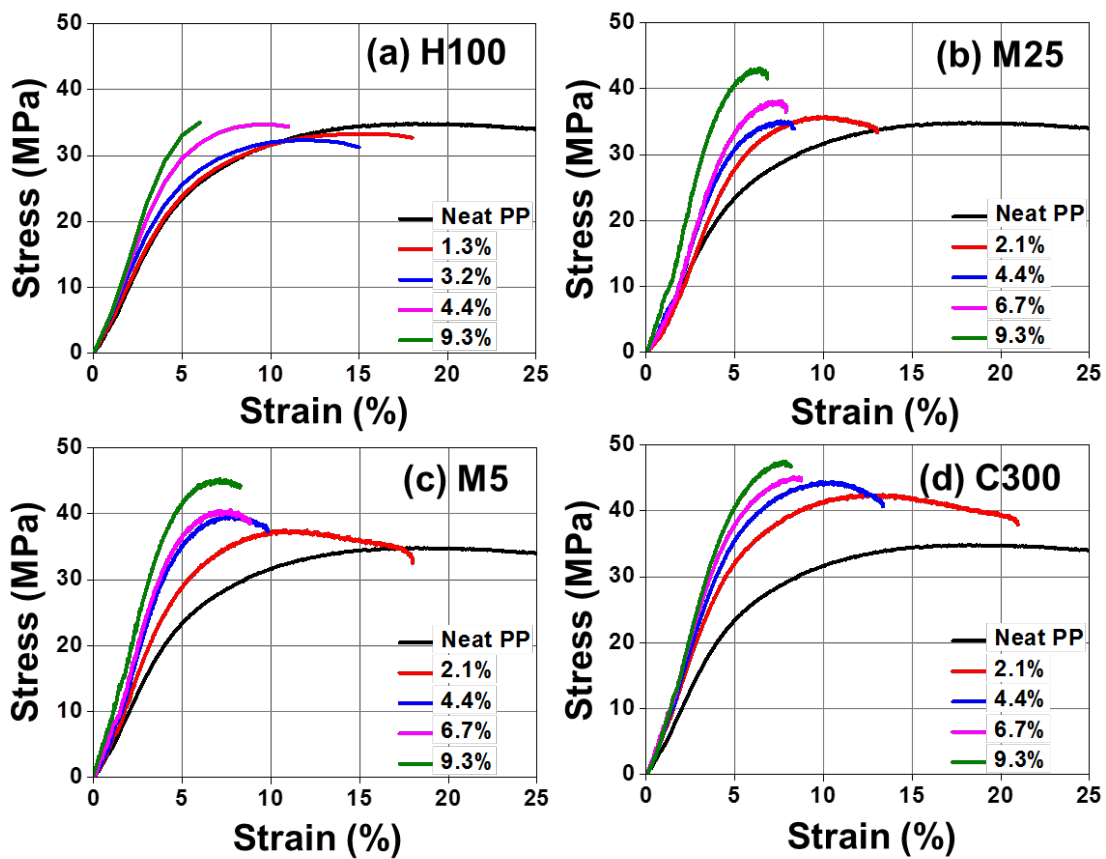
Figure 7-7. The SS curves of PP composites incorporated with (a) H100, (b) M25, (c) M5, and (d) C300, respectively.

The improvement of tensile strength was most effective with the use of C300 grade of GnPs (Table A-4). The smaller size of GnPs, the greater efficiency of reinforcement was obtained. The addition of only 2.1 vol% of C300 resulted in reaching a tensile strength greater than 40 MPa,

which is 17.5% of improvement from neat PP. Also, 28.3% enhancement for Young's modulus was observed with incorporation of 2.1 vol% of C300 (Table A-4). It has been reported that greater significant reinforcement can be achieved with the reduced size of GnPs [123], and the mechanical property enhancement is strongly inversely proportional to the size of filler in many studies [157], [158]. This could be due to increased surface areas that expedite efficient stress transfer between polymer matrix and fillers [159]. An increased surface area of fillers also offers a greater hindrance to crack propagation leading to an improved strength [123]. Moreover, interestingly the largest elongation at break for the loading of 2.1 vol% of GnPs was also obtained with C300. This could be indicative of the greater degree of dispersion and less agglomeration of C300 within the matrix since affinity between PP and GnPs does not change with GnPs size. In addition, C300 and other grades of GnPs with small sheet size did not suffer from bending or buckling as seen from Fig. 7-8, which helps boost the reinforcement effects. Therefore, the efficient reinforcement with small-sized fillers can be attributed to combined effects of better dispersion, less agglomeration, and retention of the original filler morphology within the polymer matrix.

Table 7-4. Tensile parameters extracted from SS curve with respect to GnPs grades and their contents in the composites.

	Neat PP	H100				M25				M5				C300			
Contents of GnPs (vol%)	0.0	1.3	3.2	4.4	9.3	2.1	4.4	6.7	9.3	2.1	4.4	6.7	9.3	2.1	4.4	6.7	9.3
Tensile Strength (MPa)	34.8 ±0.4	34.4 ±0.4	32.5 ±0.6	34.5 ±0.9	34.3 ±1.4	35.7 ±0.7	35.3 ±0.6	37.7 ±1.8	41.6 ±1.9	37.5 ±0.4	39.6 ±1.1	40.2 ±1.0	43.6 ±1.7	40.9 ±1.7	43.8 ±1.0	45.2 ±1.6	46.3 ±0.8
Young's Modulus (MPa)	513.7 ±17.1	539.7 ±17.1	567.3 ±49.3	609.9 ±52.5	659.5 ±35.0	573.7 ±81.8	562.7 ±102.4	627.8 ±145.0	785.4 ±45.8	614.6 ±37.9	698.1 ±32.2	719.2 ±56.1	817.2 ±54.3	658.9 ±35.3	726.8 ±14.1	741.9 ±28.7	775.2 ±18.3
Elongation at break (%)	908	17	15	12	7	13	10	9	7	18	10	9	8	21	14	9	8
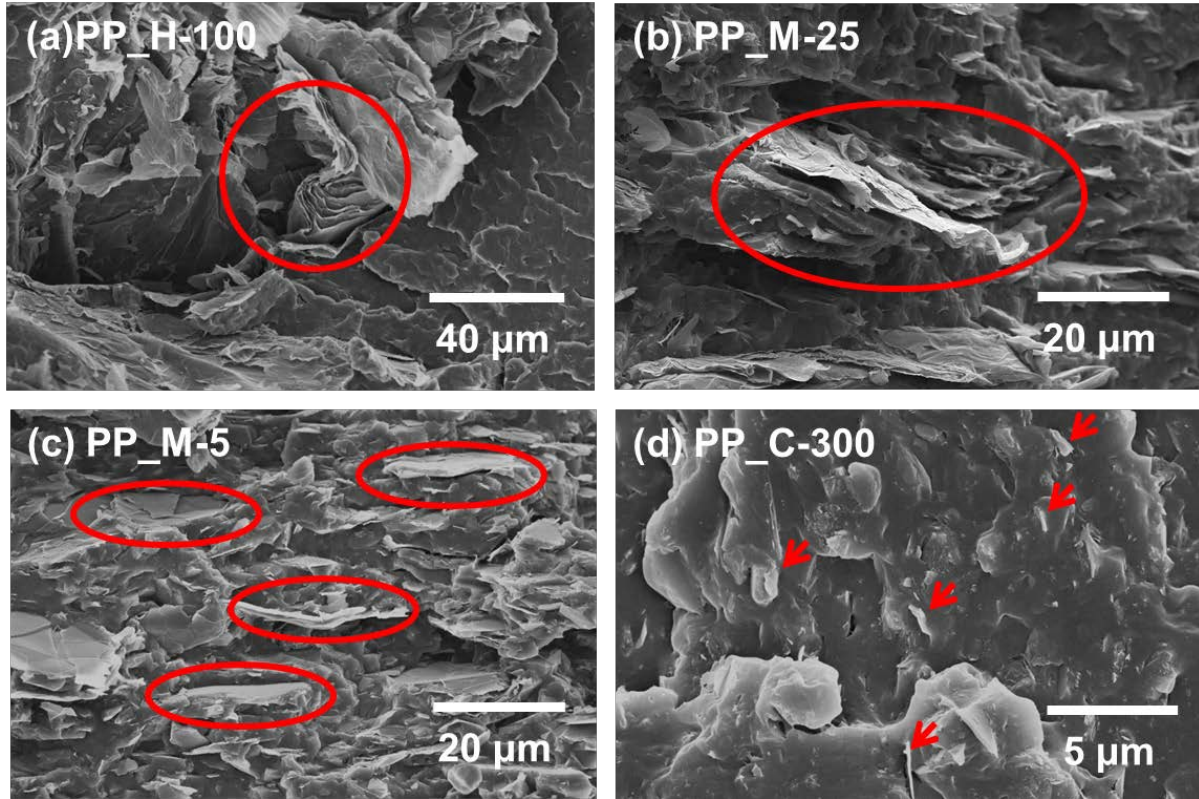
Figure 7-8. The SEM images for PP/GnPs composites with (a) H100, (b) M25, (c) M5, and (d) C300, respectively. GnPs are indicated by circles or arrows in red.

7.3.4 Electrical conductivity

The in-plane and through-plane electrical conductivities of each composite were measured and described in Fig. 7-9. As the amount of GnPs fillers in the composite increases, the composite undergoes an abrupt insulator-conductor transition, and there exists a particular concentration where electrical conductivity exhibits a sudden increase. This specific concentration is commonly referred to as the percolation threshold [145]. The percolation threshold can be determined by fitting experimentally observed values to the power law as follows:

$$\sigma \sim \left(p - p_c\right)^t \tag{3}$$

111

where σ is the electrical conductivity of the composite, p is the volumetric content of filler within the composite, p_c is the particular percolation content, and t is the critical exponent [145].
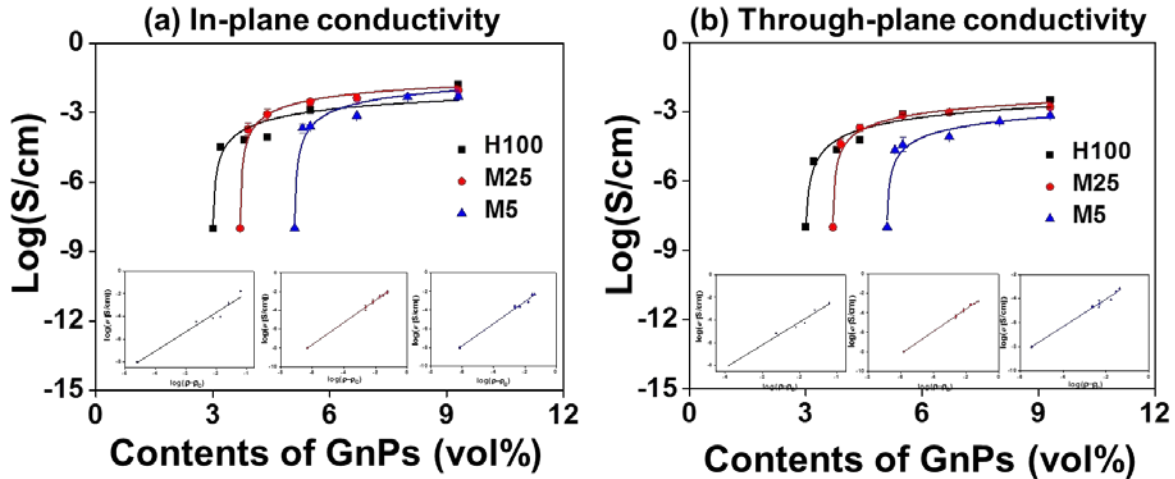
Figure 7-9. The (a) in-plane and (b) through-plane electrical conductivity of PP/GnPs composites with each grade of GnPs as a function of volume concentration of GnPs. The inset shows a log-log plot of electrical conductivity versus (p-p_c). The error bars are standard deviations.

The estimated percolation thresholds for the composites with each GnPs grade are detailed in Table 7-5. It should be noted that the percolation threshold was not determined for the composites with C300 because the C300 composite was still insulating even with 9.29 vol% of loading. A very low percolation threshold is achieved with the use of H100 as compared to other studies where GnPs were used as fillers and processed by conventional melt compounding as shown in Table 7-5. H100 exhibited the percolation thresholds of 2.99 vol% for in-plane and 2.98 vol% for through-plane conductivity, respectively. In fact, the percolation threshold from H100 was expected to be further low, but the compromised morphology of fillers may have led to an increased percolation threshold. The percolation threshold for M25 and M5 was 3.66 vol% and 5.05 vol%, respectively. It is clearly observed that the percolation threshold increases as the sheet size of GnPs reduces, and this trend confirms the well-known relationship between the

aspect ratio of fillers and percolation threshold [160]. For the composites to become electrically conductive, the incorporated conducting fillers should make contact one another and construct an inter-connected pathway for electrons to travel. Using fillers with large-sized sheet size, this conductive pathway will be readily formed with low concentration. This is highly beneficial because a great processibility and physical property can be retained. In order to further reduce percolation threshold, it is desired that the compromising of fillers be minimized by optimizing processing conditions or by employing other techniques that improve dispersion of fillers and introduce less sheer force to compounding, for example as solid-state ball milling as seen in Table 7-5.

Interestingly, while it is usual that a higher conductivity is observed with a large sheet size of fillers at the same loading of fillers, the composites with M25 exhibited higher conductivity at the GnPs loadings around 4~5 vol% for both in-plane and through-plane. This could be due to an inferior state of dispersion caused by agglomeration of H100. As it was seen from Fig. 7-8, H100 GnPs are considerably agglomerated, leading to a reduction in lateral sheet size and reduced number of dispersed particles per unit volume. This is very likely to produce a negative influence on the electrical conductivity. Nevertheless, the use of H100 is still beneficial for achieving low percolation threshold which gives significant advantages for obtaining a great processibility from a manufacturing point of view.

Table 7-5. Comparison between the literature and the percolation thresholds of the composites from this study.

Ref.	Polymer matrix	Filler (diameter in μm)	Percolation threshold		Processing
[124]	PP	xGnP-5 (5)	6 vol%		Two roller mixing chamber
		xGnP-10 (10)	4 vol%		
[147]	PP	xGnP-1 (1)	15 wt%		Twin screw extrusion
[135]	LLDPE	xGnP-15	12 wt%		Solution compounding
[161]	HDPE	xGnP-15	10-15 vol%		Twin screw extrusion
			3-5 vol%		Solid State Ball Milling
This study	PP		In-plane	Thru-plane	Twin screw extrusion
		xGnP H100 (~150)	2.99 vol%	2.98 vol%	
		xGnP M25 (~25)	3.66 vol%	3.66 vol%	
		xGnP M5 (~5)	5.05 vol%	5.05 vol%	
		xGnP C300 (~2)	> 9.29 vol%	> 9.29 vol%	

7.4 Conclusions

Four classes of GnPs (H100, M25, M5, and C300) with different physical property were incorporated with PP to produce PP_GnPs composites, and their thermal stability, the effect of GnPs on the crystallization behaviour of PP, tensile strength, and electrical conductivity were thoroughly studied. The PP composites incorporated with GnPs smaller than 25 μm in diameter exhibited an improved thermal stability as indicated by $T_{5\%}$ and T_{max}. The addition of H100 into PP did not result in an enhanced thermal stability, especially at the initial stages of decomposition. The GnPs exert a considerable nucleating effect on the crystallization of PP by increasing T_c and by inducing particular planes, such as (300), (040), (060), which can be formulated by epitaxial growth of polymer chains on the GnPs. The X_c was not significantly increased, however. The greatest efficiency in tensile strength reinforcement was achieved with

the use of C300. The lowest percolation threshold was obtained when the GnPs with largest sheet size (H100) was incorporated into a polymer matrix. It was shown from this study that physical dimensions of GnPs exert a significant influence on the performance of the final composites. The GnPs with smaller sheet size is recommended for the purpose of increasing thermal stability and mechanical strength while high electrical conductivity is readily achieved with large-sized GnPs. To achieve a composite with all-around performances, a high dispersion of large-sized GnPs with retained original morphology should be accomplished with improved interfacial interactions.

8. Conclusions and Recommendations

8.1 Conclusions

To develop electrically conductive polymer nano-composites, a variety of graphene-based carbonaceous fillers have been combined with a polymer matrix via two distinct fabrication techniques. The first two studies presented the flexible polymer composites prepared via infiltration of three-dimensional free-standing graphene foam with PDMS. Due to the unique inter-connected and percolated network of graphene within the foam, these composites exhibited a high electrical conductivity at low loadings of fillers. The improved consistency in electrical conductivity under a uniaxial tensile train was obtained when high aspect ratio fillers were used to construct the filler matrix. The last two studies demonstrated PP composites incorporated with GnPs by means of conical twin screw extrusion followed by injection moulding. GnPs with very large diameter was first processed with PP, and their influences on thermal, mechanical, and electrical properties were investigated. A follow-up study extended the inclusion of GnPs with different flake dimensions and examined their impacts on the thermal stability, crystallization behaviour of PP, tensile property, and electrical conductivity of PP/GnPs composites.

In Chapter 4, two grades of graphite with different diameters were used as a starting material; graphite with a diameter large than 100 microns (denoted as LFG) and a diameter between 2 and 15 microns (denoted as SFG) was used to synthesize GO solution by Hummer's method. As-synthesized GO solutions from each size of graphite were directly used to produce GO foams by means of freeze casting. The freeze-dried GO foams were thermally reduced to restore electrical conductivity and subsequently backfilled with PDMS. XRD confirmed the variation of interlayer distance due to oxidation and reduction, and Raman spectroscopy revealed the structural

variation on the basal plane of graphene sheets upon oxidation and reduction process. It was found that I_D/I_G ratio was decreased with use of LFG, indicating less amount of edge structures were present in the bulk graphene foam. This appeared to contribute to the enhanced intrinsic electrical conductivity of graphene foam made with LFG. Both in-plane and through-plane conductivities were significantly improved when LFG was utilized to prepare the filler matrix. This could be due to the better intrinsic electrical conductivity and the reduced number of contact junctions on the percolated pathway. The contact resistance largely originates from these contact junctions and the use of LFG significantly diminished contact resistance by reducing the number of contact junctions on the pathway of electrons. This study clearly demonstrated the benefits of using three-dimensional graphene foam with large sized graphite flake, which will significantly contribute to the development of conductive polymer composite with a low filler loading.

In a follow-up study, GNRs with a high aspect ratio were employed to produce the three-dimensional filler matrix to further improve electrical conductivity. To further improve the practicability of such composites in the area of wearable electronics, a set of apparatus capable of measuring electrical conductivity under a uniaxial tensile strain was designed and implemented. GNRs were synthesized by unzipping of MWCNTs by means of chemical oxidation and used to fabricate the composites with the same technique as previous study. It was revealed that thin and long strips of GNRs were highly accumulated in between the growing ice crystals, creating tremendously large-sized sheets aligned with the direction of the growth of ice crystals. These large-sized GNRs-accumulated sheets provided great overlapped contact areas within the percolated network. With such filler network constructed within, polymer composites exhibited a significantly improved consistency in electrical conductivity against a uniaxial elongation. This finding demonstrated the advantage and possibility of GNRs-based polymer composites in the

117

field of wearable electronics.

Having learned from Chapter 4 that graphene sheets with large diameter helped achieve a high electrical conductivity with low filler content, we have incorporated the GnPs with largest size available in the market (GnPs-H100) into PP by means of twin screw extrusion. The low percolation threshold of ~2.99 vol% was observed for in-plane electrical conductivity. However, relatively inferior enhancements in thermal stability and mechanical properties were revealed. The inferior mechanical performance can be attributed to the lack of efficient attachment of polymer melt to the fillers. During the compounding process, considerable shear force is introduced into the compounds, leading to compromised aspect ratio and deteriorated morphology of fillers. The SEM images confirmed that a high aspect ratio and platelet-like shape of H100 were not retained within the PP composites.

Since it is imperative from a manufacturing point of view to understand the influences of GnPs flake size on a variety of properties of PP/GnPs composites, in a follow-up study we have extended the inclusion of GnPs with a range of different flake size spanning from a few microns to hundreds of microns. TGA found that the thermal stability was most enhanced with the use of C300, which has the smallest diameter (~3μm). This could be due to a high degree of dispersion achieved with C300, resulting in a uniform heat spread within the composite along with the role of GnPs that provide barrier effect and scavenge the free radicals initiating decomposition of polymers. The influences of GnPs on the crystallization behaviour of PP were explored by means of DSC and XRD. It was shown that GnPs served as seeds for heterogeneous nucleation, and T_c was significantly increased with decreasing GnPs size owing to the greater surface area provided by the smaller size of GnPs. XRD revealed that GnPs exerted a minor induction effect of β-crystals. The most enhanced tensile properties were observed with C300. This could stem from

an improved stress transfer from the PP matrix to GnPs with larger surface area and an extended crack propagation length at the interface. The greatest elongation was also observed with C300, implicating better dispersion with less agglomeration of fillers within the matrix. This was also confirmed with the SEM images as any deterioration of filler morphology was not detected with C300. Electrical conductivity was the only property that benefited from the large-sized GnPs. The percolation thresholds were 2.99, 3.66, and 5.05 vol% for H100, M25, and M5, respectively. This study clearly demonstrates that the physical dimensions of GnPs play an essential role in determining a variety of properties of PP composites, and hence the dimensions of GnPs should be carefully tailored to meet the particular property of interest for each application.

8.2   Recommendations

It is crucial that future work following this thesis will further develop conductive polymer nano-composites exhibiting high electrical conductivity with other properties of importance tailored for a particular field of applications. Below is the proposed future works for each stream of composite fabrication technique.

8.2.1   Polymer nano-composites fabricated via infiltration

It has been reported that when high aspect ratio fillers were combined with two-dimensional materials with a large diameter, a substantially improved electrical conductivity was observed with low percolation threshold [29]. This is due to the role of high aspect ratio fillers that serve as bridges connecting the large diameter materials. Moreover, it was demonstrated from this thesis that a filler matrix produced via freeze casting is oriented with a freezing direction. Therefore, it is necessary to determine both electrical and mechanical properties of composites with respect to the orientation of filler matrix. Specific suggestions are summarized as below:

- Combine GNRs with different flake size of GO and come up with the optimized compositional ratio to maximize the synergistic effects for obtaining the highest electrical conductivity under elongation. The GNRs will serve as inter-linking junctions between large-sized GO sheets and electrical conductivity can be considerably enhanced with a low percolation threshold.

- The freeze casting and porous area within the filler matrix are influenced by several factors including the oxidation state of GO solution, freezing rate and temperature. Thus, by controlling these factors, the dispersion of GNRs and the porosity of a filler matrix can be tailored to further increase electrical conductivity and its consistency under elongation.

- Explore the effects of filler orientation for electrical conductivity consistency. The influences of orientation on the mechanical properties also should be investigated by means of dynamic mechanical analysis or tensile strength testing.

8.2.2 Polymer nano-composites fabricated via compounding

This thesis illustrated that electrical and mechanical properties of composites are greatly influenced by the dimensions of GnPs, and it was challenging to enhance both properties simultaneously. It was found that the use of large-sized GnPs was promising for improved electrical conductivity with low percolation threshold, but the issue was the agglomeration and deterioration of filler morphology. To prevent large-sized GnPs from being compromised during compounding, it is recommended that the different processing techniques be employed and compared, or the processing conditions are further optimized to minimize the deterioration of filler morphology.

120

Moreover, similarly to the suggestions made for composites fabricated via infiltration, it should be worth to combine different grades of GnPs and find an optimized GnPs grades and their compositional ratio for both improved electrical and mechanical properties, simultaneously. Detailed recommendations are summarized as follows:

- To avoid the compromising of GnP-H100 fillers, the advanced compounding techniques should be developed and applied. One proposed method is to coat the PP particles with GnPs by dispersing them in an organic solvent with sonication and compress mould the evaporated mixture of the PP particles coated with GnPs [162].

- Combine various grades of GnPs and find out an ideal compositional ratio that can lead to both improved electrical and mechanical properties [163].

- Inferior improvement in mechanical property can be largely due to lack of interfacial bonding between fillers and polymer matrix. To improve the mechanical properties, the interfacial bonding must be enhanced through a technique that does not compromise electrical conductivity.

- The crystallites developed around the GnPs can have negative influences on forming percolating network. Finding a way to suppress crystallization around the GnPs would lead to enhanced percolation network with improved electrical conductivity.

- PP/GnPs composites have great potential to replace conventional bipolar plates in PEMFC. There are a number of requirements, such as electrical, mechanical, and barrier and corrosion properties, to be fulfilled for successful utilization, however. It would be advantageous to predict these properties by applying theoretical analysis and modeling work to find out ideal compositional contents and physical parameters of GnPs.

References

[1]   L. Rupprecht, Ed., *Conductive Polymers and Plastics in industrial applications*. Norwich: William Andrew Inc., 1999.

[2]   M. L. Clingerman, "Development and Modelling of Electrically Conductive Composite Materials," Michigan Technological University, 2001.

[3]   T. K. Das and S. Prusty, "Graphene-Based Polymer Composites and Their Applications," *Polym. Plast. Technol. Eng.*, vol. 52, no. 4, pp. 319–331, Mar. 2013.

[4]   B. Berkowitz and R. P. Ewing, "Percolation Theory and Network Modeling Applications in Soil Physics," *Surv. Geophys.*, vol. 19, pp. 23–72, 1998.

[5]   N. G. Sahoo, S. Rana, J. W. Cho, L. Li, and S. H. Chan, "Polymer nanocomposites based on functionalized carbon nanotubes," *Prog. Polym. Sci.*, vol. 35, pp. 837–867, Jul. 2010.

[6]   Z.-S. Wu, G. Zhou, L.-C. Yin, W. Ren, F. Li, and H.-M. Cheng, "Graphene/metal oxide composite electrode materials for energy storage," *Nano Energy*, vol. 1, pp. 107–131, Jan. 2012.

[7]   H. Kim, A. a. Abdala, and C. W. Macosko, "Graphene/Polymer Nanocomposites," *Macromolecules*, vol. 43, no. 16, pp. 6515–6530, Aug. 2010.

[8]   iPolycond Consortium. (2011). Introduction to Conductive Polymer Composites. Smithers Rapra Technology. Online version available at: http://app.knovel.com/hotlink/toc/id:kpICPC0009/introduction-conductive/introduction-conductive

[9]   V. Chabot, D. Higgins, A. Yu, X. Xiao, Z. Chen, and J. Zhang, "A review of graphene and graphene oxide sponge: material synthesis and applications to energy and the environment," *Energy Environ. Sci.*, vol. 7, no. 5, p. 1564, 2014.

[10]   Z. Chen, W. Ren, L. Gao, B. Liu, S. Pei, and H.-M. Cheng, "Three-dimensional flexible and conductive interconnected graphene networks grown by chemical vapour deposition.," *Nat. Mater.*, vol. 10, no. 6, pp. 424–428, 2011.

[11]   P. A. Fowler, J. M. Hughes, and R. M. Elias, "Biocomposites: technology, environmental credentials and market forces," *J. Sci. Food Agric.*, vol. 86, pp. 1781–1789, 2006.

[12]   H. G. Karian, Ed., *Handbook of polypropylene and polypropylene composites*. New York: Marcel Dekker, Inc., 2003.

[13]   F. De Paoli, "Measuring Polydimethylsiloxane (PDMS) Mechanical Properties using flat punch nanoindentation focusing on obtaining full contact," University of South Florida, 2015.

[14]   R. Chatchaidech, "Lubrication Forces in Polydimethylsiloxane (PDMS) melts," Virginia Polytechnic Institute and State University, 2011.

[15]   E. G. Rochow, "The Direct Synthesis of Organosilicon Compounds," *J. Am. Chem. Soc.*, vol. 67, no. 6, pp. 963–965, Jun. 1945.

[16]   G. C. Lisensky, D. J. Campbell, K. J. Beckman, C. E. Calderon, P. W. Doolan, R. M. Ottosen, and A. B. Ellis, "Replication and Compression of Surface Structures with Polydimethylsiloxane Elastomer," *J. Chem. Educ.*, vol. 76, no. 4, p. 537, Apr. 1999.

[17]   C. N. R. Rao, A. K. Sood, K. S. Subrahmanyam, and A. Govindaraj, "Graphene: The New Two-Dimensional Nanomaterial," *Angew. Chemie Int. Ed.*, vol. 48, pp. 7752–7777, Oct.

2009.

[18]   A. K. Geim and K. S. Novoselov, "The rise of graphene.," *Nat. Mater.*, vol. 6, pp. 183–191, 2007.

[19]   W. S. Hummers and R. E. Offeman, "Preparation of Graphitic Oxide," *J. Am. Chem. Soc*, vol. 80, p. 1339, 1958.

[20]   D. R. Dreyer, S. Park, C. W. Bielawski, and R. S. Ruoff, "The chemistry of graphene oxide.," *Chem. Soc. Rev.*, vol. 39, pp. 228–240, 2010.

[21]   S. Pei and H.-M. Cheng, "The reduction of graphene oxide," *Carbon*, vol. 50, pp. 3210–3228, Aug. 2012.

[22]   A. Hussein, S. Sarkar, and B. Kim, "Low Temperature Reduction of Graphene Oxide Using Hot-plate for Nanocomposites Applications," *J. Mater. Sci. Technol.*, vol. 32, pp. 411–418, 2016.

[23]   B. Ahmadi-Moghadam and F. Taheri, "Effect of processing parameters on the structure and multi-functional performance of epoxy/GNP-nanocomposites," *J. Mater. Sci.*, vol. 49, pp. 6180–6190, 2014.

[24]   R. Sengupta, M. Bhattacharya, S. Bandyopadhyay, and A. K. Bhowmick, "A review on the mechanical and electrical properties of graphite and modified graphite reinforced polymer composites," *Prog. Polym. Sci.*, vol. 36, pp. 638–670, 2011.

[25]   G. R. B. Michael D. Via, Julia A. King, Jason M. Keith, Ibrahim Miskioglu, Mark J. Cieslinski, Jonathan J. Anderson, "Tensile Modulus Modeling of Carbon Black/ Polycarbonate, Carbon Nanotube/Polycarbonate, and Exfoliated Graphite Nanoplatelet/Polycarbonate Composites," *J. Appl. Polym. Sci.*, vol. 124, pp. 2269–2277,

2012.

[26] B. Mayoral, E. Harkin-Jones, P. N. Khanam, M. A. AlMaadeed, M. Ouederni, A. R. Hamilton, and D. Sun, "Melt processing and characterisation of polyamide 6/graphene nanoplatelet composites," *RSC Adv.*, vol. 5, pp. 52395–52409, 2015.

[27] B. Kalantari, M. R. Mohaddes Mojtahedi, F. Sharif, and R. Semnani Rahbar, "Flow-induced crystallization of polypropylene in the presence of graphene nanoplatelets and relevant mechanical properties in nanocompsoite fibres," *Compos. Part A Appl. Sci. Manuf.*, vol. 76, pp. 203–214, 2015.

[28] A. Tiwari and M. Syväjärvi, Eds., *Graphene Materials Fundamentals and Emerging Applications*. Beverly, MA: Scrivener Publishing, 2015.

[29] D. Galpaya, M. Wang, M. Liu, N. Motta, E. Waclawik, and C. Yan, "Recent Advances in Fabrication and Characterization of Graphene-Polymer Nanocomposites," *Graphene*, vol. 1, pp. 30–49, 2012.

[30] A. Celzard, J. F. Marêché, and G. Furdin, "Modelling of exfoliated graphite," *Prog. Mater. Sci.*, vol. 50, pp. 93–179, 2005.

[31] G. Carotenuto, S. De Nicola, M. Palomba, D. Pullini, A. Horsewell, T. W. Hansen, and L. Nicolais, "Mechanical properties of low-density polyethylene filled by graphite nanoplatelets," *Nanotechnology*, vol. 23, p. 485705, Dec. 2012.

[32] M. Y. Han, B. Özyilmaz, Y. Zhang, and P. Kim, "Energy band-gap engineering of graphene nanoribbons," *Phys. Rev. Lett.*, vol. 98, p. 206805, 2007.

[33] X. Li, X. Wang, L. Zhang, S. Lee, and H. Dai, "Chemically Derived Ultramooth Graphene Nanoribbon Semiconductors," *Sci. Mag.*, vol. 319, no. 5867, pp. 1229–1232, 2008.

[34] S. S. Datta, D. R. Strachan, S. M. Khamis, and A. T. C. Johnson, "Crystallographic etching of few-layer graphene," *Nano Lett.*, vol. 8, no. 7, pp. 1912–1915, 2008.

[35] L. Jiao, L. Zhang, X. Wang, G. Diankov, and H. Dai, "Narrow graphene nanoribbons from carbon nanotubes," *Nature*, vol. 458, pp. 877–880, 2009.

[36] D. V. Kosynkin, A. L. Higginbotham, A. Sinitskii, J. R. Lomeda, A. Dimiev, B. K. Price, and J. M. Tour, "Longitudinal unzipping of carbon nanotubes to form graphene nanoribbons," *Nature*, vol. 458, pp. 872–876, 2009.

[37] A. G. Cano-Márquez, F. J. Rodríguez-Macías, J. Campos-Delgado, C. G. Espinosa-González, F. Tristán-López, D. Ramírez-González, D. A. Cullen, D. J. Smith, M. Terrones, and Y. I. Vega-Cantú, "Ex-MWNTs: Graphene Sheets and Ribbons Produced by Lithium Intercalation and Exfoliation of Carbon Nanotubes," *Nano Lett.*, vol. 9, no. 4, pp. 1527–1533, Apr. 2009.

[38] A. L. Elias, A. R. Botello-Méndez, D. Meneses-Rodríguez, V. J. González, D. Ramírez-González, L. Ci, E. Muñoz-Sandoval, P. M. Ajayan, H. Terrones, and M. Terrones, "Longitudinal cutting of pure and doped carbon nanotubes to form graphitic nanoribbons using metal clusters as nanoscalpels," *Nano Lett.*, vol. 10, pp. 366–372, 2010.

[39] J. Campos-Delgado, J. M. Romo-Herrera, X. Jia, D. A. Cullen, H. Muramatsu, Y. A. Kim, T. Hayashi, Z. Ren, D. J. Smith, Y. Okuno, T. Ohba, H. Kanoh, K. Kaneko, M. Endo, H. Terrones, M. S. Dresselhaus, and M. Terrones, "Bulk Production of a New Form of sp 2 Carbon: Crystalline Graphene Nanoribbons," *Nano Lett.*, vol. 8, no. 9, pp. 2773–2778, Sep. 2008.

[40] X. Yang, X. Dou, A. Rouhanipour, L. Zhi, H. J. Räder, and K. Müllen, "Two-dimensional

graphene nanoribbons," *J. Am. Chem. Soc.*, vol. 130, pp. 4216–4217, 2008.

[41]   S. Wolfe, C. F. Ingold, and R. U. Lemieux, "Oxidation of olefins by potassium permanganate. Mechanism of α.-ketol formation," *J. Am. Chem. Soc.*, vol. 103, pp. 938–939, Feb. 1981.

[42]   XG Science Inc, xGnP brand graphene nanoplatelets product information, http://xgscience.com (Last Acquired Aug 10, 2016).

[43]   W. Abdelwahed, G. Degobert, S. Stainmesse, and H. Fessi, "Freeze-drying of nanoparticles: Formulation, process and storage considerations☆," *Adv. Drug Deliv. Rev.*, vol. 58, no. 15, pp. 1688–1713, Dec. 2006.

[44]   W. Chen and L. Yan, "In situ self-assembly of mild chemical reduction graphene for three-dimensional architectures.," *Nanoscale*, vol. 3, pp. 3132–3137, 2011.

[45]   L. Qiu, J. Z. Liu, S. L. Y. Chang, Y. Wu, and D. Li, "Biomimetic superelastic graphene-based cellular monoliths," *Nat. Commun.*, vol. 3, p. 1241, Dec. 2012.

[46]   Z. S. Wu, A. Winter, L. Chen, Y. Sun, A. Turchanin, X. Feng, and K. Müllen, "Three-dimensional nitrogen and boron co-doped graphene for high-performance all-solid-state supercapacitors," *Adv. Mater.*, vol. 24, no. 37, pp. 5130–5135, 2012.

[47]   C. L. Yuxi Xu, Kaixuan Sheng and G. Shi, "Self-Assembled Graphene Hydrogel," *ACS Nano*, vol. 4, no. 7, pp. 4324–4330, 2010.

[48]   S. Ye, J. Feng, and P. Wu, "Highly elastic graphene oxide–epoxy composite aerogels via simple freeze-drying and subsequent routine curing," *J. Mater. Chem. A*, vol. 1, pp. 3495–3502, 2013.

[49]   Y. Zhao, J. Liu, Y. Hu, H. Cheng, C. Hu, C. Jiang, L. Jiang, A. Cao, and L. Qu, "Highly

Compression-Tolerant Supercapacitor Based on Polypyrrole-mediated Graphene Foam Electrodes," *Adv. Mater.*, vol. 25, pp. 591–595, Jan. 2013.

[50] B. Xu, Y. Qiao, T. Park, M. Tak, Q. Zhou, and X. Chen, "A conceptual thermal actuation system driven by interface tension of nanofluids," *Energy Environ. Sci.*, vol. 4, pp. 3632–3639, 2011.

[51] L. Liu, J. Zhao, C.-Y. Yin, P. J. Culligan, and X. Chen, "Mechanisms of water infiltration into conical hydrophobic nanopores," *Phys. Chem. Chem. Phys.*, vol. 11, p. 6520, 2009.

[52] Y. Qiao, V. K. Punyamurtula, A. Han, X. Kong, and F. B. Surani, "Temperature dependence of working pressure of a nanoporous liquid spring," *Appl. Phys. Lett.*, vol. 89, p. 251905, Dec. 2006.

[53] J. Zhao, L. Liu, P. J. Culligan, and X. Chen, "Thermal effect on the dynamic infiltration of water into single-walled carbon nanotubes," *Phys. Rev. E*, vol. 80, p. 61206, Dec. 2009.

[54] D. R. Ceratti, M. Faustini, C. Sinturel, M. Vayer, V. Dahirel, M. Jardat, and D. Grosso, "Critical effect of pore characteristics on capillary infiltration in mesoporous films," *Nanoscale*, vol. 7, pp. 5371–5382, 2015.

[55] M. R. Abusrea and K. Arakawa, "Improvement of an adhesive joint constructed from carbon fiber-reinforced plastic and dry carbon fiber laminates," *Compos. Part B Eng.*, vol. 97, pp. 368–373, Jul. 2016.

[56] R. J. Cano, S. Ghose, K. A. Watson, P. B. Chunchu, B. J. Jensen, and J. W. Connell, "Processing and Properties of Vacuum Assisted Resin Transfer Molded Phenylethynyl Terminated Imide Composites," Hampton, VA, 2012. available online at https://ntrs.nasa.gov/search.jsp?R=20120009211.

[57]   B. W. Grimsley, "Characterization of the Vacuum Assisted Resin Transfer Molding Process for Fabrication of Aerospace Composites," Virginia Polytechnic Institute and State University, 2005.

[58]   C. I. Chung, *Extrusion of Polymers: Theory and Practice*, 2nd Ed. Cincinnati: Hanser Publications, 2011.

[59]   M. N. Subrmanian, *Introduction to Polymer Compounding: Machinery and Technology, Volume 2*. Shrewsbury: Smithers Rapra Technology Ltd, 2015.

[60]   K. Kohlgrüber, Ed., *Co-Rotating Twin-Screw Extruders: Fundamentals, Technology, and Applications*. Cincinnati: Hanser Gardner Publications, Inc, 2008.

[61]   J. Breitenbach, "Melt extrusion: from process to drug delivery technology," *Eur. J. Pharm. Biopharm.*, vol. 54, pp. 107–117, 2002.

[62]   Z. Tadmor and C. G. Gogos, *Principles of Polymer Processing*, 2nd editio. Hoboken, New Jersey: John Wiley & Sons, Inc, 2006.

[63]   D. Stauffer and A. Aharony, *Introduction to percolation theory*, 2nd ed. Philadelphia: Taylor and Francis, 2003.

[64]   S. Kirkpatrick, "Percolation and Conduction," *Rev. Mod. Phys.*, vol. 45, pp. 574–588, 1973.

[65]   R. Zallen, *The physics of amorphous solids*. Blacksburg, Virginia: John Wiley & Sons, Inc, 1998.

[66]   E. P. Mamunya, V. V. Davidenko, and E. V. Lebedev, "Effect of polymer-filler interface interactions on percolation conductivity of thermoplastics filled with carbon black," *Compos. Interfaces*, vol. 4, no. 4, pp. 169–176, Jan. 1996.

[67] F. M. Fowkes, "Attractive forces at interface," *Ind. Eng. Chem.*, vol. 56, pp. 40–52, Dec. 1964.

[68] F. Lux, "Models proposed to explain the electrical conductivity of mixtures made of conductive and insulating materials," *J. Mater. Sci.*, vol. 28, pp. 285–301, 1993.

[69] Z. Chen, C. Xu, C. Ma, W. Ren, and H. M. Cheng, "Lightweight and flexible graphene foam composites for high-performance electromagnetic interference shielding," *Adv. Mater.*, vol. 25, no. 9, pp. 1296–1300, 2013.

[70] E. Planes, L. Flandin, and N. Alberola, "Polymer composites bipolar plates for PEMFCs," *Energy Procedia*, vol. 20, pp. 311–323, 2012.

[71] F. G. Boyaci San and G. Tekin, "A review of thermoplastic composites for bipolar plate applications," *Int. J. Energy Res.*, vol. 37, pp. 283–309, Mar. 2013.

[72] R. Yeetsorn, "Development of Electrically Conductive Thermoplastic Composites for Bipolar Plate Application in Polymer Electrolyte Membrane Fuel Cell," University of Waterloo, 2010.

[73] S.-L. Zhang, *Raman Spectroscopy and its application in nanostructures*. West Sussex: John Wiley & Sons, Ltd, 2012.

[74] I. Childres, L. Jauregui, W. Park, H. Cao, and Y. Chen, "Raman Spectroscopy of Graphene and Related Materials," in *New Developments in Photon and Materials Research*, J. I. Jang, Ed. Nova Science Publishers, Inc., 2013, pp. 1–20.

[75] D. K. Schroder, *Semiconductor material and device characterization*. New Jersey: A John Wiley and Sons, Inc, 2006.

[76] J. W. Kim, N. H. Kim, T. Kuilla, T. J. Kim, K. Y. Rhee, and J. H. Lee, "Synergy effects of

hybrid carbon system on properties of composite bipolar plates for fuel cells," *J. Power Sources*, vol. 195, pp. 5474–5480, Sep. 2010.

[77]   C. a Mitchell and R. Krishnamoorti, "Dispersion of Single-Walled Carbon Nanotubes in Poly(ε-caprolactone)," *Macromolecules*, vol. 40, pp. 1538–1545, Mar. 2007.

[78]   E. Bekyarova, E. T. Thostenson, A. Yu, H. Kim, J. Gao, J. Tang, H. T. Hahn, T.-W. Chou, M. E. Itkis, and R. C. Haddon, "Multiscale Carbon Nanotube−Carbon Fiber Reinforcement for Advanced Epoxy Composites," *Langmuir*, vol. 23, pp. 3970–3974, Mar. 2007.

[79]   R. Sen, B. Zhao, D. Perea, M. E. Itkis, H. Hu, J. Love, E. Bekyarova, and R. C. Haddon, "Preparation of single-walled carbon nanotube reinforced polystyrene and polyurethane nanofibers and membranes by electrospinning," *Nano Lett.*, vol. 4, no. 3, pp. 459–464, 2004.

[80]   V. Chabot, B. Kim, B. Sloper, C. Tzoganakis, and A. Yu, "High yield production and purification of few layer graphene by gum arabic assisted physical sonication.," *Sci. Rep.*, vol. 3, p. 1378, 2013.

[81]   K. Zhang, Y. Zhang, and S. Wang, "Effectively decoupling electrical and thermal conductivity of polymer composites," *Carbon*, vol. 65, pp. 105–111, 2013.

[82]   T. Kuilla, S. Bhadra, D. Yao, N. H. Kim, S. Bose, and J. H. Lee, "Recent advances in graphene based polymer composites," *Prog. Polym. Sci.*, vol. 35, pp. 1350–1375, Nov. 2010.

[83]   K. H. Kim, M. Vural, and M. F. Islam, "Single-Walled Carbon Nanotube Aerogel-Based Elastic Conductors," *Adv. Mater.*, vol. 23, pp. 2865–2869, Jul. 2011.

[84] G. Tang, Z. G. Jiang, X. Li, H. Bin Zhang, A. Dasari, and Z. Z. Yu, "Three dimensional graphene aerogels and their electrically conductive composites," *Carbon*, vol. 77, pp. 592–599, 2014.

[85] M. Chen, T. Tao, L. Zhang, W. Gao, and C. Li, "Highly conductive and stretchable polymer composites based on graphene/MWCNT network," *Chem. Commun.*, vol. 49, pp. 1612–1614, 2013.

[86] A. Yu, I. Roes, A. Davies, and Z. Chen, "Ultrathin, transparent, and flexible graphene films for supercapacitor application," *Appl. Phys. Lett.*, vol. 96, p. 253105, Jun. 2010.

[87] W. Ahn, H. S. Song, S.-H. Park, K.-B. Kim, K.-H. Shin, S. N. Lim, and S.-H. Yeon, "Morphology-controlled graphene nanosheets as anode material for lithium-ion batteries," *Electrochim. Acta*, vol. 132, pp. 172–179, Jun. 2014.

[88] H. J. Shin, K. K. Kim, A. Benayad, S. M. Yoon, H. K. Park, I. S. Jung, M. H. Jin, H. K. Jeong, J. M. Kim, J. Y. Choi, and Y. H. Lee, "Efficient Reduction of Graphite Oxide by Sodium Borohydride and Its Effect on Electrical Conductance," *Adv. Funct. Mater.*, vol. 19, pp. 1987–1992, 2009.

[89] A. Jorio, "Raman Spectroscopy in Graphene-Based Systems: Prototypes for Nanoscience and Nanometrology," *ISRN Nanotechnol.*, vol. 2012, pp. 1–16, 2012.

[90] S. Reich and C. Thomsen, "Raman spectroscopy of graphite," *Philos. Trans. R. Soc. A*, vol. 362, pp. 2271–2288, Nov. 2004.

[91] X. Díez-Betriu, S. Álvarez-García, C. Botas, P. Álvarez, J. Sánchez-Marcos, C. Prieto, R. Menéndez, and A. de Andrés, "Raman spectroscopy for the study of reduction mechanisms and optimization of conductivity in graphene oxide thin films," *J. Mater.*

Chem. C, vol. 1, pp. 6905–6912, 2013.

[92]   F. Tuinstra and J. L. Koenig, "Raman Spectrum of Graphite," *J. Chem. Phys.*, vol. 53, pp. 1126–1130, Aug. 1970.

[93]   Y. Zhang, C. J. Sheehan, J. Zhai, G. Zou, H. Luo, J. Xiong, Y. T. Zhu, and Q. X. Jia, "Polymer-Embedded Carbon Nanotube Ribbons for Stretchable Conductors," *Adv. Mater.*, vol. 22, pp. 3027–3031, Jun. 2010.

[94]   W. Bauhofer and J. Z. Kovacs, "A review and analysis of electrical percolation in carbon nanotube polymer composites," *Compos. Sci. Technol.*, vol. 69, pp. 1486–1498, Aug. 2009.

[95]   J. Hicks, A. Behnam, and A. Ural, "A computational study of tunneling-percolation electrical transport in graphene-based nanocomposites," *Appl. Phys. Lett.*, vol. 95, p. 213103, Nov. 2009.

[96]   L. Jiao, L. Zhang, L. Ding, J. Liu, and H. Dai, "Aligned graphene nanoribbons and crossbars from unzipped carbon nanotubes," *Nano Res.*, vol. 3, pp. 387–394, Jun. 2010.

[97]   S. Stankovich, D. a. Dikin, R. D. Piner, K. a. Kohlhaas, A. Kleinhammes, Y. Jia, Y. Wu, S. T. Nguyen, and R. S. Ruoff, "Synthesis of graphene-based nanosheets via chemical reduction of exfoliated graphite oxide," *Carbon*, vol. 45, pp. 1558–1565, Jun. 2007.

[98]   A. L. Higginbotham, D. V. Kosynkin, A. Sinitskii, Z. Sun, and J. M. Tour, "Lower-Defect Graphene Oxide Nanoribbons from Multiwalled Carbon Nanotubes," *ACS Nano*, vol. 4, pp. 2059–2069, Apr. 2010.

[99]   W. L. Li, K. Lu, and J. Y. Walz, "Freeze casting of porous materials: review of critical factors in microstructure evolution," *Int. Mater. Rev.*, vol. 57, pp. 37–60, Jan. 2012.

[100] S. Deville, "Freeze-Casting of Porous Ceramics: A Review of Current Achievements and Issues," *Adv. Eng. Mater.*, vol. 10, pp. 155–169, Mar. 2008.

[101] S. Park and R. S. Ruoff, "Chemical methods for the production of graphenes," *Nat. Nanotechnol.*, vol. 4, pp. 217–224, Apr. 2009.

[102] D. Hofmann, K.-A. Wartig, R. Thomann, B. Dittrich, B. Schartel, and R. Mülhaupt, "Functionalized Graphene and Carbon Materials as Additives for Melt-Extruded Flame Retardant Polypropylene," *Macromol. Mater. Eng.*, vol. 298, pp. 1322–1334, Dec. 2013.

[103] K. Kalaitzidou, H. Fukushima, H. Miyagawa, and L. T. Drzal, "Flexural and tensile moduli of polypropylene nanocomposites and comparison of experimental data to Halpin-Tsai and Tandon-Weng models," *Polym. Eng. Sci.*, vol. 47, pp. 1796–1803, Nov. 2007.

[104] B. Dittrich, K.-A. Wartig, D. Hofmann, R. Mülhaupt, and B. Schartel, "Flame retardancy through carbon nanomaterials: Carbon black, multiwall nanotubes, expanded graphite, multi-layer graphene and graphene in polypropylene," *Polym. Degrad. Stab.*, vol. 98, pp. 1495–1505, Aug. 2013.

[105] C. I. Idumah and A. Hassan, "Effect of exfoliated graphite nanoplatelets on thermal and heat deflection properties of kenaf polypropylene hybrid nanocomposites," *J. Polym. Eng.*, vol. 36, pp. 877–889, Jan. 2016.

[106] M. H. Al-Saleh, "Electrical, EMI shielding and tensile properties of PP/PE blends filled with GNP:CNT hybrid nanofiller," *Synth. Met.*, vol. 217, pp. 322–330, Jul. 2016.

[107] S. Zhong, Z. Zhou, K. Zhang, Y. Shi, Y. Chen, X.-D. Chen, J.-B. Zeng, and M. Wang, "Formation of thermally conductive networks in isotactic polypropylene/hexagonal boron nitride composites via 'Bridge Effect' of multi-wall carbon nanotubes and graphene

nanoplatelets," *RSC Adv.*, vol. 6, pp. 98571–98580, 2016.

[108] D. G. Papageorgiou, I. A. Kinloch, and R. J. Young, "Hybrid multifunctional
graphene/glass-fibre polypropylene composites," *Compos. Sci. Technol.*, vol. 137, pp. 44–
51, Dec. 2016.

[109] A. P. Bafana, X. Yan, X. Wei, M. Patel, Z. Guo, S. Wei, and E. K. Wujcik,
"Polypropylene nanocomposites reinforced with low weight percent graphene
nanoplatelets," *Compos. Part B Eng.*, vol. 109, pp. 101–107, Jan. 2017.

[110] J. Liang, Q. Du, G. C. Tsui, and C. Tang, "Tensile properties of graphene nano-platelets
reinforced polypropylene composites," *Compos. Part B Eng.*, vol. 95, pp. 166–171, Jun.
2016.

[111] S. R. Ahmad, C. Xue, and R. J. Young, "The mechanisms of reinforcement of
polypropylene by graphene nanoplatelets," *Mater. Sci. Eng. B*, vol. 216, pp. 2–9, Feb.
2017.

[112] G. Luo, W. Li, W. Liang, G. Liu, Y. Ma, Y. Niu, and G. Li, "Coupling effects of glass
fiber treatment and matrix modification on the interfacial microstructures and the
enhanced mechanical properties of glass fiber/polypropylene composites," *Compos. Part
B Eng.*, vol. 111, pp. 190–199, Feb. 2017.

[113] E. M. do Nascimento, D. Eiras, and L. A. Pessan, "Effect of thermal treatment on impact
resistance and mechanical properties of polypropylene/calcium carbonate nanocomposites,"
Compos. Part B Eng., vol. 91, pp. 228–234, Apr. 2016.

[114] A. Patti, P. Russo, D. Acierno, and S. Acierno, "The effect of filler functionalization on
dispersion and thermal conductivity of polypropylene/multi wall carbon nanotubes

composites," *Compos. Part B Eng.*, vol. 94, pp. 350–359, Jun. 2016.

[115] P. I. Gonzalez-Chi, O. Rodríguez-Uicab, C. Martin-Barrera, J. Uribe-Calderon, G. Canché-Escamilla, M. Yazdani-Pedram, A. May-Pat, and F. Avilés, "Influence of aramid fiber treatment and carbon nanotubes on the interfacial strength of polypropylene hierarchical composites," *Compos. Part B Eng.*, vol. 122, pp. 16–22, Aug. 2017.

[116] J. a. King, M. D. Via, F. a. Morrison, K. R. Wiese, E. a. Beach, M. J. Cieslinski, and G. R. Bogucki, "Characterization of exfoliated graphite nanoplatelets/polycarbonate composites: electrical and thermal conductivity, and tensile, flexural, and rheological properties," *J. Compos. Mater.*, vol. 46, pp. 1029–1039, May 2012.

[117] G. Gedler, M. Antunes, and J. I. Velasco, "Low density polycarbonate–graphene nanocomposite foams produced by supercritical carbon dioxide two-step foaming. Thermal stability," *Compos. Part B Eng.*, vol. 92, pp. 299–306, May 2016.

[118] M. Ioniţă, G. M. Vlăsceanu, A. A. Watzlawek, S. I. Voicu, J. S. Burns, and H. Iovu, "Graphene and functionalized graphene: Extraordinary prospects for nanobiocomposite materials," *Compos. Part B Eng.*, vol. 121, pp. 34–57, Jul. 2017.

[119] Y.-H. Zhao, Y.-F. Zhang, S.-L. Bai, and X.-W. Yuan, "Carbon fibre/graphene foam/polymer composites with enhanced mechanical and thermal properties," *Compos. Part B Eng.*, vol. 94, pp. 102–108, Jun. 2016.

[120] J.-H. Lin, Z.-I. Lin, Y.-J. Pan, C.-L. Huang, C.-K. Chen, and C.-W. Lou, "Polymer composites made of multi-walled carbon nanotubes and graphene nano-sheets: Effects of sandwich structures on their electromagnetic interference shielding effectiveness," *Compos. Part B Eng.*, vol. 89, pp. 424–431, Mar. 2016.

[121] M. O. Khan, S. N. Leung, E. Chan, H. E. Naguib, F. Dawson, and V. Adinkrah, "Effects of microsized and nanosized carbon fillers on the thermal and electrical properties of polyphenylene sulfide based composites," *Polym. Eng. Sci.*, vol. 53, pp. 2398–2406, Nov. 2013.

[122] B. Galindo, A. Benedito, E. Gimenez, and V. Compañ, "Comparative study between the microwave heating efficiency of carbon nanotubes versus multilayer graphene in polypropylene nanocomposites," *Compos. Part B Eng.*, vol. 98, pp. 330–338, Aug. 2016.

[123] K. Kalaitzidou, H. Fukushima, and L. T. Drzal, "Mechanical properties and morphological characterization of exfoliated graphite–polypropylene nanocomposites," *Compos. Part A Appl. Sci. Manuf.*, vol. 38, pp. 1675–1682, Jul. 2007.

[124] E. V. Kuvardina, L. A. Novokshonova, S. M. Lomakin, S. A. Timan, and I. A. Tchmutin, "Effect of the graphite nanoplatelet size on the mechanical, thermal, and electrical properties of polypropylene/exfoliated graphite nanocomposites," *J. Appl. Polym. Sci.*, vol. 128, pp. 1417–1424, 2013.

[125] K. Kalaitzidou, H. Fukushima, and L. T. Drzal, "Multifunctional polypropylene composites produced by incorporation of exfoliated graphite nanoplatelets," *Carbon*, vol. 45, pp. 1446–1452, Jun. 2007.

[126] R. Dweiri and J. Sahari, "Electrical properties of carbon-based polypropylene composites for bipolar plates in polymer electrolyte membrane fuel cell (PEMFC)," *J. Power Sources*, vol. 171, pp. 424–432, Sep. 2007.

[127] Goonvean Fibres Ltd, HM20/70P product data sheet, http://www.goonveanfibres.com (Last Acquired Aug 10, 2015).

[128] A.S. T. M. (ASTM). D 1238-13. Standard test method for melt flow rates of thermodynamics by extrusion plastometer. West Conshohocken, PA: ASTM International; 2017. www.astm.org.

[129] A.S. T. M. (ASTM). D 790-03. Standard test method for flexural properties of unreinforced and reinforced Plastics and electrical insulating materials. West Conshohocken, PA: ASTM International; 2015. www.astm.org.

[130] A.S. T. M. (ASTM). D 638-14. Standard test method for tensile properties of Plastics. West Conshohocken, PA: ASTM International; 2015. www.astm.org.

[131] S. Zhao, F. Chen, Y. Huang, J.-Y. Dong, and C. C. Han, "Crystallization behaviors in the isotactic polypropylene/graphene composites," *Polymer*, vol. 55, pp. 4125–4135, Aug. 2014.

[132] X. Wei, D. Li, W. Jiang, Z. Gu, X. Wang, Z. Zhang, and Z. Sun, "3D Printable Graphene Composite," *Sci. Rep.*, vol. 5, p. 11181, Sep. 2015.

[133] A. V. Raghu, Y. R. Lee, H. M. Jeong, and C. M. Shin, "Preparation and Physical Properties of Waterborne Polyurethane/Functionalized Graphene Sheet Nanocomposites," *Macromol. Chem. Phys.*, vol. 209, pp. 2487–2493, Dec. 2008.

[134] Y. R. Lee, A. V. Raghu, H. M. Jeong, and B. K. Kim, "Properties of Waterborne Polyurethane/Functionalized Graphene Sheet Nanocomposites Prepared by an in situ Method," *Macromol. Chem. Phys.*, vol. 210, pp. 1247–1254, Aug. 2009.

[135] S. Kim, I. Do, and L. T. Drzal, "Multifunctional xGnP/LLDPE Nanocomposites Prepared by Solution Compounding Using Various Screw Rotating Systems," *Macromol. Mater. Eng.*, vol. 294, pp. 196–205, Mar. 2009.

[136] J. Yang, Y. Huang, Y. Lv, P. Zhao, Q. Yang, and G. Li, "The intrinsic thermal-oxidative stabilization effect of chemically reduced graphene oxide on polypropylene," *J. Mater. Chem. A*, vol. 1, pp. 11184–11191, 2013.

[137] S. Thomas and G. E. Zaikov, Eds., *Polymer nanocomposite research advances*. New York: Nova Science Publishers, Inc., 2008.

[138] K. Kalaitzidou, H. Fukushima, P. Askeland, and L. T. Drzal, "The nucleating effect of exfoliated graphite nanoplatelets and their influence on the crystal structure and electrical conductivity of polypropylene nanocomposites," *J. Mater. Sci.*, vol. 43, pp. 2895–2907, Apr. 2008.

[139] M. A. Milani, R. Quijada, N. R. S. Basso, A. P. Graebin, and G. B. Galland, "Influence of the graphite type on the synthesis of polypropylene/graphene nanocomposites," *J. Polym. Sci. Part A Polym. Chem.*, vol. 50, pp. 3598–3605, Sep. 2012.

[140] D. Pedrazzoli, A. Pegoretti, and K. Kalaitzidou, "Understanding the effect of silica nanoparticles and exfoliated graphite nanoplatelets on the crystallization behavior of isotactic polypropylene," *Polym. Eng. Sci.*, vol. 55, pp. 672–680, Mar. 2015.

[141] H. Wu, B. Rook, and L. T. Drzal, "Dispersion optimization of exfoliated graphene nanoplatelet in polyetherimide nanocomposites: Extrusion, precoating, and solid state ball milling," *Polym. Compos.*, vol. 34, pp. 426–432, Mar. 2013.

[142] I. M. Inuwa, A. Hassan, S. A. Samsudin, M. H. Mohamad Kassim, and M. Jawaid, "Mechanical and thermal properties of exfoliated graphite nanoplatelets reinforced polyethylene terephthalate/polypropylene composites," *Polym. Compos.*, vol. 35, pp. 2029–2035, Oct. 2014.

[143] J. Liang, Y. Huang, L. Zhang, Y. Wang, Y. Ma, T. Guo, and Y. Chen, "Molecular-Level Dispersion of Graphene into Poly(vinyl alcohol) and Effective Reinforcement of their Nanocomposites," *Adv. Funct. Mater.*, vol. 19, pp. 2297–2302, Jul. 2009.

[144] J. A. King, D. R. Klimek, I. Miskioglu, and G. M. Odegard, "Mechanical properties of graphene nanoplatelet/epoxy composites," *J. Compos. Mater.*, vol. 49, pp. 659–668, Mar. 2015.

[145] S. C. Tjong, "Polymer Composites with Carbonaceous Nanofillers: Electrical Properties and Applications," *J. Nanosci. Nanotechnol.*, vol. 14, pp. 1154–1168, Sep. 2012.

[146] Y. She, G. Chen, and D. Wu, "Fabrication of polyethylene/graphite nanocomposite from modified expanded graphite," *Polym. Int.*, vol. 56, pp. 679–685, May 2007.

[147] H. Park, K. Kalaitzidou, H. Fukushima, L. Drzal. Exfolaited graphite nanoplatelet (xGnP)/polypropylene nanocomposites. Spe Automotive and Composites Divisions - 7th Annual Automotive Composites Conference and Exhibition, Acce 2007 - Driving Performance and Productivity. 1:314-322

[148] Y. F. Zhao, M. Xiao, S. J. Wang, X. C. Ge, and Y. Z. Meng, "Preparation and properties of electrically conductive PPS/expanded graphite nanocomposites," *Compos. Sci. Technol.*, vol. 67, pp. 2528–2534, Sep. 2007.

[149] Y. S. Jun, S. Sy, W. Ahn, H. Zarrin, L. Rasen, R. Tjandra, B. M. Amoli, B. Zhao, G. Chiu, and A. Yu, "Highly conductive interconnected graphene foam based polymer composite," *Carbon*, vol. 95, pp. 653–658, 2015.

[150] E. Logakis, E. Pollatos, C. Pandis, V. Peoglos, I. Zuburtikudis, C. G. Delides, A. Vatalis, M. Gjoka, E. Syskakis, K. Viras, and P. Pissis, "Structure–property relationships in

isotactic polypropylene/multi-walled carbon nanotubes nanocomposites," *Compos. Sci. Technol.*, vol. 70, pp. 328–335, Feb. 2010.

[151] S. Chunhui, P. Mu, and Y. Runzhang, "The effect of particle size gradation of conductive fillers on the conductivity and the flexural strength of composite bipolar plate," *Int. J. Hydrogen Energy*, vol. 33, pp. 1035–1039, Feb. 2008.

[152] W. Xiao, P. Wu, and J. Feng, "Effect of β-nucleating agents on crystallization and melting behavior of isotactic polypropylene," *J. Appl. Polym. Sci.*, vol. 108, pp. 3370–3379, Jun. 2008.

[153] E. Ferrage, F. Martin, A. Boudet, S. Petit, G. Fourty, F. Jouffret, P. Micoud, P. De Parseval, S. Salvi, C. Bourgerette, J. Ferret, Y. Saint-Gerard, S. Buratto, and J. P. Fortune, "Talc as nucleating agent of polypropylene: morphology induced by lamellar particles addition and interface mineral-matrix modelization," *J. Mater. Sci.*, vol. 37, pp. 1561–1573, 2002.

[154] L. Valentini, J. Biagiotti, M. A. Lopez-Manchado, S. Santucci, and J. M. Kenny, "Effects of Carbon Nanotubes on the Crystallization Behavior of Polypropylene," *Polym. Eng. Sci.*, vol. 44, pp. 303–311, 2004.

[155] T. A. Huy, R. Adhikari, T. Lüpke, S. Henning, and G. H. Michler, "Molecular deformation mechanisms of isotactic polypropylene in α- and β-crystal forms by FTIR spectroscopy," *J. Polym. Sci. Part B Polym. Phys.*, vol. 42, pp. 4478–4488, Dec. 2004.

[156] K. Kalaitzidou, "Exfoliated graphite nanoplatelets as reinforcement for multifunctional polypropylene nanocomposites," Michigan State University, 2006.

[157] S. Fu, X. Feng, B. Lauke, and Y. Mai, "Effects of particle size, particle/matrix interface

adhesion and particle loading on mechanical properties of particulate–polymer composites," *Compos. Part B Eng.*, vol. 39, pp. 933–961, Sep. 2008.

[158] J. R. Greer, W. C. Oliver, and W. D. Nix, "Size dependence of mechanical properties of gold at the micron scale in the absence of strain gradients," *Acta Mater.*, vol. 53, pp. 1821–1830, Apr. 2005.

[159] M. Cadek, J. N. Coleman, K. P. Ryan, V. Nicolosi, G. Bister, A. Fonseca, J. B. Nagy, K. Szostak, F. Béguin, and W. J. Blau, "Reinforcement of Polymers with Carbon Nanotubes: The Role of Nanotube Surface Area," *Nano Lett.*, vol. 4, pp. 353–356, Feb. 2004.

[160] P. Calvert, "Nanotube composites: A recipe for strength," *Nature*, vol. 399, pp. 210–211, 1999.

[161] X. Jiang and L. T. Drzal, "Reduction in percolation threshold of injection molded high-density polyethylene/exfoliated graphene nanoplatelets composites by solid state ball milling and solid state shear pulverization," *J. Appl. Polym. Sci.*, vol. 124, pp. 525–535, Apr. 2012.

[162] K. Kalaitzidou, H. Fukushima, and L. T. Drzal, "A new compounding method for exfoliated graphite–polypropylene nanocomposites with enhanced flexural properties and lower percolation threshold," *Compos. Sci. Technol.*, vol. 67, pp. 2045–2051, Aug. 2007.

[163] X. Jiang and L. T. Drzal, "Exploring the potential of exfoliated graphene nanoplatelets as the conductive filler in polymeric nanocomposites for bipolar plates," *J. Power Sources*, vol. 218, pp. 297–306, Nov. 2012.

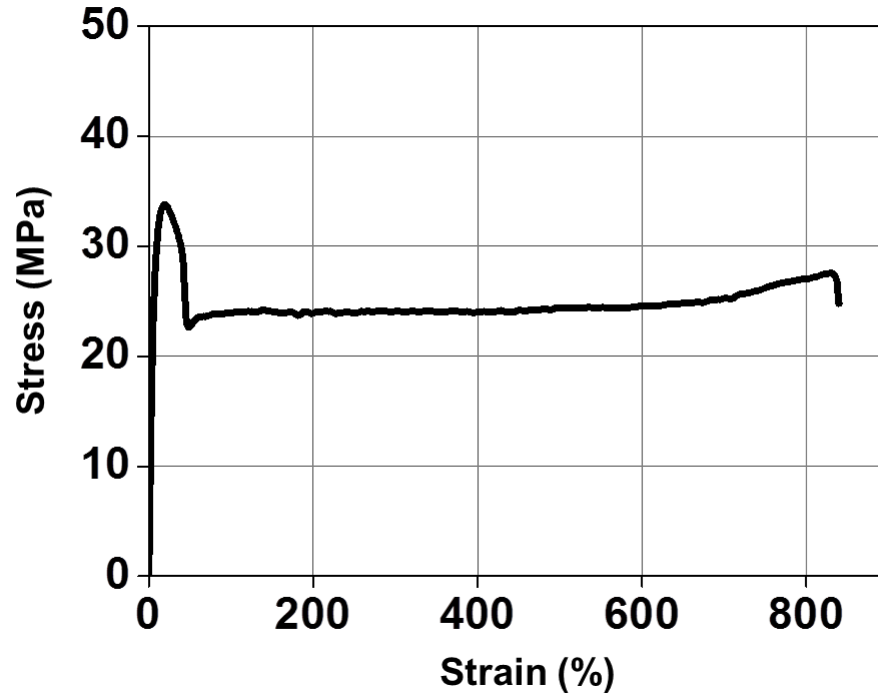# Appendix A

Figure A-1. The SS curve of neat PP

Figure A-2. The crystallization thermograms of PP composites incorporated with (a)H100, (b)M25, (c)M5, and (d)C300, respectively.
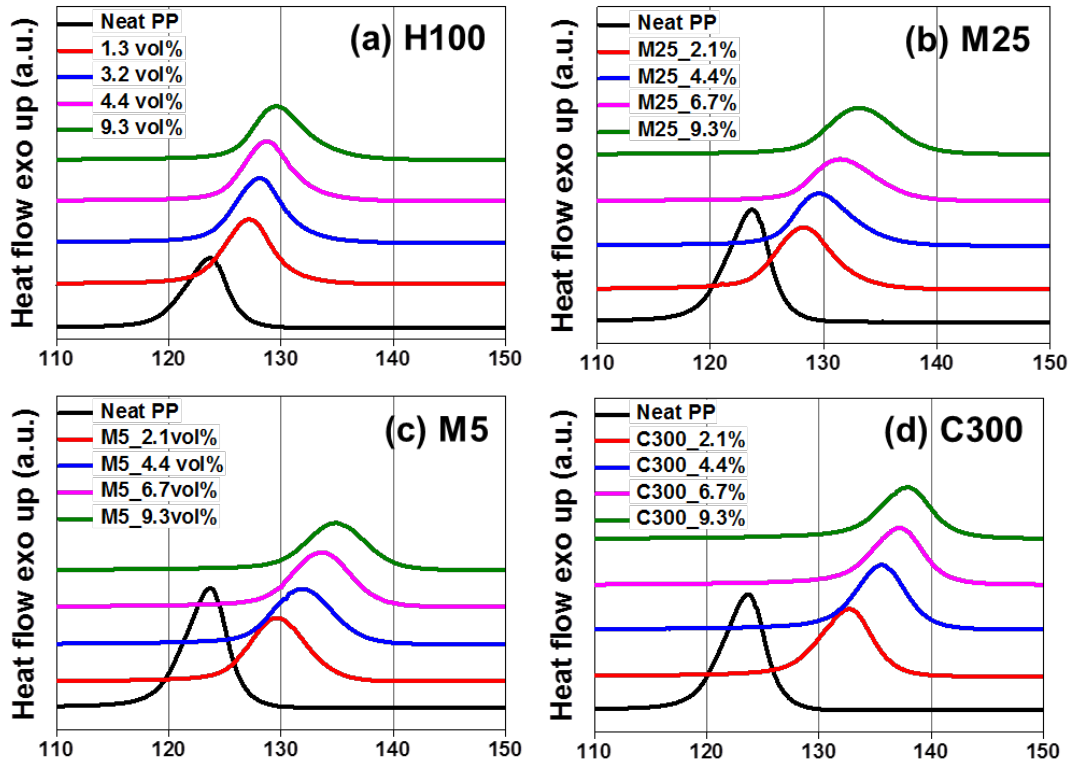
Figure A-3. The melting thermograms of PP composites incorporated with (a) H100, (b) M25, (c) M5, and (d) C300, respectively.
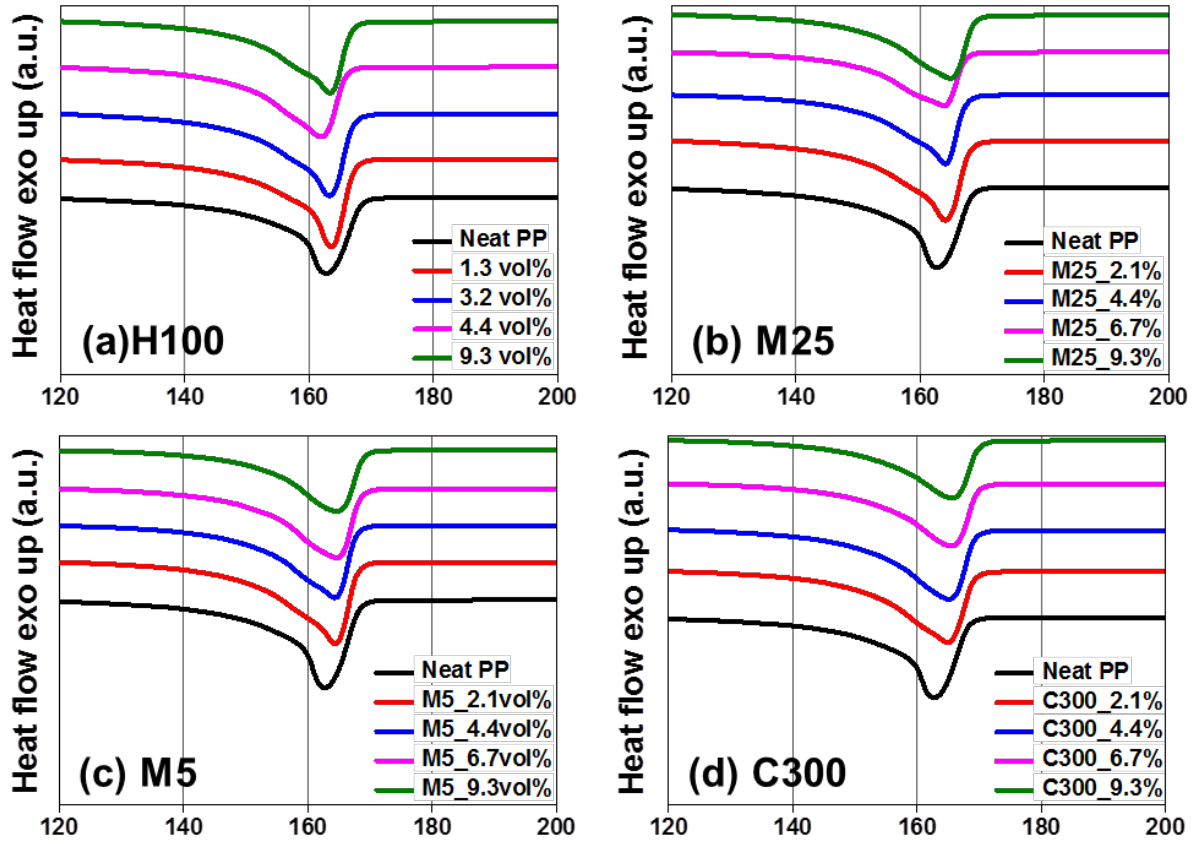
Figure A-4. The melting thermograms of PP/GnPs composites with a ramping rate of (a) 2°C/min, (b) 10°C/min, and (c) 20°C/min, respectively. Since the slight bimodal patterns are only visible when GnPs are added, this is more likely to be induced by incorporating GnPs. If the induction effect of GnPs is significant, the bimodal patterns should be clearer with a ramping rate of 2°C/min since a sufficient time is provided for the growth of crystals. However, the appearance of β crystals was not observed with a ramping rate of 2°C/min. This indicates that the induction effect of GnPs for β crystals is not significant, and the contents of β crystals are minimal.

146

Figure A-5. The variation of tensile strength and Young's modulus of PP composites incorporated with (a) H100, (b) M25, (c) M5, and (d) C300.
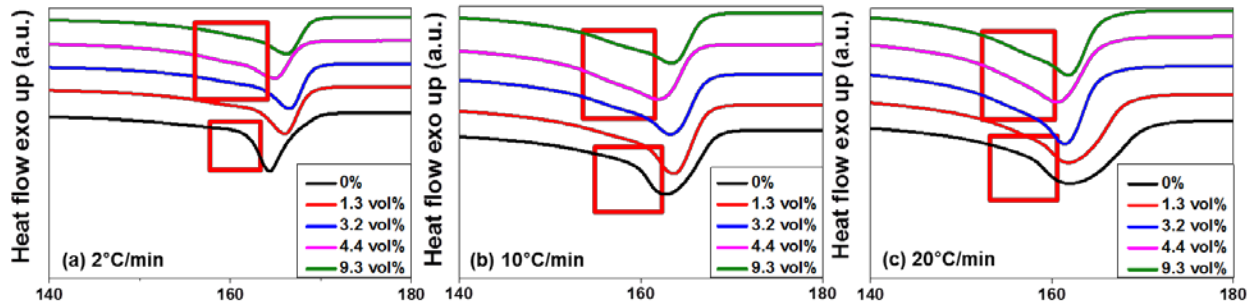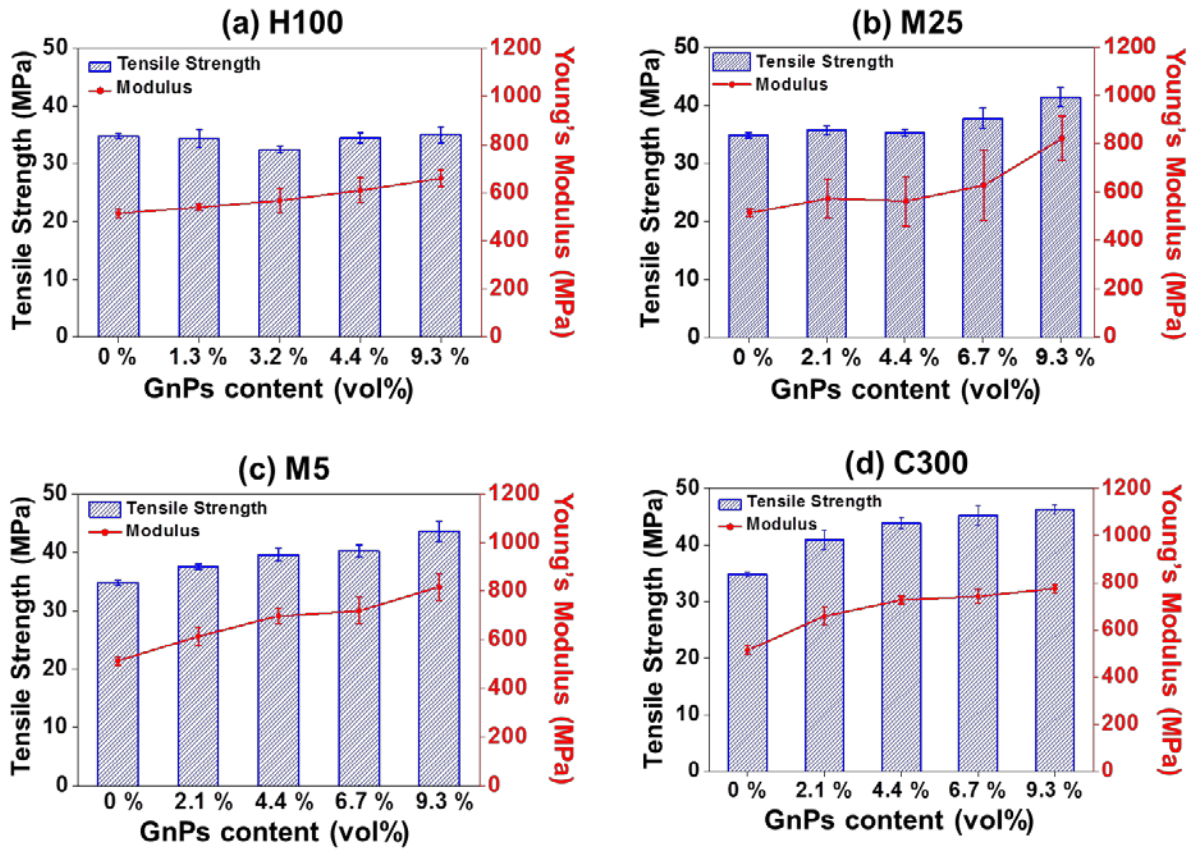
Table A-1. The crystallization parameters extracted from DSC

Vol%	Neat PP	PP_H100				PP_M25				PP_M5				PP_C300			
		1.3	3.2	4.4	9.3	2.1	4.4	6.7	9.3	2.1	4.4	6.7	9.3	2.1	4.4	6.7	9.3
T_{cry}	123.5	127.1	127.9	128.6	129.6	128.2	129.6	131.5	133.1	129.7	131.9	133.6	134.9	132.6	135.6	137.2	137.8
T_m	162.7	163.6	163.2	162.0	163.3	164.0	164.1	164.9	164.8	164.4	164.3	164.7	164.7	165.0	165.2	165.5	165.6
ΔT	39.2	36.5	35.3	33.4	33.7	35.8	34.5	33.4	31.7	34.8	32.4	31.1	29.8	32.4	29.6	28.3	27.8
ΔH_{cry}	171.5	166.6	162.7	150.5	133.5	119.0	115.9	111.1	104.0	124.1	118.9	112.2	105.4	122.9	121.0	109.4	103.6
ΔH_m	124.8	122.5	117.3	113.1	100.6	123.1	116.4	112.3	105.7	122.0	116.2	110.7	105.5	122.4	117.8	108.6	103.5
X_c	60	60	60	60	59	62	62	63	63	62	62	62	62	62	62	61	61

Table A-2. The relative contents of β form of crystals (k_β) in the PP/GnPs_H100 composites were calculated by Turner-Jones method. It should be noted that only α planes of (110), (040), and (130) are taken into account for estimation. The k_β values are further reduced when taking all the peaks for α planes of (041) and (060) into the calculation as shown in the table (this relative content of β crystals is denoted as $k_\beta*$).

Loading of GnPs (vol%)	k_β (%)	$k_\beta*$ (%)
0.0	0	0
1.3	12	11
3.2	13	11
4.4	11	9
9.3	12	11

Table A-3. The XRD peaks of GnPs analyzed by the Scherrer-Debye equation. The calculations show that the number of GnP layers within the composite increases, which indicates that GnPs have aggregated due to the sheer force created during the compounding process. It should be noted, however, that the number of layers calculated by the equation is a preliminary estimation, and it might not be directly indicative of actual numbers of layers in the composites.

	FWHM (rad)	L_c	Number of layers
GnP	0.00654	217.79	64.4
PP/GnP_1.3 vol%	0.00597	239.25	74.3
PP/GnP_3.2 vol%	0.00623	228.91	69.9
PP/GnP_4.4 vol%	0.00619	230.53	71.1
PP/GnP_9.3 vol%	0.00598	238.51	73.4

Table A-4. Percentage improvement (%) of tensile strength and Young's modulus of PP_GnPS composites

GnPs (vol%)	Tensile Strength (% improvement)				Young's Modulus (% improvement)			
	H100	M25	M5	C300	H100	M25	M5	C300
0.0	0.0	0.0	0.0	0.0	0.0	0.0	0.0	0.0
1.3	-1.1	-	-	-	5.1	-	-	-
2.1	-	2.6	7.8	17.5	-	11.7	19.6	28.3
3.2	-6.6	-	-	-	10.4	-	-	-
4.4	-0.9	1.4	13.8	25.9	18.7	9.5	35.9	41.5
6.7	-	8.3	15.5	29.9	-	22.2	40.0	44.4
9.3	-1.4	19.5	25.3	33.0	28.4	52.9	59.1	50.9

Appendix B

The calculation of degree of crystallinity

The degree of crystallinity (X_c) of the composites was calculated by the following equation[1]:

$$X_c = \left(\frac{1}{1 - wt\%(GnP)}\right) \times \frac{\Delta H_m}{\Delta H_m^o} \tag{B-1}$$

where ΔH_m is the heat of fusion estimated from DSC curves, ΔH_m^o is the heat of fusion of 100% crystalline PP[2] which is taken as 209 J·g^{-1}, and the weight percent of GnPs was taken from TGA curves

Conversion of weight fraction to volume fraction

The volumetric fraction of GnPs (φ_{vt}) in the composites and can be converted from weight fraction by the following equation[1],

$$\varphi_{vt} = \frac{1}{1 + \dfrac{\rho_{GnP}}{\rho_{PP}}\left(\dfrac{1}{\varphi_{wt}} - 1\right)} \tag{B-2}$$

where ρ_{GnP} and ρ_{PP} represent the density of GnPs and PP, respectively. φ_{wt} is the weight fraction of GnPs. The density of GnPs and PP are 2.2 g·cm^{-3} and 0.9 g·cm^{-3}, respectively.

---

[1]Logakis E, Pollatos E, Pandis C, Peoglos V, Zuburtikudis I, Delides CG, et al. Structure-property relationships in isotactic polypropylene/multi-walled carbon nanotubes nanocomposites. Composite Science and Technolgy. 2010;70:328–35.

[2]Hoffman D Wartig KA, Thomann R, Dittrich B, Schartel B, Mülhaupt R. Functionalized graphene and carbon materials as additives for melt-extruded flame retardant polypropylene. Macromolecular Materials and Engineering. 2013;298:1322–34.

The calculation of relative contents of *β* form of crystals

The relative contents of *β* form of crystals, so-called *k* value proposed by Turner-Jones and co-workers, were calculated by the following equation:

$$k_\beta = \frac{I_{\beta 1}}{I_{\alpha 1} + I_{\alpha 2} + I_{\alpha 3} + I_{\beta 1}} \times 100\% \qquad \text{(B-3)}$$

where $I_{\beta 1}$ is the intensity of the diffraction peaks responsible for *β*(300) plane, and $I_{\alpha 1}, I_{\alpha 2}, I_{\alpha 3}$ is the intensity of the diffraction peaks responsible for α(110), α(040), and α(130) planes, respectively.